Quantification of Pore Pressure in Subduction Zones and its Implication for the Slip Behavior of the Plate Interface

Dissertation for the Doctoral Degree in Natural Sciences
in the Faculty of Geosciences
University of Bremen

Submitted by

Junli Zhang

Bremen, April 2021

REVIEWERS / GUTACHTER

Prof. Dr. Achim J. Kopf

University of Bremen

MARUM - Centre for Marine Environmental Sciences

Leobener Str. 8

28359 Bremen, Germany

Prof. Dr. Jan Behrmann

GEOMAR | Helmholtz Center for Ocean Research Kiel

Wischhofstrasse 1-3

24148 Kiel, Germany

Date of the doctoral colloquium / Datum des Prüfungskolloquiums

24 June / Juni 2021

Versicherung an Eides Statt / *Affirmation in lieu of an oath**

gem. § 5 Abs. 5 der Promotionsordnung vom 18.06.2018 /
according to § 5 (5) of the Doctoral Degree Rules and Regulations of 18 June, 2018

Ich / I, _____
(Vorname / First *Name*, Name / *Name*, Anschrift / *Address*, ggf. Matr.-Nr. / *student ID no., if applicable)*

versichere an Eides Statt durch meine Unterschrift, dass ich die vorliegende Dissertation selbständig und ohne fremde Hilfe angefertigt und alle Stellen, die ich wörtlich dem Sinne nach aus Veröffentlichungen entnommen habe, als solche kenntlich gemacht habe, mich auch keiner anderen als der angegebenen Literatur oder sonstiger Hilfsmittel bedient habe und die zu Prüfungszwecken beigelegte elektronische Version (PDF) der Dissertation mit der abgegebenen gedruckten Version identisch ist. / *With my signature I affirm in lieu of an oath that I prepared the submitted dissertation independently and without illicit assistance from third parties, that I appropriately referenced any text or content from other sources, that I used only literature and resources listed in the dissertation, and that the electronic (PDF) and printed versions of the dissertation are identical.*

Ich versichere an Eides Statt, dass ich die vorgenannten Angaben nach bestem Wissen und Gewissen gemacht habe und dass die Angaben der Wahrheit entsprechen und ich nichts verschwiegen habe*. / I affirm in lieu of an oath that the information provided herein to the best of my knowledge is true and complete.*

Die Strafbarkeit einer falschen eidesstattlichen Versicherung ist mir bekannt, namentlich die Strafandrohung gemäß § 156 StGB bis zu drei Jahren Freiheitsstrafe oder Geldstrafe bei vorsätzlicher Begehung der Tat bzw. gemäß § 161 Abs. 1 StGB bis zu einem Jahr Freiheitsstrafe oder Geldstrafe bei fahrlässiger Begehung. / *I am aware that a false affidavit is a criminal offence which is punishable by law in accordance with § 156 of the German Criminal Code (StGB) with up to three years imprisonment or a fine in case of intention, or in accordance with § 161 (1) of the German Criminal Code with up to one year imprisonment or a fine in case of negligence.*

_____ _____
Ort / *Place*, Datum / *Date* Unterschrift / *Signature*

*The affirmation was signed in the submitted printed version.

ABSTRACT

Subduction zones host the largest earthquakes and ~90% of the global seismic energy is released there. It has been recognized that large tectonic earthquakes occur by sudden slip along the pre-existing plate interface (décollement) and thus are a frictional phenomenon. Pore fluid pressure plays a crucial role in the earthquake generation and propagation of seismic slip, because it not only governs the frictional strength of faults but also exerts an important control on the mode of slip. Therefore, predicting pore pressure is critical to understand the fault slip behavior in subduction zones and provides key information for the assessment of geological hazard potential. In this Ph.D. dissertation, pore pressure in the Nankai Trough, North Sumatra and Northern Hikurangi subduction zones is investigated and linked to the occurrence of tsunamigenic earthquakes and slow slip events.

In the Nankai Trough subduction zone, robust pore pressure estimates are provided for both the accreting and subducting sediments based on consolidation experiments and numerical models. Continuous excess pore pressure with nearly constant ratios of pore pressure to lithostatic stress is revealed in the accreted and underthrust sediments, implying the Nankai décollement is not a fluid barrier as previously suggested. Pore pressures 84%-93% of the lithostatic stress along the décollement are inferred by experimental data, which might originate from repeated lithostatic pore pressure transients in the last 3 kyrs. The high excess pore pressure leads to the shear strength of Nankai subduction thrust at the toe of accretionary prism as low as 0.4-0.8 MPa, which may facilitate the likelihood of seismic slip propagation to the trench and thus a catastrophic tsunami offshore SW Japan, when a large earthquake happens.

In addition, the robust pore pressure estimates in the Nankai Trough are employed to evaluate a porosity-based pore pressure prediction approach. The approach advances a recently proposed critical state soil mechanics method by taking the consolidation state of sediments into account. Compared with the normally consolidated sediment, the overconsolidated sediment in the Nankai Trough generates 40%~50% less excess pore pressure, suggesting that overconsolidation inhibits the development of excess pore pressure. Using the pore pressure prediction approach for overconsolidated sediments, the mechanical properties of the Nankai décollement are quantified. The shear strength along the décollement is below 2.2 MPa, obviously larger than the shear stress (<0.4 MPa). This implies that the accretionary prism is not at Coulomb failure, which is in good agreement with the dynamic Coulomb wedge theory.

In the North Sumatra subduction zone, estimates of pore pressure are provided for IODP Sites U1480 and U1481, ~225 km seaward of the trench. Experimental results reveal moderate excess pore pressure in a horizon which is considered as a proto-décollement. The pore pressure evolution is simulated through a one-dimensional sedimentation-flow model which accounts for the

sedimentation rate and silicate dehydration. The modeling results show that the excess pore pressure increases continuously and reaches a high level corresponding to a pore pressure up to 96% of lithostatic stress, as the sediment approaches the trench. Therefore, high excess pore pressure is inferred along the plate interface and is invoked to explain the landward-vergent frontal thrusts. The high excess pore pressure in the near-trench faults may facilitate the propagation of coseismic slip all the way to the trench and, thus, potentially increases the tsunami size in the 2004 great Sumatra-Andaman earthquake.

In the Northern Hikurangi subduction zone, consolidation experiments on samples from IODP Site U1520 show that the sediment in trench-wedge facies is underconsolidated whereas that in pelagic and volcaniclastic facies is overconsolidated. Lithology, biostratigraphy and seismic reflection data suggest that the trench-wedge facies are stratigraphically equivalent to the horizon where the active Pāpaku splay fault occurs at IODP Site U1518. Based on the consolidation data on trench-wedge facies, a pore pressure prediction equation for Site U1518 is derived using critical state soil mechanics. Pore pressure 77% of lithostatic stress is revealed at the top of the Pāpaku fault, whereas the pore pressure at the bottom increases to 93% of lithostatic stress. Previous studies have shown that slow slip events (SSEs) in the North Hikurangi subduction zone may propagate to a depth of < 2 km below seafloor (kmbsf). Therefore, SSEs at 2 kmbsf are simulated under above pore pressure conditions according to the rate-and-state friction theory. The modeling results are comparable to the natural SSEs and indicate that high pore pressure decreases the reoccurrence interval of SSEs.

ZUSAMMENFASSUNG

In Subduktionszonen entstehen die größten Erdbeben und ~90 % der globalen seismischen Energie wird dort freigesetzt. Die Erdbeben finden entlang bereits der bestehenden Verwerfung der Plattengrenze (Décollement) statt und stellen somit ein Reibungsphänomen dar. Der Porendruck spielt eine entscheidende Rolle bei der Erdbebenentstehung und der Ausbreitung des seismischen Versatzes, da er das Versagen von Verwerfungen bestimmt und die Art des Reibungsgleitens kontrolliert. Daher ist die Vorhersage des Porendrucks von entscheidender Bedeutung, um das Reibungsverhalten von Verwerfungen in Subduktionszonen zu verstehen und das geologische Gefährdungspotential abzuschätzen. In der vorliegenden Dissertation wird der Porendruck in den Subduktionszonen Nankai-Trog, Nord-Sumatra und Nord-Hikurangi quantifiziert und mit dem Auftreten von Tsunami-Erdbeben und langsamen Erdbeben, sogenannten „slow slip“ Ereignissen, untersucht.

Für den Nankai-Trog werden robuste Porendruckabschätzungen durch einen multimethodischen Ansatz aus Konsolidierungsexperimenten und numerischen Modellen, sowohl für die akkretierenden als auch für die subduzierenden Sedimente, vorgenommen. Die Ergebnisse zeigen einen kontinuierlich ansteigenden Porenüberdruck mit nahezu konstantem Verhältnis von Porendruck zu lithostatischer Spannung in den akkretierten und subduzierten Sedimenten. Dies deutet darauf hindeutet, dass die Plattengrenze im Nankai-Trog kein Wasserstauer ist, wie zuvor angenommen. Aus den experimentellen Daten abgeleitete Porendrücke von 84%-93% der lithostatischen Spannung entlang des Décollements werden dabei auf wiederholte lithostatische Porendruckpulse in den letzten 3 kyrs zurückgeführt. Der hohe Porenüberdruck führt dazu, dass die Scherfestigkeit des Décollements am Fuß des Akkretionskeils nur 0,4-0,8 MPa beträgt, was die Wahrscheinlichkeit einer seismischen Ausbreitung bis zum Tiefseegraben und damit die Entstehung eines verheerenden Tsunamis vor der Küste SW-Japans bei einem großen Erdbeben begünstigen könnte.

Darüber hinaus werden die Porendruckschätzungen im Nankai-Trog für die Bewertung eines neuen porositätsbasierten Modells zur Porendruckvorhersage verwendet, dass den Konsolidierungszustand der Sedimente berücksichtigt. Der Ansatz stellt eine Weiterentwicklung eines kürzlich vorgestellten Modells dar, das auf dem bodenmechanischen Konzept des kritischen Zustands aufbaut. Verglichen mit dem normal konsolidierten Sediment wird in dem überkonsolidierten Sediment des Nankai-Trogs 40-50% weniger Porenüberdruck aufgebaut. Eine Überkonsolidierung mindert daher die Porenüberdruckentstehung. Unter Berücksichtigung der Überkonsolidierung der Sedimente im Nankai-Trog werden mit Hilfe des neu entwickelten Ansatzes zudem die mechanischen Eigenschaften der Plattengrenze in der Subduktonszone quantifiziert. Die Scherfestigkeit entlang der Überschiebung liegt unter 2,2 MPa und ist damit größer als die Scherspannung (<0,4 MPa). Dies impliziert, dass der äußere Akkretionskeil nicht

im Zustand des mechanischen Versagens ist und in Übereinstimmung mit der „dynamic Coulomb wedge"-Theorie steht.

In der Nord-Sumatra Subduktionszone wurde der Porendruck für die IODP-Lokationen U1480 und U1481 quantifiziert, die sich ~225 km seewärts des Tiefseegrabens befinden. Ergebnisse aus den experimentellen Konsolidierungsversuchen belegen einen moderaten Porenüberdruck in einem Horizont, der als Proto-Décollement betrachtet wird. Die Porendruckentwicklung in Richtung Subduktionszone wird durch ein eindimensionales Konsolidierungsmodell simuliert, das die Sedimentationsrate und die Dehydrierung von Silikaten berücksichtigt. Die Modellierungsergebnisse zeigen, dass der Porenüberdruck kontinuierlich ansteigt und einen Höchstwert von 96% der lithostatischen Spannung erreicht, wenn sich das Sediment dem Tiefseegraben nähert. Daraus wird ein hoher Porenüberdruck entlang der Plattengrenze abgeleitet und zur Erklärung des Versatzes im großen Sumatra-Andaman-Erdbeben 2004 herangezogen indem der hohe Porenüberdruck die Ausbreitung des koseismischen Versatzes bis in den Tiefseegraben erleichtert und damit möglicherweise die Größe des Tsunamis erhöht hat.

In der nördlichen Hikurangi-Subduktionszone zeigen Konsolidierungsexperimente an Proben der IODP Lokation U1520, dass das Sediment der Tiefseegrabenfazies unterkonsolidiert ist, während das tiefer liegende Sediment der pelagischen und vulkaniklastischen Fazies überkonsolidiert ist. Lithologie, Biostratigraphie und seismische Reflektionsdaten deuten darauf hin, dass die Tiefseegrabenfazies stratigraphisch äquivalent zu dem Horizont ist, in dem die aktive Pāpaku-Spreizungsstörung an der IODP Site U1518 auftritt. Basierend auf den Konsolidierungsdaten der Tiefseegrabenfazies wird der Porendruck für die Lokation U1518 unter Verwendung des in dieser Arbeit entwickelten bodenmechanischen Models abgeleitet. Der Porendruck beträgt 77% der lithostatischen Spannung am oberen Ende der Pāpaku-Verwerfung und steigt bis zum unteren Ende auf 93% der lithostatischen Spannung an. Frühere Studien haben gezeigt, dass sich SSEs („slow slip" Ereignisse) in der nördlichen Hikurangi Subduktionszone bis zu einer Tiefe von < 2 km unter dem Meeresboden (kmbsf) ausbreiten können. Daher werden SSEs in 2 kmbsf unter den oben genannten Porendruckbedingungen gemäß der „Rate-and-State-Friction" - Theorie simuliert. Die Modellierungsergebnisse sind vergleichbar mit den natürlichen SSEs und zeigen, dass hoher Porendruck das Wiederholungsintervall von SSEs verringert.

CONTENTS

Chapter 1: Introduction

1.1 Earthquakes in Subduction Zone

Subduction zone is a region where a denser oceanic plate is subducting beneath a more buoyant continental or another oceanic plate (Stern, 2002). As an active convergent plate margin, subduction zones accommodate the plate motions and host the largest earthquakes (e.g., Kanamori, 1986). Statistics of global large earthquakes between 1900 and 1989 have shown that 90% of the seismic energy is released in subduction zones (Pacheco & Sykes, 1992). It has been recognized that large tectonic earthquakes occur by sudden slip along the pre-existing plate interface and thus are a frictional phenomenon (Scholz, 1998). Therefore, understanding the slip behavior of the plate interface in subduction zones has been a subject of ongoing concern (e.g., Hirose & Hirahara, 2002; Schwartz & Rokosky, 2007; Saffer & Wallace, 2015; Saffer, 2017; Wallace, 2020).

Subduction zones can be divided into accretionary and nonaccretionary types (von Huene & Scholl, 1991). The accretionary subduction zones are characterized by a portion of sediment on the incoming plate accreted onto the frontal tip of the overriding plate where an accretionary prism is formed (Saffer & Tobin, 2011). The rest sediment on the incoming plate normally underthrusts beneath the overriding plate, enters the subduction factory and reequilibrates with the mantle of Earth (Stern, 2002). In contrast, for nonaccretionary subduction zones, the sediment completely subducts beneath the overriding plate and no sediment on the incoming plate is accreted (Saffer & Tobin, 2011). The plate boundary interface which separates the overriding plate from the underthrusting section is a megathrust and is also termed décollement (Figure 1-1).

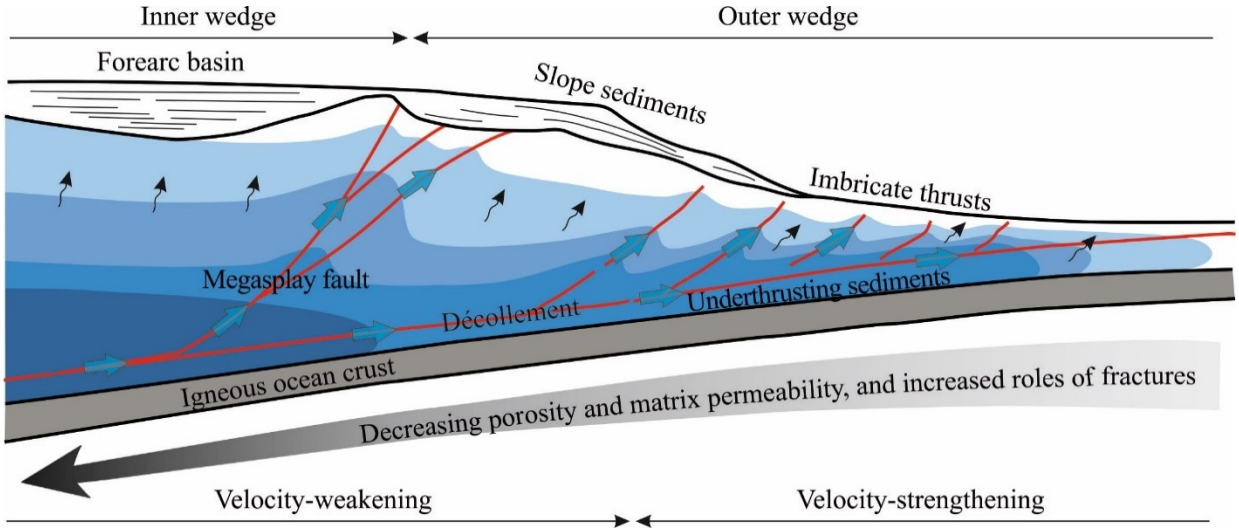

Figure 1-1. Schematic cross section of subduction zone forearc showing geologic elements and hydrologic processes of accretionary wedge after Saffer and Tobin (2011) and Moore et al. (2007). Blue shading denotes excess pore pressure and deeper blue represents higher excess pore pressure.

Arrows show fluid flow and are scaled qualitatively to illustrate flow rates. Red lines illustrate the distribution of faults.

Large subduction earthquakes nucleate on the plate boundary megathrust and occur at a specific depth range which is called seismogenic zone (e.g., Scholz, 2019). The updip and downdip limits approximately locate at depths of 5-10 and 25-55 km below seafloor, respectively (Ruff & Tichelaar, 1996; Deshon et al., 2003). Further investigations suggest that the updip limit might be associated with a suite of diagenetic to low-grade metamorphic processes corresponding to a temperature range of 100-150 °C (Moore & Saffer, 2001), whereas the lower limit seems to be attributable to rock behavior transition from brittle to ductile (Oleskevich et al., 1999) when the temperature reaches 350-450°C (Hyndman et al., 1995). Friction experiments provide direct evidence for the former. For examples, with the increasing lithification, the frictional behavior of the sediment changes from velocity-strengthening to velocity-weakening (e.g., Trütner et al., 2015; Ikari & Hüpers, 2021). The transformation of smectite to illite promotes the lithification and slip-weakening behavior (e.g., Lauer et al., 2017). Therefore, a classical subduction earthquake model (e.g., Moore & Saffer, 2001) is established that earthquakes nucleate and rupture in the inner subduction thrust system whereas the material in the outer system is aseismic and any seaward rupture propagation should cease in velocity-strengthening unconsolidated sediments (Figure 1-1).

However, coseismic slip nearly extending to the trench was inferred in the 2004 Sumatra-Andaman and 2011 Tohoku earthquakes (e.g., Bletery et al., 2016; Fujiwara et al., 2011), which triggered devastating tsunamis through large seafloor displacement and challenged the prevailing model (Hüpers et al., 2017). Therefore, the origin of seismogenic behavior is more sophisticated and requires accounting for conditions that include, but might not be limited to, clay dehydration (e.g., Lauer et al., 2017), precipitation of calcite and quartz (e.g., Peltonen et al., 2009; Saffer et al., 2012), water content (e.g., Ikari et al., 2007), sliding velocity (e.g., Ikari & Kopf, 2017), and stress state (e.g., Saffer & Marone, 2003; Faulkner et al., 2011). A recent explanation for the occurrence of coseismic slip in shallow subduction zones was proposed that the weak sediment in the outer subduction system is energetically favorable for the propagation of earthquakes and permits earthquake slip to the trench (Faulkner et al., 2011). Another important finding in shallow subduction in the last two decades was the recognition of a spectrum of slow earthquake phenomena (Saffer & Wallace, 2015). Within this spectrum, slow slip events (SSEs) or silent slip/earthquakes which are characterized by too low sliding velocity to produce earthquakes (Schwartz & Rokosky, 2007), attracted great attention, due to its close relationship with ordinary earthquakes and tsunamigenic earthquakes (Koulali et al., 2017). It has been proposed that pore fluid pressure plays a fundamental role in the generation of this fault slip behavior (Kodaira et al., 2004; Arnulf et al., 2021).

In fact, pore fluid pressure has been thought to has profound influence on the mechanics of earthquakes and faulting (Saffer & Tobin, 2011). Previous study has shown that fault-valve behavior is governed by pore pressure (Sibson et al., 1988; Sibson, 1990): under a given deviatoric

stress state (σ_1'-σ_3'), faulting of intact formation or reactivation of existing faults can be triggered by elevated pore pressure. Pore pressure not only determines the absolute strength of faults (e.g., Townend & Zoback 2001), but also plays a critical role in the hydro-mechanical processes at subduction zones (Saffer & Tobin, 2011). There is common agreement that the overall geometry of the subduction complex is closely related to pore pressure (e.g., Davis et al. 1983; Wang & Hu, 2006). Based on the mechanics of earthquakes and faulting (Scholz, 1998), pore pressure governs the frictional stability of the fault which can be described by the friction stability parameter ζ:

$$\zeta = (a\text{-}b) \cdot \sigma_e \tag{1-1}$$

where a an b are velocity-dependent frictional properties of material, and σ_e is the effective normal stress on the fault plane. Positive (a-b) value represents velocity-strengthening material, corresponding to a positive ζ which predicts intrinsically stable behavior. In contrast, the material with negative (a-b) and ζ values exhibits velocity-weakening behavior and is either unstable (large negative values of ζ) or conditionally stable (small negative values of ζ). According to the Terzaghi's effective stress theory, the normal stress σ is borne by the effective normal stress σ_e and pore pressure P:

$$\sigma = \sigma_e + P \tag{1-2}$$

Hence the material with low pore pressure is unstable while that with high pore pressure is conditional stable (Scholz, 1998). Normally earthquakes cannot nucleate on conditional stable fault patches, but the fault patches can be destabilized when a nearby earthquake initiates (Park et al., 2014). Therefore, pore pressure decides the distribution of seismogenic zones (e.g., Moore & Saffer, 2001) and rupture propagation zones (e.g., Seno, 2002). Furthermore, it has been accepted that pore pressure also has profound effects on the mode of fault slip behavior (e.g., Kitajima & Saffer, 2012; Liu & Rice, 2007). Therefore, pore pressure is a key parameter to understand the dynamics and evolution of subduction zones (Saffer & Tobin, 2011). To date, excess pore pressure has been widely invoked to explain the small critical taper of accretionary wedge (e.g., Dahlen, 1990), the occurrence of tsunamigenic slip near the trench (e.g., Seno, 2002), the wide seismogenic zone (e.g., Fagereng & Ellis, 2009), as well as a series of new modes of slip behavior including slow slip events (e.g., Song et al., 2009), low frequency earthquakes and very low-frequency earthquakes (e.g., Ito & Obara, 2006).

1.2 Pore Pressure in Subduction Zones

In subduction zones, pore pressure is tightly interconnected with the fluid flow processes, and widely distributed excess pore pressure has been revealed (Figure 1-1). According to the Darcy law (1856), permeability exerts a first order control on pore pressure. Therefore, the excess pore pressure is attributable to the relatively low permeability which cannot drain the pore fluid in time when the sediment is rapidly loaded due to high sedimentation rate and lateral tectonic compaction (e.g., Skarbek & Saffer, 2009; Flemings & Saffer, 2018). The release of bound water driven by diagenetic processes is another important origin of excess pore pressure (e.g., Lauer et al., 2017).

Besides, the up-dip migrated deep fluids along faults may also contribute to the generation of excess pore pressure (Zhang et al., 2021). Geochemical anomaly such as elevated B, Li or CH_4 concentrations which are typical signatures for deep-rooted pore fluids provide solid evidence (e.g., Kastner et al., 1991; You et al., 1996). Following Gordon and Flemings (1998), the pore pressure evolution accounting for these effects is described by:

$$\frac{\partial P}{\partial t} = \frac{1}{S_t} \cdot \frac{\partial}{\partial z}\left[\frac{k}{\mu} \cdot \left(\frac{\partial P}{\partial z} - \rho g\right)\right] + \gamma \cdot \frac{\partial \sigma}{\partial t} + \frac{1}{S_t} \cdot \frac{\partial V}{\partial t} \tag{1-3}$$

where P is the pore pressure, t is the time, S_t is the storage coefficient, z is the burial depth, k is the permeability, μ is the viscosity of pore water, ρ is the water density, g is the gravity acceleration, $\frac{\partial \sigma}{\partial t}$ is the loading rate, γ is the loading efficiency, $\frac{\partial V}{\partial t}$ is the fluid production rate during diagenetic processes. The term on the left side represents the final variation of pore pressure with time. The first term on the right side represents the component caused by Darcy flow. The second term on the right side represents the component attributed to the rapid loading by high sedimentation rate and lateral tectonic compaction. The third term on the right side represents the component derived from the pore water volume variation such as opal-A to opal-CT to quartz, clay dehydration and fluid influx along faults.

Numerous studies have investigated the pore pressure in subduction zones (e.g., Screaton et al., 2002; Tsuji et al., 2008, 2014; Flemings & Saffer, 2018). Qualitatively, a series of indicators for excess pore pressure have been proposed. For example, relatively high porosity has been regarded as inhibited pore fluid drainage which cannot equilibrate with the rapid increase of loading, and is viewed as a manifestation of excess pore pressure (e.g., Screaton et al., 2002). Seismic velocity decreases with increase of pore pressure, reversal of acoustic impedance (impedance = velocity × density) thus has been seen as evidence of excess pore pressure (e.g., Tobin et al., 1994; Moore et al., 1995). Also, classical Coulomb wedge theory links the morphology of accretionary wedge to pore pressure and considers the low taper angle as indicative of excess pore pressure (e.g., Davis et al., 1983; Wang & Hu, 2006). On the other hand, many quantitative approaches have been developed to estimate the magnitude of pore pressure. The approaches for pore pressure estimation include, but are not limited to, using tapered probes (e.g., Flemings et al., 2008) or Long Term Borehole Monitoring System (e.g., Kopf et al., 2011; Kopf et al., 2017), leak-off or hydraulic fracturing tests (e.g., Couzens-Schultz & Chan, 2010), inference from wellbore breakouts (e.g., Huffman & Saffer, 2016), laboratory consolidation experiments (e.g., Saffer et al., 2000), hydrogeological modeling (e.g., Dugan et al., 2003), prediction from porosity (e.g., Screaton et al., 2002) and conversion of seismic interval velocities (e.g., Tobin & Saffer, 2009; Tsuji et al., 2008, 2014). Among them, direct pore pressure measurements through such as borehole observatories or pore pressure probes are rare due to the high costs. Laboratory experimental data provide robust but limited pore pressure estimates. Numerical modeling can constrain pore pressure evolution, but requires input of many accurate parameters. In comparison, porosity, seismic velocity, or other

analogous data not only provides reliable pore pressure estimates, but also can be applied to a large area.

Consolidation experiment is an important experimental approach to calculate the pore pressure in subduction zones. In uniaxial consolidation experiments, a load is applied on the samples. With the increase of applied load, the specimen deforms and the resulting deformation is recorded by a linear variable displacement transducer (LVDT). By plotting the deformation against the applied stress, a yield point can be identified. This yield point is commonly regarded as the maximum vertical effective stress that the sediment has sustained and is termed preconsolidation stress (e.g., Casagrande, 1936). The experimental procedure has been established by American Society for Testing and Materials (ASTM) Committee and detailed description can be found in ASTM D2435/D2435M-11 (ASTM International, 2011). Assuming the preconsolidation stress represents the in situ vertical effective stress, the pore pressure can be calculated (e.g., Saffer, 2003). This method is normally limited to underthrust sediment, because the preconsolidation stress in accretionary prism is highly affected by tectonic stress (e.g., Moore et al., 1998). Despite this, Moore and Tobin (1997) investigated the pore pressure in accreted sediments by interpreting the preconsolidation stress as the in situ horizontal effective stress.

Porosity-based pore pressure prediction approach is another widely used method to investigate the pore pressure in subduction zones, because porosity can be easily obtained from moisture and density (MAD) measurements (e.g., Screaton et al., 2002), logging while drilling (LWD) data (e.g., Hoffman & Tobin, 2004), or pre-drilling seismic velocity (e.g., Tobin & Saffer, 2009). Due to the great challenge in submarine deep-drilling, the current deepest borehole in the ocean is 3262.5 meters below seafloor (Tobin et al., 2020). Therefore, pore pressure prediction for great depth mainly relies on seismic data. For porosity-based pore pressure prediction approach, a key step is to establish a relationship between porosity and effective stress (e.g., Tobin & Saffer, 2009). The empirical relationship represents a normal consolidation curve (e.g., Swarbrick, 2001) and is usually obtained from a reference site prior to subduction (e.g., Screaton et al., 2002). Although many studies have established solid porosity-effective stress relationships and have generated robust pore pressure estimates, they mainly focused on the underthrust sediment (e.g., Saffer, 2003; Skarbek & Saffer, 2009). The underlying reason is that the underthrusting sediment is subjected to uniaxial consolidation, whereas the stress path of accretionary prism is more complex (e.g., Kitajima & Saffer, 2014). Both the underthrust section in subduction zones and the reference sites where the empirical relationship is established are thought to deform in uniaxial compression and their consolidation is mainly governed by vertical effective stress (e.g., Moore & Tobin, 1997; Tsuji et al., 2008). Therefore, the empirical relationship acquired from reference sites is applicable to the underthrust section. In comparison, the accretionary prism is highly affected by the lateral tectonic stress and thus the consolidation of sediments is controlled by both mean effective stress and shear stress (e.g., Kitajima et al., 2017), such that the empirical relationship is not applicable to the accreting sediments.

The key for the pore pressure prediction in accretionary prism is to establish an applicable empirical relationship between porosity (or analogous parameter) and effective stress. The critical state soil mechanic provides the foundation to derive the empirical relationship in accretionary prism from that acquired at reference sites (e.g., Kitajima & Saffer, 2012; Flemings & Saffer, 2018). Karig (1986) made the first effort to estimate the prism pore pressure with this method (Flemings & Saffer, 2018). For the accretionary prism, the sediment initially experiences uniaxial compression before passing into the wedge (e.g., Yamamoto et al., 2013). When the sediment is accreted on the overriding wedge, the horizontal stress increases and may reach Coulomb failure (e.g., Kitajima & Saffer, 2014). Assuming the accretionary prism is in a state of Coulomb failure, Flemings and Saffer (2018) proposed a generalized method to predict pore pressure in subduction zones based on the Modified Cam Clay (MCC) model (Roscoe & Burland, 1968). This method is applicable to both underthrust and accreted sediments and brings new insights into the stress state in accretionary prism (Flemings & Saffer, 2018). In addition to this method, triaxial experiments provide another approach to establish the empirical relationship between porosity (or analogous parameter) and effective stress in the accretionary prism. For example, Kitajima and Saffer (2012) conducted triaxial deformation experiments and determined the critical state line which represents the empirical relationship between mean effective stress and void ratio for the accreted sediment.

1.3 Motivation and Research Design

As discussed above, previous studies have led to greatly improved understanding of the hydro-mechanical processes in subduction zones and their relations with subduction earthquakes. However, there is still much to be learned and improved, including but not limited to the following aspects (Figure 1-2):

(1) Pore pressure prediction in the accretionary prism and fault zone

The pore pressure prediction in subduction zones mainly focuses on the underthrust sediments (e.g., Screaton et al., 2002; Skarbek & Saffer, 2009), while pore pressure estimates in the accretionary prism are scarce due to its complex stress environment (e.g., Yamamoto et al., 2013). Flemings and Saffer (2018) recently proposed a method to estimate the stress state in the Nankai accretionary prism and revealed greater excess pore pressure than that in underthrust sediments. However, this result seems to contradict with the drainage of pore fluids from buried sediments to seafloor, because higher excess pore pressure in the accretionary prism will act as a pore pressure seal. Therefore, more studies are needed to verify the pore pressure state in the accretionary prism. For the pore pressure in subduction zone faults, it has been widely accepted that high excess pore pressure exists along the décollement (e.g., Tobin et al., 1994; Bekins & Screaton, 2007; Saffer & Tobin, 2011). However, previous quantitative studies were mainly based on geophysical data (e.g., Tobin & Saffer, 2009; Tsuji et al., 2014) and experimental pore pressure estimates for the décollement zone are sparse. There is a need to provide experimental estimates to verify the high pore pressure along the décollement.

(2) The effect of consolidation state on pore pressure prediction

Consolidation experiments have been successfully used to estimate the pore pressure in subduction zones (e.g., Saffer, 2003), but it relies on a fundamental assumption that the preconsolidation stress acquired from consolidation tests represents the in situ vertical effective stress (e.g., Dugan & Germaine, 2008). Previous studies have shown that many phenomena such as secondary consolidation and diagenesis could shift the preconsolidation stress to higher values (e.g., Bjerrum, 1973; Morgan & Ask, 2004). Therefore, the consolidation state of sediments has to be taken into consideration when using preconsolidation stress to calculate pore pressure, which is lacking in previous studies (e.g., Saffer, 2003; Dugan & Germaine, 2008). Similarly, for non-experimental methods, the consolidation state of sediments also has important impact on the pore pressure results (Swarbrick, 2001). Among them, one important method is a porosity-based approach proposed by Flemings and Saffer (2018). Different from many empirical methods, this approach is rooted in critical state soil mechanics and provides a complete pathway to predict the pore pressure in a variety of environments (Flemings & Saffer, 2018). However, the consolidation state of sediments is not considered in this model and it is critical to investigate the effects of consolidation state on the model performance.

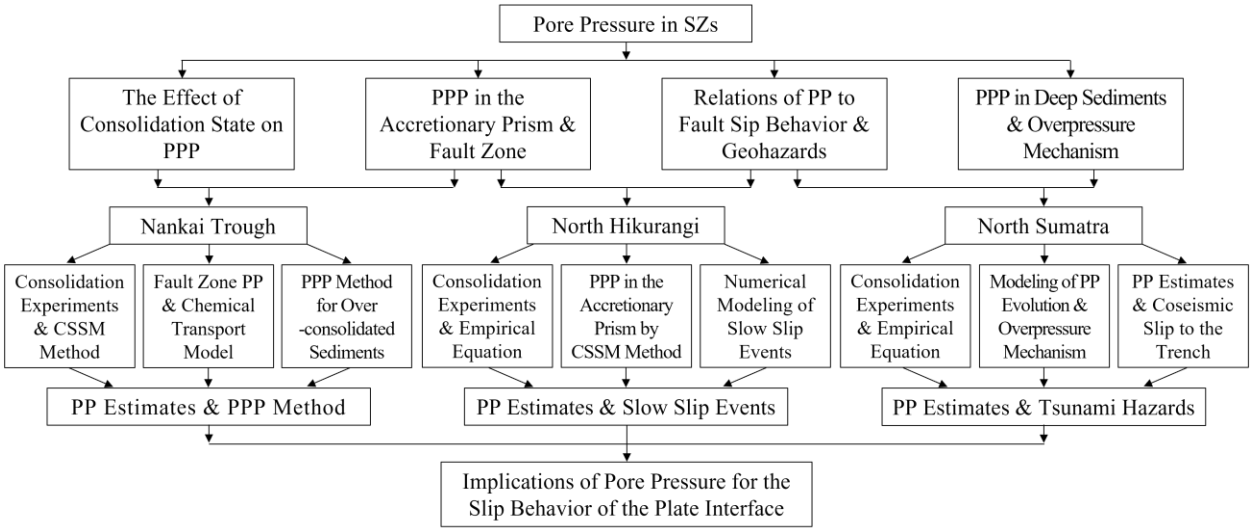

Figure 1-2. Schematic workflow of this Ph.D. study. PP = Pore Pressure, PPP = Pore Pressure Prediction, CSSM = Critical State Soil Mechanics.

(3) Pore pressure prediction in deep sediments and mechanism of excess pore pressure generation

Because current deep-drilling only reaches a depth of 3262.5 meters below seafloor (Tobin et al., 2020), pore pressure prediction in deep sediments is mainly based on seismic data (e.g., Kitajima & Saffer, 2012). It is important to develop other methods to verify the pore pressure estimates in deep sediments due to the multiple solutions of seismic data. On the other hand, to better predict and understand the distribution of excess pore pressure, clarifying the mechanism of excess pore pressure generation is crucial. To date, many mechanisms have been proposed to explain excess

pore pressure in subduction zones. Chief among of them are clay mineral dehydration (e.g., Ko et al., 1997; Lauer & Saffer, 2015), rapid sedimentation rate (e.g., Meridth et al., 2017) and influx of deep fluids (e.g., Saffer & Bekins, 1998; Saffer & Kopf, 2016). However, the relative contribution of different mechanisms to excess pore pressure generation is not well evaluated and quantitative research is especially limited. Quantification of the contribution of different mechanisms to excess pore pressure generation is of interest for the study of pore pressure prediction, and is expected to generate improved understanding of excess pore pressure distribution.

(4) Relations of pore pressure to fault slip behavior and geohazards

It has been recognized that pore pressure has a fundamental effect on the fault slip behavior and SSEs are thought to be closely related to excess pore pressure (e.g., Kodaira et al., 2004), because the region hosting SSEs is commonly characterized by excess pore pressure (Arnulf et al., 2021). However, how pore pressure affects SSEs remains incompletely understood and there is a need to investigate the relationship between pore pressure and SSEs. In addition, pore pressure provides critical information for understanding the frictional stability and earthquake generation in subduction zones, and thus is a key parameter for assessing the geohazard potential (e.g., Seno, 2002). From perspective of energy, the shallow slip near the trench causing tsunamis can be explained by the low fracture energy of weak sediments (Faulkner et al., 2011). Based on the mechanism of frictional strength (Persson, 2000), weak sediments can be attributed to either intrinsic low friction coefficient or high pore pressure. It has been validated that the unexpected large shallow slip in 2011 Tohoku earthquake is owing to the presence of abundant weak smectite (Ujiie et al., 2013). In comparison, the causal relationship between high pore pressure and exceptionally large slip has not been well assessed.

In order to improve the above four aspects and to better understand the implications of pore pressure for the slip behavior of the plate interface, this Ph.D. study investigated the pore pressure in the Nankai Trough, North Sumatra and North Hikurangi subduction zones, using multiple approaches involving consolidation experiments, empirical equations, critical state soil mechanics and numerical modeling (Figure 1-2).

In the Nankai Trough subduction zone, recent International Ocean Discovery Program (IODP) Expedition 370 penetrated the décollement and recovered sediments from the accretionary prism, underthrust section and major reverse fault zone (Heuer et al., 2017). This provides the unique opportunity to estimate the pore pressure in the accretionary prism and fault zone by experimental approach such as consolidation tests. Further, anomalously low chlorinity has been revealed along the décollement in the Nankai Trough (Heuer et al., 2017) and can be used to constrain the fault zone pore pressure by numerical modeling. Also, as one of the best-studied subduction zone, abundant consolidation experiments have been conducted on samples from the Nankai Trough, which makes Nankai Trough the best area to investigate the effects of consolidation state on pore

pressure prediction. Therefore, Nankai Trough was selected as a research area, in order to provide new insights into aspects (1) and (2).

In the North Sumatra subduction zone, coseismic slip in the Mw 9.2 2004 Sumatra-Andaman earthquake propagated to the trench and triggered devastating tsunami (Ammon et al., 2005). Seismic profile shows that the incoming sequence is as thick as 5 km at the deformation front (Dean et al., 2010). This makes coring the sediments close to the décollement impossible and increases the difficulty of predicting pore pressure around the rupture area. However, recent IODP Expedition 362 recovered the sediment succession before entering into the subduction zone (McNeill et al., 2017a) and provided critical information to constrain the evolution of sedimentation and silicate dehydration in clay-rich sediment (Hüpers et al., 2017). Combining the parameters that can be acquired from consolidation experiments, these basic data can be employed to simulate the pore pressure evolution in the North Sumatra subduction zone. The modeling result will answer whether large slip near the trench can be explained by pore pressure estimates. Further, the established pore pressure evolution model is capable of quantifying the relative contribution of different mechanisms to excess pore pressure generation. Therefore, North Sumatra was selected as a research area, aiming at promoting our knowledge in aspects (3) and (4).

In the North Hikurangi subduction zone, slow slip events (SSEs) recur every 1-2 years (Wallace, 2020). Recent IODP Expedition 375 has recovered core samples from both frontal accretionary prism and incoming sediments (Saffer et al., 2019). By using consolidation experiments and porosity-based method, pore pressure in the North Hikurangi subduction zone can be computed. Together with the pore pressure estimates in the Nankai accretionary prism, the results from North Hikurangi will provide quantitative evidence for characterizing the pore pressure state in the accretionary prism. In addition, the pore pressure results can be utilized to illuminate its relationship with SSEs. To explain the occurrence of SSEs, Im et al. (2020) recently proposed a numerical model to simulate SSEs. By combining the pore pressure results and the numerical model, the effects of pore pressure on SSEs can be investigated. Therefore, North Hikurangi was selected as a research area, with the goal of improving our understanding in aspects (1) and (4).

1.4 Outline of this Cumulative Dissertation

The work in this Ph.D. dissertation was conducted at the MARUM – Center for Marine Environmental Sciences, University of Bremen, under the supervision of Prof. Dr. A. J. Kopf and Dr. A. Hüpers. The samples used in this Ph.D. study were acquired from the IODP Expeditions 370, 362 and 375. The research outcome is presented in four first-authored manuscripts which constitute this cumulative dissertation. This Ph.D. dissertation is divided into six chapters and the main content of each chapter is summarized as follows.

Chapter 1: As shown above, this chapter reviews the state-of-the-art research on earthquakes and pore pressure in subduction zones, summarizes the aspects which can be improved by this Ph.D.

study, explains how the research area is selected, outlines the main content of each chapter and describes my detailed contribution to each manuscript.

Chapter 2: This chapter focuses on the investigation of pore pressure in the Nankai Trough. Robust estimates of pore pressure are provided for both the accreting and subducting sediments in the shallow Nankai Trough subduction zone, based on consolidation experiments and numerical models. Continuous excess pore pressure is found in the accreted and underthrust sediments and implies the Nankai décollement is not a fluid barrier. Pore pressures 84%-93% of the lithostatic stress along the décollement are revealed and lead to the shear strength of Nankai subduction thrust as low as 0.4-0.8 MPa, which may facilitate the propagation of seismic slip to the trench and thus a catastrophic tsunami offshore SW Japan. This work has been published on *Journal of Geophysical Research-Solid Earth*.

Chapter 3: This chapter presents the porosity-based pore pressure prediction approach modified from Flemings and Saffer (2018) based on critical state soil mechanics. The modified method considers the consolidation state of sediments and investigates the effects of consolidation state on pore pressure estimates. Compared with the normally consolidated sediment, the overconsolidated sediment in the Nankai Trough generates 40%~50% less excess pore pressure and the pore pressure estimates are consistent with experimental data. Based on the results, the mechanical properties of the Nankai décollement are quantified. The shear strength along the décollement is below 2.2 MPa, obviously larger than the shear stress (<0.4 MPa). This implies that the accretionary prism is not at Coulomb failure, which is in good agreement with the dynamic Coulomb wedge theory (Wang & Hu, 2006).

Chapter 4: This chapter focuses on the investigation of pore pressure in the North Sumatra subduction zone. Present pore pressure in the incoming sequence is calculated, and the pore pressure evolution in a horizon which is considered as potential candidates for the localization of the décollement (Dean et al., 2010) is simulated. Based on consolidation experiments and numerical models, mainly hydrostatic to low excess pore pressure is inferred in future accreted section at IODP Sites U1480 and U1481, while the pre-décollement horizon shows moderate excess pore pressure. A one-dimensional sedimentation-flow model which accounts for the sedimentation rate and silicate dehydration demonstrates that the moderate excess pore pressure is attributed to both rapid sedimentation rate and silicate dehydration. Pore pressure in the pre-décollement horizon reaches >90% of the lithostatic stress before plate subduction. This study suggests that the high excess pore pressure in the near-trench faults may facilitate the propagation of coseismic slip all the way to the trench and increase the tsunami size, when the 2004 great Sumatra-Andaman earthquake nucleates.

Chapter 5: This chapter focuses on the investigation of pore pressure in the North Hikurangi subduction zone. Consolidation experiments on samples from Site U 1520 suggest that the sediment in trench-wedge facies is underconsolidated, whereas that in pelagic and volcaniclastic

facies is overconsolidated. At Site U1518, porosity-based pore pressure prediction approach shows that the frontal accretionary prism is widely overpressured. Further, pore pressure 77% of lithostatic stress is revealed at the top of the Pāpaku fault, while the pore pressure at the bottom increases to 93% of lithostatic stress. This provides plausible explanation for the mixed deformation styles observed on the Pāpaku splay fault (Fagereng et al., 2019), and explains the frequent slow-slip events (SSEs) in the Northern Hikurangi subduction zone. The numerical simulation of SSEs indicates that the stress drop, peak slip velocity and recurrence interval of SSEs decrease with increasing pore pressure.

Chapter 6: This chapter summarizes the main conclusions of this Ph.D. dissertation and presents an outlook for the future research on pore pressure and fault slip behavior in subduction zones.

1.5 Contribution to the Manuscripts

Manuscript I: Pore Pressure Regime and Fluid Flow Processes in the Shallow Nankai Trough Subduction Zone Based on Experimental and Modeling Results from IODP Site C0023

J. Zhang prepared all the 11 samples, conducted all the experiments, wrote the MATLAB code for data processing, processed all the data, performed all the calculations, developed the numerical model for fluid flow, wrote the MATLAB code for numerical modeling, interpreted the data, prepared all the figures, wrote and revised the manuscript.

A. Hüpers helped in the preparation and experiments of the first two samples, proposed the initial numerical model for fluid flow, wrote the initial MATLAB code for numerical modeling, interpreted the data, and revised the manuscript. S. Kreiter and A. Kopf contributed to the interpretations and revised the manuscript.

Manuscript II: The Effect of Consolidation State on Pore Pressure Prediction in an Accretionary Prism Using a Porosity-Based Critical State Soil Mechanics Approach

J. Zhang derived the pore pressure prediction model for overconsolidated sediments, established the velocity-porosity transform equation, performed all the calculations, wrote the MATLAB code for two-dimensional pore pressure prediction, interpreted the data, prepared all the figures, wrote and revised the manuscript.

A. Hüpers, S. Kreiter and A. Kopf initiated the idea of developing a new model based on the work of first manuscript, contributed to interpretations and revised the manuscript. T. Tsuji provided the velocity data, contributed to interpretations and revised the manuscript.

Manuscript III: Pore Pressure Prediction and Modeling in the North Sumatra Subduction Zone: Implications for Tsunami Hazard

J. Zhang prepared all the 17 samples, conducted all the experiments, wrote the MATLAB code for data processing, processed all the data, performed all the calculations, established the

sedimentation-flow model, wrote the MATLAB code for numerical modeling, interpreted the data, prepared all the figures, wrote and revised the manuscript.

A. Hüpers and A. Kopf contributed to the interpretations and revised the manuscript. H. Li contributed to the discussion of the sedimentation-flow model and revised the manuscript.

Manuscript IV: Pore Pressure Prediction in the North Hikurangi Subduction Zone: Implications for Slow Slip Events

J. Zhang prepared all the 9 samples, conducted all the experiments, wrote the MATLAB code for data processing, processed all the data, performed all the calculations, modified the MATLAB code for slow slip event modeling written by Im et al. (2020), performed the slow slip event modeling, interpreted the data, prepared all the figures, wrote and revised the manuscript.

A. Hüpers, M. Ikari and A. Kopf contributed to the interpretations and revised the manuscript.

Chapter 2: Pore Pressure Regime and Fluid Flow Processes in the Shallow Nankai Trough Subduction Zone Based on Experimental and Modeling Results from IODP Site C0023*

Junli Zhang, Andre Hüpers, Stefan Kreiter, and Achim J. Kopf

MARUM—Center for Marine Environmental Sciences and Faculty of Geosciences, University of Bremen, Bremen, Germany

Corresponding author: Junli Zhang (jzhang@marum.de)

*An edited version of this paper was published by AGU. Copyright 2021 American Geophysical Union.
Citation: Zhang, J., Hüpers, A., Kreiter, S., & Kopf, A. J. (2021). Pore pressure regime and fluid flow processes in the shallow Nankai Trough subduction zone based on experimental and modeling results from IODP Site C0023. *Journal of Geophysical Research: Solid Earth*, 126, e2020JB020248. https://doi.org/10.1029/2020JB020248

Abstract

Pore fluid pressure is a critical parameter controlling the dynamics of subduction zones and related geological hazards, but quantitative constraints on pore pressure are sparse. Here we provide robust estimates of pore pressure in the shallow Nankai Trough subduction zone based on consolidation experiments and numerical models. Our experimental data reveal excess pore pressures with nearly constant ratios of pore pressure to lithostatic stress for the accreted and underthrust sediments, implying the décollement is not a fluid barrier as previously inferred. Also, our research suggests repeated lithostatic pore pressure transients in the last 3 kyrs, probably associated with the propagation of the frontal thrust. The coupled pore pressure dissipation and chemical transport model results let us conclude the updip migration fluid originates from an overpressured horizon nearby, confirming the view of a heterogeneous plate boundary with overpressured and permeable patches along the fault surface that shift in time and space. The resulting high excess pore pressure leads to the shear strength of Nankai subduction thrust as low as 0.4-0.8 MPa. This provides quantitative constraints on the weakness of subduction thrusts at the toe of accretionary prisms and may explain why seismic slip can propagate all the way to the trench in some earthquakes (e.g. 2011 Tohoku event).

2.1 Introduction

Recent subduction earthquakes such as the M_w 9.2 2004 Sumatra-Andaman (Ammon et al., 2005) and M_w 9.1 2011 Tohoku events (Fujii et al., 2011) triggered devastating tsunamis through large seafloor displacement caused by coseismic slip extending to the trench. The shallow slip challenges the prevailing model of plate boundary interface behavior in which the outer subduction thrust system behaves aseismically and any seaward rupture propagation should cease in velocity-

strengthening unconsolidated sediments (e.g., Moore & Saffer, 2001; Wang & He, 2008). Recent laboratory friction experiments show that propagation of earthquakes through these zones seems energetically favorable when the sediments are at low effective normal stress conditions (Faulkner et al., 2011). Therefore, pore fluid pressure plays a crucial role for fault mechanical behavior because it governs the effective normal stress and thus the absolute fault strength (e.g., Scholz, 1998; Kitajima & Saffer, 2012), as well as the nature of fault slip (e.g., Kodaira et al., 2004; Liu & Rice, 2007; Saffer & Tobin, 2011).

The presence of pore fluid pressure in excess of hydrostatic in shallow subduction zones has been inferred from the porosity profile of sediments having entered the subduction system (e.g., Moore & Vrolijk, 1992). Underthrust sediments show higher porosity than expected, which has been interpreted as an indicator of elevated pore pressure inherited from rapid vertical loading by the overriding wedge as well as inhibited drainage across the subduction thrust (e.g., Moore et al., 2001; Gamage & Screaton, 2006). In accreted sediments better drainage and additional tectonic compaction are supposed to cause lower porosities in comparison to reference sites outside the subduction system. The change of stress field compared to the references seaward of the accretionary prism, however, complicates pore pressure estimation. Most existing pore pressure studies circumnavigate this problem by calculating fluid sources from an assumed porosity field for the accreted sediments that in turn drive pore pressure in fluid flow models (e.g., Screaton et al., 1990; Bekins & Dreiss, 1992; Saffer & Bekins, 1998). In a recent study, Flemings and Saffer (2018) proposed a generalized porosity-based approach to predict pore pressure in accreted sediments by combining a critical state soil model and the knowledge of stress path of sediments entering an accretionary prism. This method takes the porosity loss driven by shear stress into consideration and provides a more constitutive relationship between porosity and stress. All these previous approaches have been used with success to understand the overall time-averaged pore pressure pattern in subduction zones. But they provide only limited insight into detailed pore pressure transients because of assumed priori stress states and porosity fields. The need for a better understanding of transient pore pressure becomes apparent by the discrepancy between predicted near lithostatic pore pressure and moderate excess pore pressure measured in sealed ocean drilling boreholes along the shallow plate interface of subduction zones (also called décollement). For example, pore pressure in Barbados accretionary complex is only one-third of the lithostatic stress (Becker et al., 1997).

Here, we focus on the Nankai Trough subduction zone where five $M_w \approx 8$ earthquakes in the last four centuries caused tsunamis (Ando, 1975). Numerous studies have investigated excess pore pressure in the shallow portion, but were either based on geophysical data (Bangs et al., 2004; Tsuji et al., 2008), time-averaged fluid flow models (e.g., Saffer & Bekins, 1998) or hydrogeological models focusing on the underthrust sequence (Screaton et al., 2002; Skarbek & Saffer, 2009). In a recent study, Park et al. (2014) showed a large portion of the shallow décollement in the Nankai Trough is characterized by impedance-decreases (Figure 2-1). They

explained the decreasing acoustic impedance with (1) a high-impedance accretionary prism versus a low-impedance underthrust section or (2) increase of pore pressure within the fault zone, which causes decreases of seismic velocity and thus reversal of acoustic impedance across the fault, as discovered in the Oregon accretionary prism (Tobin et al., 1994; Moore et al., 1995).

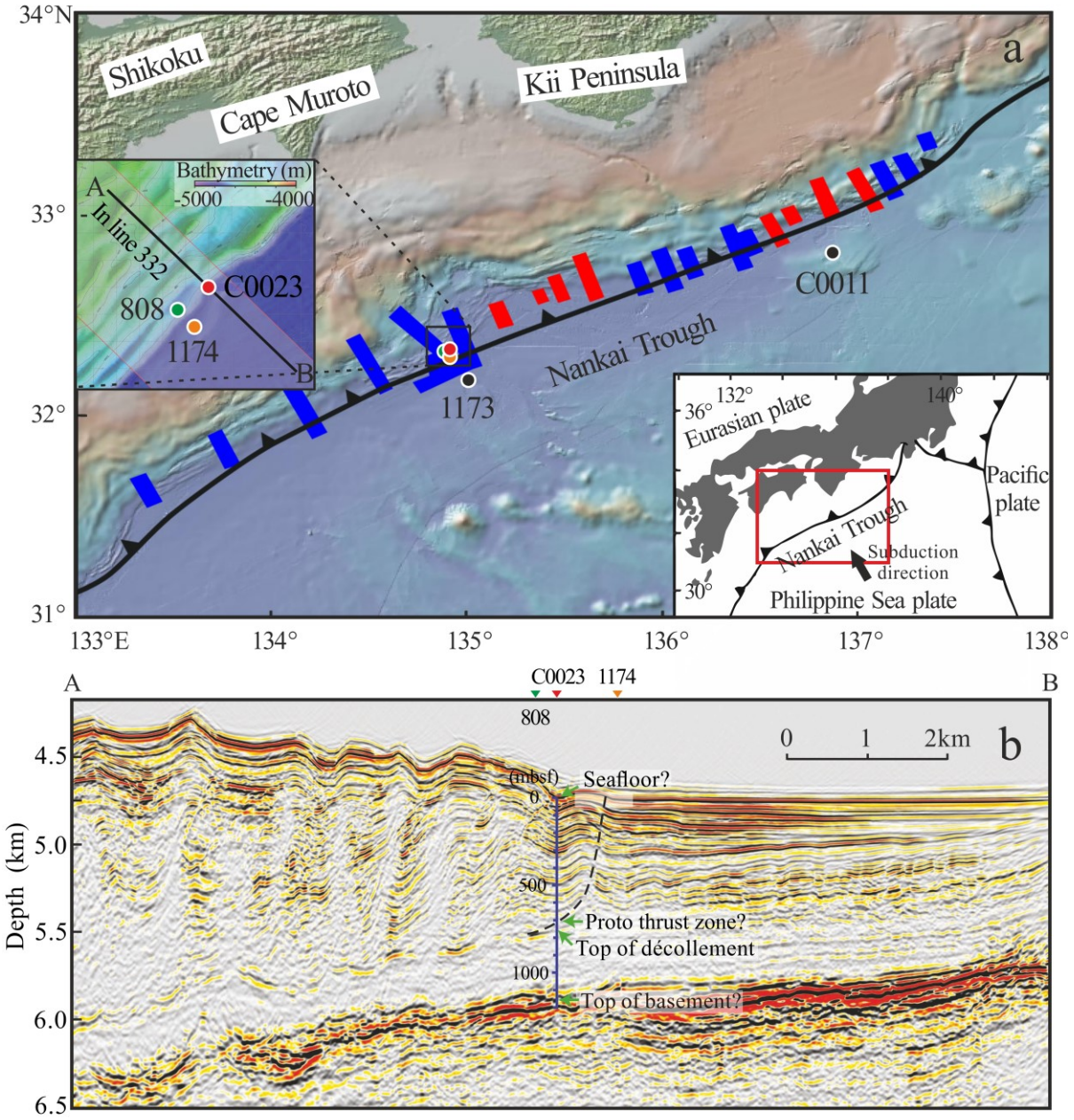

Figure 2-1. Geological setting of the study area and seismic section at the toe of the Nankai Trough accretionary prism off Muroto. (a) The locations of Nankai Trough and ODP/IODP drill sites after Heuer et al. (2017). Figure made with GeoMapApp (www.geomapapp.org; Ryan et al., 2009). Solid dots mark ODP Sites 808, 1173 and 1174, as well as IODP Sites C0011 and C0023. Thick blue bars mark décollements with reverse polarity reflections and red bars mark décollements with

normal polarity reflections after Park et al. (2014). Insets: The location of seismic line 332 after Heuer et al. (2017) and tectonic background of the Nankai Trough after Moore et al. (2001). (b) Pre-stack depth migrated 2D seismic section of Inline 332 in the area of Site C0023 after Heuer et al. (2017). Solid reverse triangles mark the position of Site C0023 and projected positions of Sites 808 and 1174. The dashed line marks the proto thrust zone.

To test if the shallow plate boundary in the Nankai Trough is overpressured, we collected samples at the top of the major reverse fault zone and conducted a multi-methodological approach, which takes into account the stress state of the incoming sediment, its stress path during burial and the timing of pore pressure build up. In addition to samples close to the décollement, we also sampled accreted and underthrust sediments to characterize the pore pressure regime in the whole sediment succession. For the pore pressure estimates, we conducted uniaxial consolidation experiments, which is a widely and successfully utilized method to derive in situ pore pressures (e.g., Saffer, 2003, 2007). The analysis of the data accounts for the compressive strengthening from secondary consolidation (creep) and diagenesis observed in the incoming sediments and the change of stress field in the prism sediments. We compared the inferred pore pressure estimates with those predicted from the recently developed critical state soil mechanics model by Flemings and Saffer (2018). Through a one-dimensional coupled pore pressure dissipation and chemical transport model, we also addressed the transient nature of pore pressure build up along the shallow décollement and constrained the timing of the fault activities.

2.2 Geological Setting

The central Nankai Trough subduction zone forearc, where the Philippine Sea plate is subducting to the northwest beneath the Eurasian plate (Figure 2-1), has been recently sampled at Site C0023 by the International Ocean Discovery Program (IODP) Expedition 370. The drill site is located on the frontal accretionary prism off Cape Muroto, ~2 km landward of the trench, and was established to investigate the limits of life in the deep subseafloor biosphere (Heuer et al., 2017). The sediment succession of Site C0023 is divided into 4 main lithostratigraphic units and consists of sediments offscraped from the Philippine Sea plate (Heuer et al., 2017). The lithostratigraphy is similar to that of nearby Ocean Drilling Program (ODP) Sites 1174 and 808, with a ~38 m thick décollement (Figure 2-2) located between 758 and 796 mbsf (meters below seafloor) in bioturbated hemipelagic mudstones of the Lower Shikoku Basin facies (Heuer et al., 2017).

Shipboard measured porosity and pore water geochemistry at Site C0023 (Figure 2-2) provide qualitative evidence for excess pore pressure and active fluid flow. According to the prevailing model of the shallow subduction zone hydrogeology, the porosity offset to higher values across the décollement is supposed to reflect high excess pore pressure in low permeable clay-rich underthrust sequence from rapid loading and inhibited fluid expulsion across the subduction thrust (e.g., Bray & Karig, 1988; Moore et al., 2001; Gamage & Screaton, 2006). The general chloride profile is similar to that of ODP Sites 1174 and 808 with a broad low-chloride anomaly, reflecting

fluid freshening by in situ clay dehydration and possibly an additional contribution of freshened fluids by updip migration (Saffer & Bekins, 1998; Saffer & McKiernan, 2009). A clear deviation from the general decreasing trend to lower Cl^- values between 600 and 780 mbsf at Site C0023 is indicative for a recent influx event of low Cl^- fluids and supports the proposed lateral migration of fluids formed by clay mineral dehydration at greater depth (Saffer & Bekins, 1998). In situ clay dehydration as an alternative explanation can be excluded because no significant increase in clay content is observed in the horizon (Heuer et al., 2017).

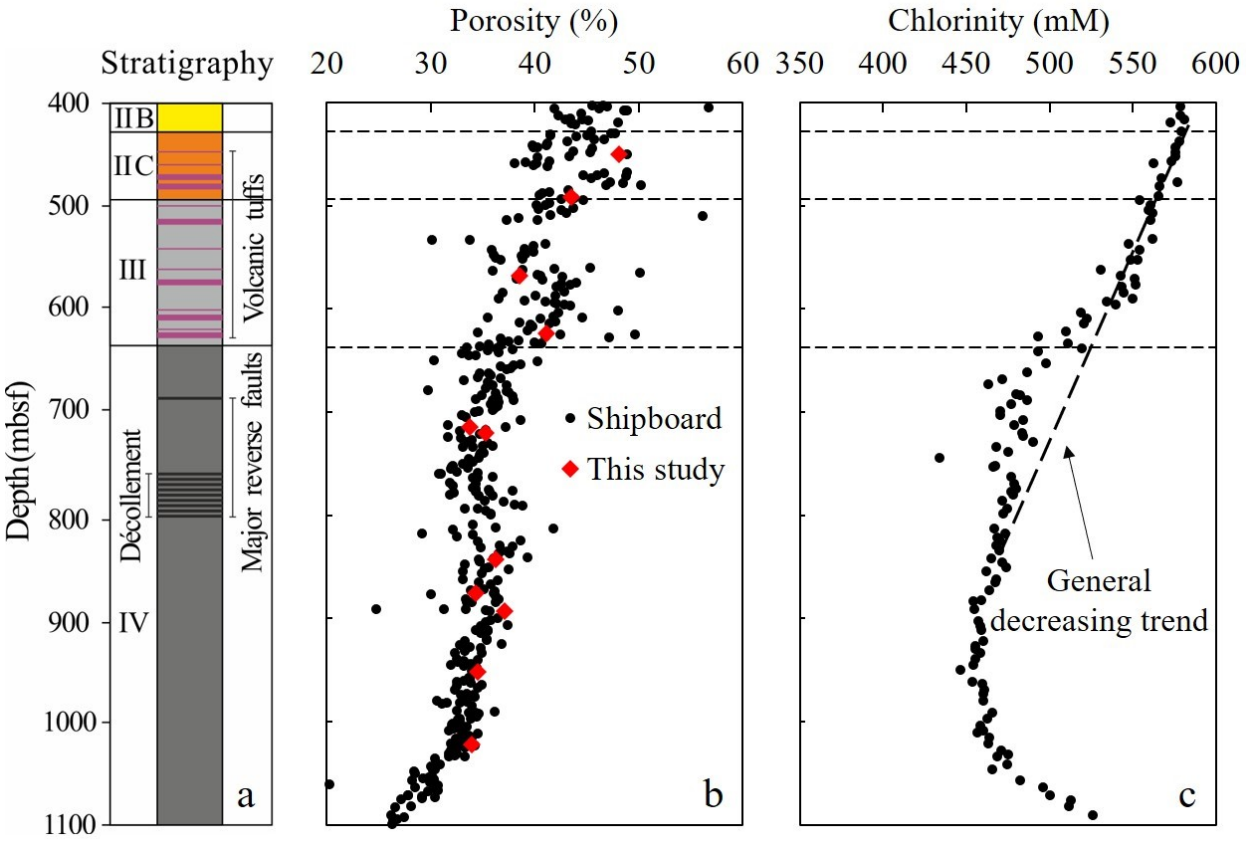

Figure 2-2. Lithostratigraphy (a), porosity (b) and chlorinity (c) profiles of IODP Site C0023 after Heuer et al. (2017). IIB: Outer trench-wedge facies, consisting of turbidite-deposited mudstones and thin sand beds; IIC: Trench-to-basin transitional facies, including turbidite-deposited and bioturbated mudstones, siltstones, and volcanic tuffs; III: Upper Shikoku Basin facies, mainly containing hemipelagic mudstones except <8% tuffs and tuffaceous sedimentary rocks; IV: Lower Shikoku Basin facies, composed of volcaniclast-bearing and heavily bioturbated hemipelagic mudstones.

2.3 Materials and Methods

2.3.1 Materials and Experimental Estimates of Pore Pressure

2.3.1.1 Theory of Consolidation Experiment and Sample Materials

Consolidation is the gradual volume reduction of fully saturated sediments with increasing effective stress (Terzaghi, 1943; Knappett & Craig, 2012). The consolidation characteristics of sediments can be assessed through an uniaxial consolidation experiment, e.g., the incremental loading oedometer test, the constant rate of strain loading test, and the one-dimensional consolidation test in a triaxial apparatus. For the incremental loading oedometer test, the specimen is held inside a confining ring and lies between two porous stones (Figure 2-3a). A loading cap sits on the upper porous stone and passes the applied load onto the specimen. The whole assembly is placed into an oedometer cell, which is filled with water and allows the water inside the specimen to drain out. With the increase of the applied load, the specimen is compressed, leading to the upper porous stone and loading cap moving down. The resulting displacement is recorded by a linear variable displacement transducer (LVDT). Because the confining ring prevents the specimen from lateral deformation, the strain is uniaxial and can be calculated by the vertical displacement. On the semi-logarithmic stress-strain plot, a yield point which separates the elastic from elasto-plastic deformation behavior can be identified (Figure 2-3b). This yield point is commonly regarded as the maximum vertical effective stress that the sediment has sustained and is termed preconsolidation stress $\sigma_{pc}^{'}$ (e.g., Casagrande, 1936). The sediment is said to be normally consolidated when the in situ vertical effective stress ($\sigma_{v}^{'}$) equals $\sigma_{pc}^{'}$ while it is called overconsolidated if $\sigma_{pc}^{'}$ is larger than $\sigma_{v}^{'}$ (e.g., Knappett & Craig, 2012). For sediments that have only experienced uniaxial consolidation (K_0 consolidation) and no unloading ever happened, $\sigma_{pc}^{'}$ is commonly interpreted as $\sigma_{v}^{'}$ (Saffer, 2003). Hence assuming $\sigma_{pc}^{'}$ is equal to $\sigma_{v}^{'}$, the pore pressure *P* can be computed based on Terzaghi's effective stress theory:

$$P = \sigma_v - \sigma_{pc}^{'} \tag{2-1}$$

where σ_v is the lithostatic stress calculated by shipboard measured bulk density data (e.g., Dugan & Germaine, 2008).

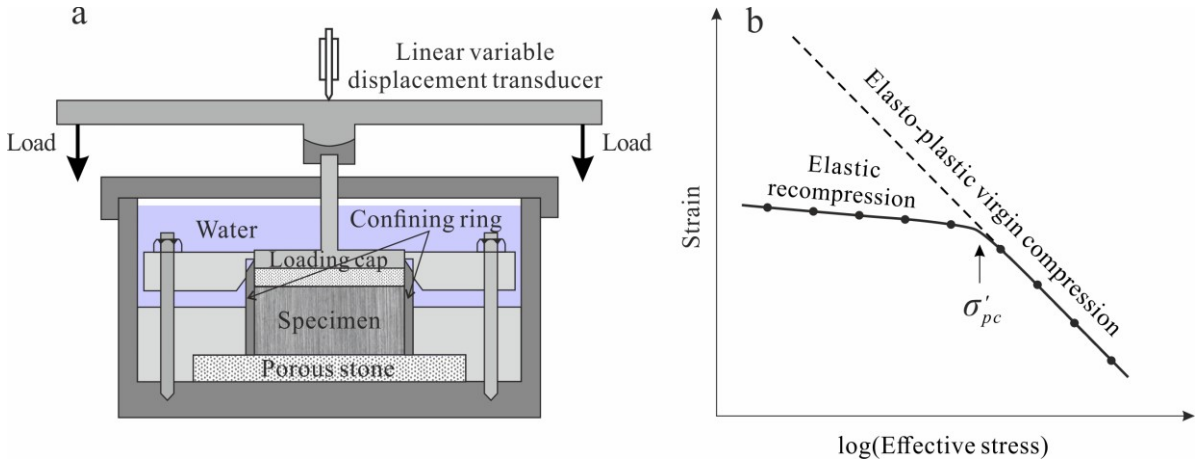

Figure 2-3. Schematic illustration of oedometer apparatus (a) and idealized compression behavior during oedometer tests showing preconsolidation stress (b).

For this study, a total of 11 specimens sampled from 450 to 1022 mbsf at Site C0023 (Table S2-1) were tested by incremental loading consolidation experiments following ASTM D2435/D2435M-11 (ASTM International, 2011). In order to maintain the natural water content, all samples were sealed and stored in the core liner at 4 ℃ before testing. The specimens were trimmed into cylinders with a diameter of 25.4 mm and a height of ~10 mm and were kept saturated in a fixed ring oedometer using an artificial seawater brine (35‰). The inner surface of the confining ring was highly polished and coated with silicone grease to minimize the effects of friction between the specimen and confining ring. In order to avoid intrusion of sediments into the pores of the porous stone, filter screens were placed between the specimen and the porous stones. During our consolidation experiments, we firstly doubled the load and then used small increments in the vicinity of σ'_{pc} so that the transition between the recompression and virgin compression lines could be determined with more precision (e.g., Brumund et al., 1976). Although σ'_{pc} was unknown before the experiments, we utilized hydrostatic vertical effective stress (σ'_{vh}) which was calculated by subtracting hydrostatic pore pressure from σ_v as a reference. For each load, a constant load increment duration of 24 h was performed to allow complete dissipation of excess pore pressure. Vertical load and sample height were continuously recorded throughout the experiments.

In this study, we determined σ'_{pc} using a modification of the widely used Casagrande method (Casagrande, 1936; McNulty et al., 1978). However, due to the scale dependence of σ'_{pc} by graphical construction (Clementino, 2005), we also used the Pacheco Silva method (1970) to estimate σ'_{pc} for comparison since it requires only modest subjective interpretation (Grozic et al., 2005). Moreover, we determined the confident range of σ'_{pc} by estimating the maximum and minimum possible σ'_{pc} values. The maximum σ'_{pc} was acquired from effective stress on the

stress-strain plot at which the strain begins to deviate from the virgin compression line (e.g., Saffer, 2003). Similarly, the minimum σ'_{pc} can be given by the first point deviating from the recompression line. However, this method produces over-conservative estimates of minimum σ'_{pc} because the starting stress of transition from recompression to virgin compression is significantly lower than σ'_{pc}. For example, Jacobsen (1992) proposed $\sigma'_{pc} = 2.5\,\sigma'_{k}$, where σ'_{k} is the point with maximum curvature in Casagrande method and also larger than the starting stress of transition from recompression to virgin compression. Therefore, we plotted our consolidation data with the work-stress method (Becker et al., 1987) and extrapolated post-yield line (corresponding to virgin compression line in Casagrande method) to zero work. The intersection of zero work line and post-yield line was interpreted as the minimum σ'_{pc} (e.g., Santagata & Germaine, 2002; Dugan & Germaine, 2008). The estimating procedures for the modified Casagrande method and all laboratory data are shown in the supplementary material (Text S2-1, Table S2-2 and Figures S2-1 and S2-2) and available in Zhang (2020).

2.3.1.2 Correction for Secondary Consolidation and Diagenesis

Although equation (2-1) was successfully used to infer pore pressure (e.g., Saffer, 2003; Dugan & Germaine, 2008), it has been recognized that secondary consolidation and diagenesis could shift σ'_{pc} to higher values (e.g., Bjerrum, 1973; Morgan & Ask, 2004). In this study, we accounted for these effects and corrected σ'_{pc}. The quantitative relation between σ'_{pc} and σ'_{v} is given by the overconsolidation ratio (OCR):

$$OCR = \frac{\sigma'_{pc}}{\sigma'_{v}} \tag{2-2}$$

For normally consolidated sediments OCR equals unity, whereas for sediments subjected to unloading, through erosion for example, OCR is larger than unity (e.g., Knappett & Craig, 2012). OCR > 1 is also possible when secondary consolidation (creep), cementation or thixotropy causes a strengthening of the sediment (e.g., Bjerrum, 1973; Locat & Lefebvre, 1986). Strictly speaking, OCR can never be less than one (e.g., Knappett & Craig, 2012). However, many authors replaced σ'_{v} by σ'_{vh} in equation (2-2) to calculate OCR owing to difficulty in obtaining σ'_{v} and presented OCR<1 (e.g., Saffer, 2003; Kitajima & Saffer, 2014). Here we used the strict definition of OCR (equation (2-2)).

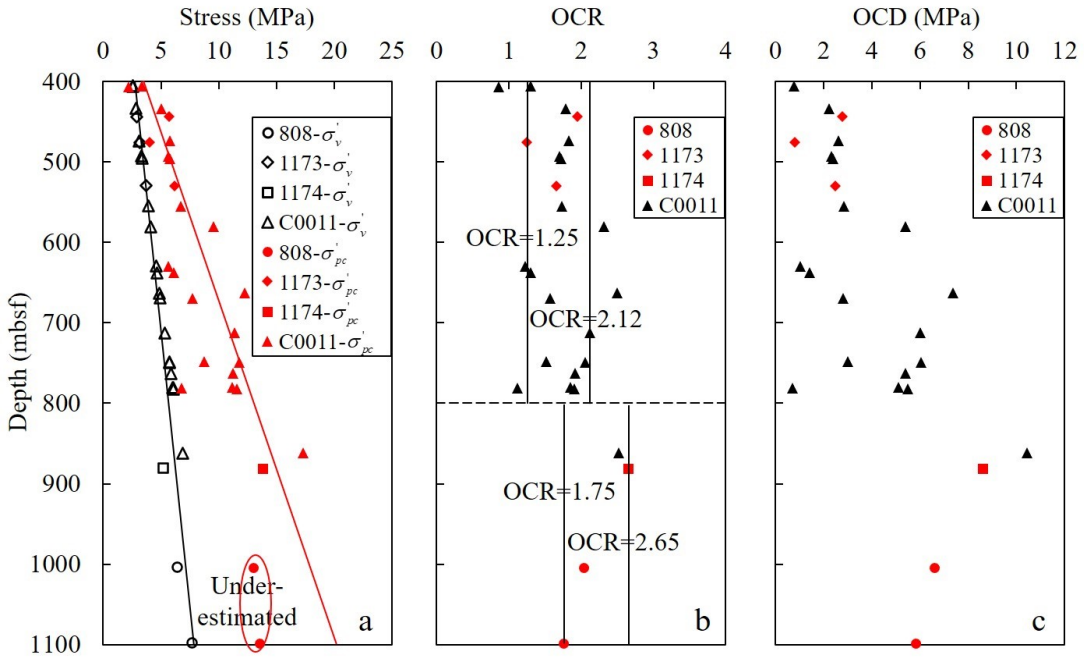

Figure 2-4. Profiles of in situ vertical effective stress and preconsolidation stress (a), OCR (b) and OCD (c) in the Nankai Trough. Data are collected from Morgan and Ask (2004), Bellew (2004), Hüpers and Kopf (2012), Guo and Underwood (2014) and Kitajima and Saffer (2014). OCR (overconsolidation ratio) = σ'_{pc}/σ'_{v}; OCD (overconsolidation difference) = $\sigma'_{pc} - \sigma'_{v}$. Dashed line marks the depth where an obvious increase in the measured percentages of illite in illite/smectite mixed-layer clays is observed (Steurer & Underwood, 2003), which may strengthen the sediment. Note that the preconsolidation stress generally increases linearly with depth except for the two data points from Site 808 which are obviously underestimated.

Previous consolidation tests on sediments from reference Sites 1173 and C0011 and the underthrust section of Sites 808 and 1174 (Morgan & Ask, 2004; Bellew, 2004; Hüpers & Kopf, 2012; Guo & Underwood, 2014; Kitajima & Saffer, 2014) have revealed OCR values mainly ranging from 1.2 to 2.3 in the Nankai Trough (Figure 2-4 and Table S2-3). The σ'_{v} values at reference Sites 1173 and C0011 were inferred from σ'_{vh} since low sedimentation rates prevented pore pressure in excess of hydrostatic (e.g., Screaton et al., 2002; Kitajima & Saffer, 2014), whereas at Sites 808 and 1174, σ'_{v} was estimated by inversion of porosity data using a solid porosity versus effective stress relationship (e.g., Screaton et al., 2002; Morgan & Ask, 2004). Both secondary consolidation and diagenesis have been invoked to explain the OCRs >1 (Hüpers & Kopf, 2009; Morgan & Ask, 2004). Secondary consolidation results in continuous settlement under constant effective stress, which enhances the stiffness of sediments (Karig & Ask, 2003) and shifts the yield point in consolidation test to higher effective stress (Figure 2-5). For sediments subject to diagenesis e.g. cementation, the intergranular bonding strengthens the sediment matrix

and further increases σ'_{pc} (Morgan & Ask, 2004). In contrast, overconsolidation driven by lateral tectonic force is negligible because the underthrust section in subduction zones and reference sites are widely considered to deform in uniaxial compression (e.g., Skarbek & Saffer, 2009; Screaton et al., 2002). To investigate the mechanism for the strength evolution with increasing burial, Perret et al. (1995) compiled a set of parameters with idealized subseafloor profiles. In addition to OCR, they used σ'_v and σ'_{pc} profiles as well as the overconsolidation difference (OCD) which is defined as OCD = $\sigma'_{pc} - \sigma'_v$ (Olsen et al., 1986). According to those authors, secondary consolidation leads to a constant OCR with depth, while σ'_{pc} and OCD increase linearly versus depth with gradients higher than those for normally consolidated sediment. We note that the Nankai inputs generally have similar character to this pattern with an average OCR of 1.76, although the data show a considerable scatter. The latter can be explained by the formation and breakdown of structural links built by cementation, which have been observed by previous studies (e.g., Steurer & Underwood, 2003; Hüpers et al., 2015; Sample et al., 2017). The slight increase of OCR with depth may also be related to the progressive diagenesis at greater depth (Morgan & Ask, 2004).

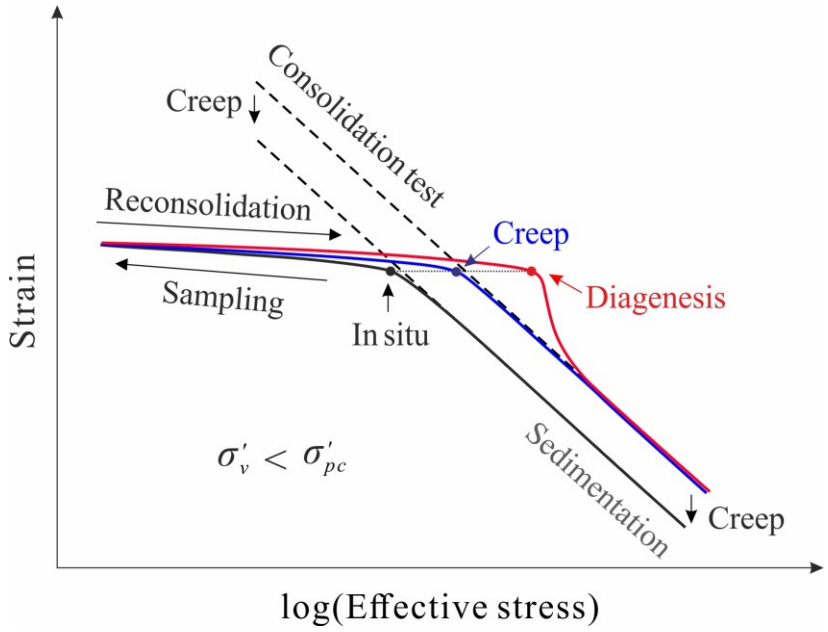

Figure 2-5. Schematic plot of elevated preconsolidation stress by secondary consolidation (creep) and diagenesis. The black point represents the in situ vertical effective stress. The blue and red points represent the elevated preconsolidation stress caused by secondary consolidation and diagenesis, respectively.

Our assessment of the available preconsolidation stresses for the Nankai inputs shows that the assumption of normally consolidated sediments does not apply (Figure 2-4). Secondary consolidation and diagenesis have shifted the yield point in consolidation tests to higher stresses,

which has to be addressed in the calculation of pore pressure from σ'_{pc}. We therefore modified equation (2-1) to account for the increase in σ'_{pc} by employing equation (2-2) to calculate σ'_v:

$$P = \sigma_v - \frac{\sigma'_{pc}}{OCR} \tag{2-3}$$

Because a solid relationship between OCR and depth is absent, we divided the Muroto transect into two sections. The boundary between the two sections was set at 800 mbsf where an obvious increase is observed in the measured percentages of illite in illite/smectite mixed-layer clays (Steurer & Underwood, 2003). The growth of authigenic illite (e.g., Morgan & Ask, 2004) and possible precipitation of quartz (e.g., Thyberg & Jahren, 2011) during enhanced smectite-to-illite transformation are expected to strengthen the sediment. Therefore an average OCR of 1.54 from reference Site 1173 at similar depth (Morgan & Ask, 2004; Bellew, 2004) was used for the upper section, whereas for the lower section an higher average OCR of 2.14 was utilized based on subducted samples from nearby Sites 1174 and 808 (Morgan & Ask, 2004). To understand the effects of OCR values on pore pressure estimates, we calculated the error bar by employing a minimum and maximum OCR value for both upper and lower sections, respectively. Due to the complexity of OCR values, the minimum and maximum OCR (1.25 and 2.12) were determined at values covering 90% of all published data for the upper section (Figure 2-4b). However only several published data were available in the lower section so that we used the minimum and maximum OCR values (1.75 and 2.65) directly for the lower section.

2.3.1.3 Correction for Stress Field

For the analysis of the samples from the accreted section, an additional correction is required because the lateral tectonic force changes the in situ triaxial stress state in the accretionary prism (e.g., Moran et al., 1993; Moore & Tobin, 1997; Tsuji et al., 2008). As a result the maximum principal stress has probably a horizontal orientation and the overburden corresponds to the minimum principal stress (Figure 2-6), which would lead to an underestimation of the pore pressure. To overcome this problem, Moore and Tobin (1997) directly interpreted σ'_{pc} as the horizontal maximum principal effective stress in the prism. In contrast, building on the observation that porosity loss is caused by the mean effective stress increase (Figure 2-6), we calculated the mean effective stress at yield point using σ'_{pc}. Because the consolidation test is widely regarded as K_0 consolidation and has a constant stress ratio (K_0) of horizontal to vertical effective stress, the mean effective stress can be estimated by:

$$\sigma'_{mpc} = \frac{\sigma'_{pc}}{OCR} \cdot \frac{1+2K_0}{3} \tag{2-4}$$

where σ'_{mpc} is the mean effective stress at the yield point. If we assume the intermediate principal effective stress equals the minor principal effective stress in accretionary prism, the in situ mean effective stress can be calculated by:

$$\sigma'_m = \sigma'_v \cdot \frac{1+2K_{in}}{3K_{in}} \tag{2-5}$$

where σ'_m is the in situ mean effective stress and K_{in} is the in situ stress ratio of minor to maximum principal effective stress. Assuming the mean effective stress at the yield point in the consolidation tests (σ'_{mpc}) is equal to the in situ mean effective stress in accretionary prism (σ'_m), the following expression is obtained when σ'_v is replaced by $\sigma_v - P$:

$$(\sigma_v - P) \cdot \frac{1+2K_{in}}{3K_{in}} = \frac{\sigma'_{pc}}{OCR} \cdot \frac{1+2K_0}{3} \tag{2-6}$$

Then the pore pressure in accretionary prism is estimated by transforming equation (2-6) into:

$$P = \sigma_v - \frac{\sigma'_{pc}}{OCR} \cdot \frac{K_{in}(1+2K_0)}{1+2K_{in}} \tag{2-7}$$

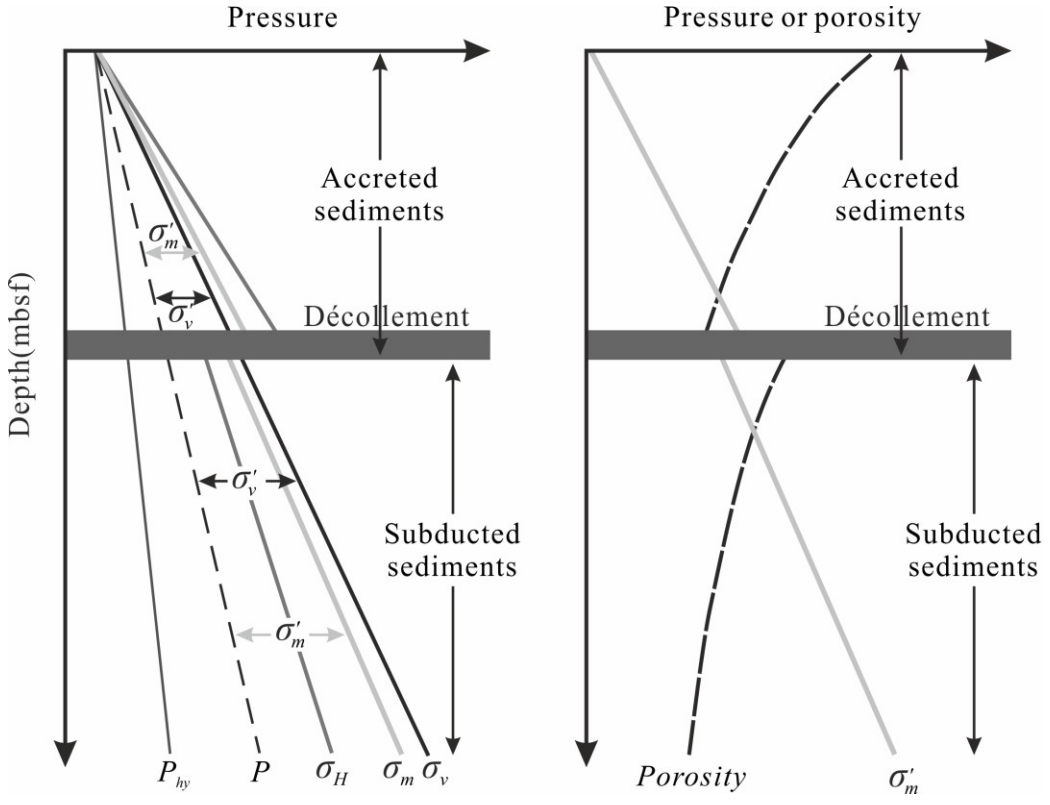

Figure 2-6. Conceptual profiles of pressures and porosity in the shallow subduction zones. Pore

pressure (P) profile is based on the results of this research and may differ in different subduction zones. P_{hy}: hydrostatic pore pressure; σ_H : horizontal stress; σ_m : mean total stress.

In our calculations, we used a K_0 = 0.81 for consolidation tests (Morgan & Ask, 2004) and K_{in} = 0.5 for in situ conditions (Moran et al., 1993) that were experimentally determined for accretionary prism samples from Sites 1174 and 808, respectively. Both K_0 = 0.81 and K_{in} = 0.5 are similar to the calculated stress ratios (K_0 = 0.90, K_{in} = 0.59) based on the numerical model by Flemings and Saffer (2018) using a sediment friction angle of 15° (Casey et al., 2016). To evaluate the effect of stress ratios on pore pressure estimates, we also calculated the maximum and minimum K_0 and K_{in} values with a sediment friction angle of 5°-30° after Flemings and Saffer (2018) by the numerical model. Stress ratios of K_0 = 0.64-0.99 and K_{in} = 0.33-0.84 were used to quantify the uncertainty of estimated pore pressures.

2.3.2 Numerical Estimates of Pore Pressure

To get a continuous insight into pore pressure variations at Site C0023, we compared our results with a recently developed method for pore pressure prediction by Flemings and Saffer (2018). In contrast to previous approaches, this method is built on the Modified Cam Clay (MCC) critical state model under plane stain conditions (Roscoe & Burland, 1968) and allows also the prediction of pore pressure in the prism sediments.

The method contains two models for the accreting sediments: an intact sediment model and a weak fault model. Both models postulate that the maximum principal stress is horizontal whereas the minimum principal stress is vertical. The intact sediment model further assumes the accretionary prism is in a state of Coulomb failure and the stress state is fully controlled by the material's inherent properties, i.e., sediment friction angle and the porosity-mean effective stress relationship. Based on critical state soil mechanics, the pore pressure can be estimated by:

$$P = \sigma_v - (1\text{-}\sin\phi)\cdot e^{\frac{e_{\lambda\tau} - e_{in}}{\lambda}} \tag{2-8}$$

where ϕ is the friction angle of sediment material, e is Euler's number, e_{in} is void ratio, λ is the slope on the $\ln(\sigma_m^{'})$ - e_{in} plot for accreting sediments at Coulomb failure, and $e_{\lambda\tau}$ is the intercept at $\sigma_m^{'}$ = 1 MPa (see Flemings and Saffer (2018) for details). In contrast, the weak fault model hypotheses that the stress state is affected by the properties of faults such that the accretionary prism reaches Coulomb failure in advance due to preexisting weak faults or is not at Coulomb failure (Flemings & Saffer, 2018). Therefore, the friction angle of weak faults is introduced in the weak fault model and the pore pressure can be predicted by:

$$P = \sigma_v - (1 - \sin\phi_{wf}) \cdot e^{\frac{e_{\lambda wf} - e_{in}}{\lambda}} \quad (2\text{-}9)$$

where ϕ_{wf} is the friction angle of weak fault, $e_{\lambda wf}$ is the intercept at $\sigma_m^{'}$ = 1 MPa on the $\ln(\sigma_m^{'})$ - e_{in} plot for weak faults at Coulomb failure.

For the underthrust section, the method assumes the sediment is in a state of K_0 consolidation and it is converted into the widely used empirical logarithmic equation to calculate vertical effective stress by porosity (e.g., Skarbek & Saffer, 2009). The prediction equation with soil mechanic meaning is expressed as:

$$P = \sigma_v - \frac{2 \cdot e^{\frac{e_{\lambda K_0} - e_{in}}{\lambda}}}{1 + K_0} \quad (2\text{-}10)$$

where $e_{\lambda K_0}$ is the intercept at $\sigma_m^{'}$ = 1 MPa on the $\ln(\sigma_m^{'})$ - e_{in} plot for underthrust sediments at K_0 consolidation state.

Assuming the elastic deformation is negligible, the yield surface in mean effective stress-maximum shear stress space represents the iso-void ratio stress path (Wood, 1990), which makes the stress variation predictable when the sediment deforms under undrained condition. The MCC critical state model shows how to derive the $\ln(\sigma_m^{'})$ - e_{in} relationship at any stress state when that at one specific state is known (e.g., Azizi, 2000). In our calculations, we considered $e_{\lambda K_0}$ = 1.16 and λ = 0.463 inferred from reference Site 1173 by Flemings and Saffer (2018) as known parameters. A sediment friction angle of 15° (Casey et al., 2016) and a weak fault friction angle of 5° (Flemings & Saffer, 2018) were used to derive K_0, $e_{\lambda\tau}$, and $e_{\lambda wf}$ (see Flemings and Saffer (2018) for details). By transforming the shipboard porosity data at Site C0023 (Figure 2-2b) to void ratio, the pore pressure profile was obtained.

2.3.3 Coupled Pore Pressure Dissipation and Chemical Transport Model

A vertical one-dimensional coupled pore pressure dissipation and chemical transport model was established to constrain the pore pressure estimates along the major reverse faults. Specifically, we tested the hypothesis if the obtained pore pressure profile was affected by lateral fluid flow as indicated by the observed Cl^- anomaly between 600 and 780 mbsf.

A constant pore pressure gradient equivalent to the averaged pore pressure ratio ($\lambda_p = P/\sigma_v$) of 0.71 as described in section 4.1 was assigned to the model as initial pore pressure profile. For the initial Cl^- concentration, the general decreasing trend (Figure 2-2c) was assigned. Based on the fault-valve model (Sibson et al., 1988; Sibson, 1990), the fault permeability increases immediately

after fault activity due to the inherent roughness of natural rupture surfaces, which leads to the updip migration of overpressured fluids. The high pore pressure along faults, in turn, further enhances and maintains the fault permeability through reducing the effective stress (e.g., Fisher & Zwart, 1997). Under sufficient fluid source condition, the discharged fluids can be compensated by releasing fluid from the source and high pore pressure can exist for long periods of geologic time (Bredehoeft, 2009). In the Muroto transect, active smectite-to-illite transformation (Steurer & Underwood, 2003) in the downdip direction provides a potential fluid source for the maintenance of high pore pressure. Hence, we induced the duration of transience into our model, which represents the timescale of transient lateral fluid flow and was simulated by maintaining the lithostatic conditions over an extended period before we allowed pore pressure to dissipate. Modeling results have shown that pore pressures along the fault can rise rapidly to near lithostatic value (e.g., Bekins et al., 1995; Saffer & Bekins, 1998). We therefore simulated the transient lateral fluid flow by increasing pore pressures along faults to lithostatic and decreasing Cl^- concentrations to certain low values. However, this does not mean the lithostatic pore pressure exists throughout the subduction thrust since the fault zone is heterogeneous (Brown et al., 1994). Four temporarily active fault zones were assigned in our model because (1) we observed 4 low Cl^- concentration spikes in chlorinity profile, and (2) several reverse faults and shear fractures were found around each low Cl^- concentration spike. The timing of the fault activities was assigned separately based on the width of the spikes, given that older fault activity has more time to allow advection and diffusion of solutes and thus has wider spikes (e.g., Saffer & Bekins, 1998). When the transient lateral fluid flow ceases, the lithostatic pore pressure along faults starts to dissipate. We used the concentration profile of the inert Cl^- to constrain the pore pressure dissipation, given that the vertical fluid flow away from the fault zone drives the advection of solutes. Constant pore pressures and Cl^- concentrations were specified for both the top and bottom boundaries of this model under the assumption that transient fluid flow can only affect limited horizons within the timescale covered by the model due to low permeability.

The pore pressure dissipation is quantified by the differential equation of consolidation (Terzaghi, 1943):

$$\frac{\partial P}{\partial t} = c_v \cdot \frac{\partial^2 P}{\partial z^2} \tag{2-11}$$

where t is time, c_v is the coefficient of consolidation, and z is depth. We used a c_v = 0.0008 cm^2/s for outer trench-wedge and trench-to-basin transitional facies, c_v = 0.0028 cm^2/s for Upper Shikoku Basin facies, c_v = 0.0032 cm^2/s for faulting sediments of Lower Shikoku Basin facies and c_v = 0.0007 cm^2/s for underthrust sediments of Lower Shikoku Basin facies, calculated from our experimental data.

For the variation of Cl^- concentration in a water-saturated one-dimensional sediment column, we used the following differential equation (Boudreau, 1997):

$$\frac{\partial C}{\partial t} = D \cdot \frac{\partial^2 C}{\partial z^2} - v \cdot \frac{\partial C}{\partial z} \tag{2-12}$$

where C is interstitial solute concentration i.e. Cl^- concentration, D is the effective chemical diffusion coefficient, and v is velocity. D is determined by $D = D_0/(1-\log(n^2))$ (Boudreau, 1997), where D_0 is estimated after Boudreau (1997) using the temperature profile reported for Site C0023 in Heuer et al. (2017) and the porosity, n, is based on a robust polynomial regression of the porosity profile ($n = -5.776\times10^{-15}\cdot z^5 + 1.539\times10^{-11}\cdot z^4 - 1.410\times10^{-8}\cdot z^3 + 4.997\times10^{-6}\cdot z^2 - 6.595\times10^{-4}\cdot z + 0.485$, adjusted $R^2 = 0.98$). The velocity, v, is given by Darcy's law:

$$v = -\frac{k}{\eta_w n} \cdot \frac{\partial P}{\partial z} \tag{2-13}$$

where k is vertical permeability, computed by porosity based on the empirical equation (i.e., $\log(k) = -20 + 5.5\, n$) by Saffer and Bekins (1998) and η_w is the temperature dependent viscosity of pore water after Huyakorn and Pinder (1978). The porosity and permeability profiles were assumed constant in our model because of the limited time interval of 3 kyr covered by the model (section 4). We further neglected porosity rebound during transient unloading because of the small porosity change associated with it (e.g., Nobes et al., 1991). Also, the constant vertical permeability is consistent with the view that lateral fractures only affect horizontal permeability (Saffer, 2015).

Previous studies showed that the duration of transient lateral fluid flow varies from several years (e.g., Hiramatsu et al., 2005) to thousands of years (e.g., Henry, 2000; Howald et al., 2015), we therefore conducted sensitivity analysis using a duration of 10-1000 years for the transient lateral fluid flow. Meanwhile, we also tested an influx fluid with Cl^- concentrations from 350 to 430 mM. The best parameters which predict our experimental pore pressure estimates were determined and constraints on the timing of the fault activities were acquired by matching the modeled results to the observed data after a certain time step.

2.4 Results

2.4.1 Experimental Results and Numerical Pore Pressure Estimates

The compression index, Cc, and recompression index, Cr, are the slopes of the virgin elasto-plastic compression and elastic recompression lines on the logarithmic mean effective stress versus void ratio plot (Knappett & Craig, 2012). Our consolidation tests yielded Cc and Cr values mainly in the range of 0.11-0.34 and 0.01-0.03, respectively.

In this study, the modified Casagrande method (McNulty et al., 1978) and Pacheco Silva method (1970) produced similar pore pressure estimates. The pore pressure difference between these two methods is lower than 0.7 MPa and the maximum difference as a percentage is 5.6% (Figure 2-7c). For the convenience of comparison with other studies, only results by the modified Casagrande method are described.

The consolidation tests conducted on 4 accreted sediment samples from Upper Shikoku Basin facies to outer trench-wedge facies (Unit III to IIB) yielded pore pressure in excess of hydrostatic (Figure 2-7c). The experimentally determined excess pore pressure varies from 1.3 MPa at 491 mbsf to 2.3 MPa at 568 mbsf. The pore pressures increase linearly with depth with a slope larger than hydrostatic, which corresponds to a narrow pore pressure ratio range of 0.69-0.76 (Figure 2-7d). In comparison, our numerical approaches predict similar pore pressures for the weak fault model, whereas in the absence of weak faults, the intact sediment model results in higher pore pressure ratios (λ_p = 0.71-0.85).

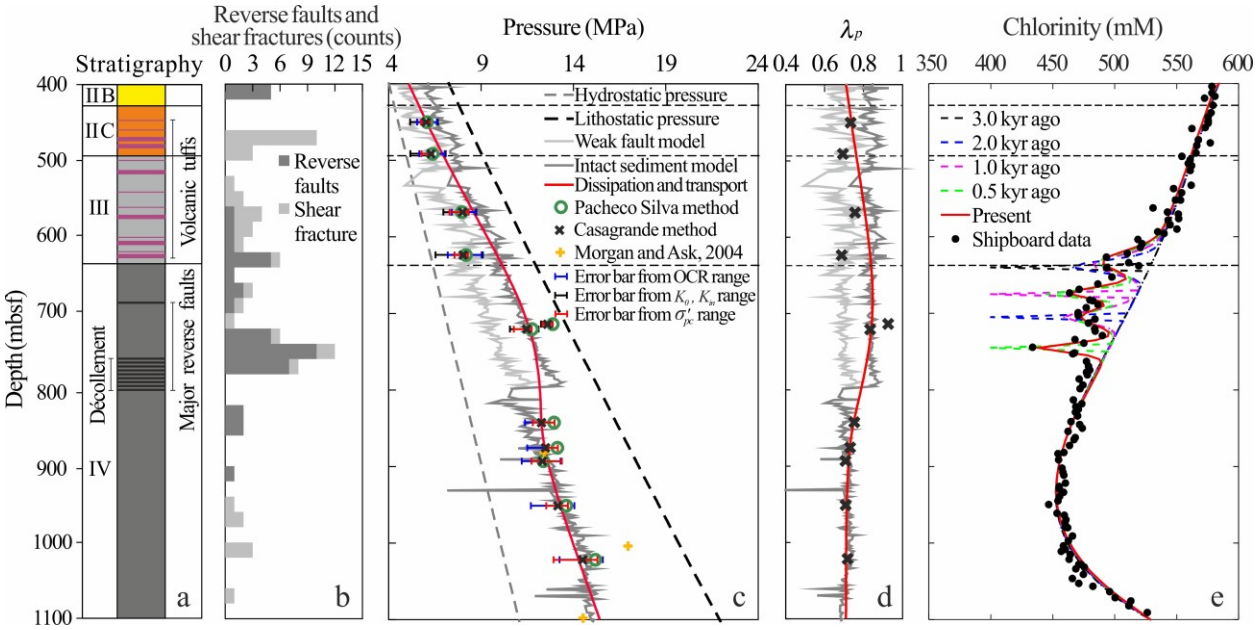

Figure 2-7. Lithostratigraphy (a), number of reverse faults and shear fractures (b), pore pressure estimates (c), estimated pore pressure ratio λ_p (d) and modelled chlorinity profiles (e) of IODP Site C0023. Number of reverse faults and shear fractures is from Heuer et al. (2017). The experimental pore pressure estimates in the major reverse fault zones did not account for secondary consolidation and diagenesis and were calculated by equation (2-7) with OCR = 1. Cl^- transport modeling fits the laboratory data best when assuming a duration of 100 years for transient lateral fluid flow and influx of a low Cl^- (400 mM) fluid along faults at 3.0 kyrs, 2.0 kyrs, 1.0 kyrs and 0.5 kyrs before present, respectively. Note that the model does not predict the long-term evolution of the pore pressure profile.

For the underthrust sequence, the experimental data also revealed pore pressure in excess of hydrostatic (Figure 2-7c). A total of 5 samples were tested for the subducted Lower Shikoku Basin facies with excess pore pressures ranging from 3.4 MPa to 4.2 MPa between 843 mbsf and 1022 mbsf. The pore pressure ratios are in range of 0.71-0.75 (Figure 2-7d). Although the excess pore pressures for subducted sediments are higher than those for the accreted section, their corresponding pore pressures follow the same increasing trend with depth. Again, our modeling results show good agreement with the experimental data.

Further, our experimental results indicated high excess pore pressures of 5.7 MPa and 5.0 MPa for the samples from 714 and 721 mbsf, respectively (Figure 2-7c). These values correspond to pore pressures supporting 95% and 89% of the overburden stress. The depth of the high excess pore pressures coincides with that of low Cl^- anomalies and the upper boundary of a depth interval with enhanced number of reverse faults and shear fractures (Figure 2-7b).

2.4.2 Coupled Pore Pressure Dissipation and Chemical Transport Model

Sensitivity analysis for our coupled pore pressure dissipation and chemical transport model shows that the maintenance of excess pore pressure is sensitive to the duration of transient lateral fluid flow (Figure S2-3). Lithostatic pore pressure dissipates quickly when using a duration of 10 years, but can be nearly maintained for several thousand years if a duration of 1000 years is employed. Along the major reverse faults, a duration of 10 years generates obviously lower pore pressure estimates compared to experimental data, while the duration of 1000 years yields obviously larger values. Only the modeled pore pressure from a duration of 100 years best fits the experimental data.

In contrast, the Cl^- concentration profile is controlled by both the duration of transient lateral fluid flow and the Cl^- concentration of influx fluids (Figure S2-3). A longer duration of transience generates more freshened fluid for the same Cl^- concentration, whereas a higher Cl^- concentration of influx fluids leads to less freshened water for the same duration of transience. For a duration of 10 years, the modeled Cl^- concentrations are overall larger than the measured values. On the contrary, a duration of 1000 years predicts obviously lower values than the observed Cl^- concentrations. The modeled Cl^- concentrations using a duration of 100 years are generally consistent with the measured values and reach best fit when a moderately freshened fluid with Cl^- concentration = 400 mM is used.

In addition, the modeling results show that the assigned multiple fault zones with different timing of activity match the observable amplitudes of the Cl^- concentration peaks (Figure 2-7e). Our model predicts both the experimental pore pressure estimates and the Cl^- concentration profile best when assuming (1) four separate fault zones which were active between 3 kyr and 0.5 kyr before

present, (2) lithostatic pore pressure is maintained for 100 years before we allow pore pressure to dissipate, and (3) a moderately freshened fluid with Cl^- concentration = 400 mM (Figure S2-3).

2.5 Discussion

2.5.1 Comparison with Previous Pore Pressure Estimates

Here, we provide new estimates for the excess pore pressure at the seaward edge of the Nankai Trough accretionary prism offshore Muroto peninsula based on a combination of uniaxial consolidation tests and numerical modeling. In contrast to many previous studies focusing on the underthrust sequence, we report on pore pressure in both the accreted and the underthrust sediments with regard to the consolidation state and stress path. The Cc and Cr values generated in our experiments are consistent with previous results of 0.32±0.15 and 0.03±0.02 for the sediments at the Muroto transect (Feeser et al., 1993; Bellew, 2004; Morgan & Ask, 2004), which might be a good hint for the quality of our experiments. Our experimental estimates of pore pressure are reliable considering the error bar is generally narrow.

Our experimental data reveal an overpressured underthrust sequence with excess pore pressures ranging from 3.4 MPa to 4.2 MPa (Figure 2-7c). The pore pressure results are consistent with previous estimates from uniaxial consolidation experiments using a triaxial cell (Morgan & Ask, 2004), corroborating our correction scheme for secondary consolidation and diagenesis. The laboratory-based estimates are also in good agreement with our own and other numerical modeling results that utilized Site 1173 as a normally consolidated reference site (e.g., Screaton et al., 2002; Skarbek & Saffer, 2009; Hüpers & Kopf, 2009; Tobin & Saffer, 2009). As discussed in section 3.1.2, the porosity profile at Site 1173 reflects the combined effects of primary, secondary consolidation and diagenesis. Hence, those effects are accounted for in the vertical hydrostatic effective stress–porosity relationship of the reference site, which produced results similar to those obtained by our correction scheme. This confirms previous assumptions by Screaton et al. (2002) that the vertical hydrostatic effective stress–porosity relationship observed at Site 1173 continues to depths equivalent to those at Sites 1174 and 808.

Our consolidation tests also reveal excess pore pressure in the accreted Upper Shikoku Basin facies to outer trench-wedge facies (Unit III to IIB). The estimated pore pressures are higher than previous estimates at Sites 808 and 1174 by Tsuji et al. (2008) based on seismic velocity. Their mean effective stress–porosity relationship derived from underthrust sediments does not consider the different stress state for the accreted sediments and causes the underprediction of excess pore pressure. Our experimentally determined pore pressure ratios meet the theoretical limits for in situ stress at Site 808 inferred from borehole breakout by Huffman and Saffer (2016). In comparison, our numerical approaches predict similar pore pressures only for the weak fault model, in which the strength of the prism sediment is governed by low friction along preexisting faults or the accretionary prism is not at Coulomb failure. The intact sediment model results in higher pore

pressure ratios (λ_p = 0.71-0.85) than in the underthrust sequence (Figure 2-7d). Using the same numerical approach with friction angles of 5–30°, Flemings and Saffer (2018) obtained similar values (λ_p = 0.7-0.9) for Sites 1174 and 808 and proposed the excess pore pressure was attributed to rapid loading by burial and horizontal compression. Although uncertainty may exist in some of above estimates, all these data are much higher than the fluid overpressures of <0.2 MPa monitored in a sealed borehole observatory at Site 808 (Sawyer et al., 2008). Flemings and Saffer (2018) raised the possibility that small leaks in the observatory bleed excess pressure more rapidly than fluids can be delivered from the surrounding clay-rich wallrock.

2.5.2 Pore Pressure Regime in Shallow Subduction Zones

In general our data is consistent with the view of rapid loading by burial and horizontal compression causing elevated pore pressure in the shallow low permeable clay-rich subduction zone sediments (e.g., Moore & Vrolijk, 1992; Saffer & Tobin, 2011). However, our results provide new insights into pore pressure regime and timing of fluid flow processes in the shallow subduction zone, although we made some assumptions and simplifications in our calculations and modeling (section 3).

The experimental results show a continuous pore pressure increase across the accreted and underthrust sequence with λ_p = 0.69-0.76, except for the two samples in the major reverse fault zone. This does not support previous views that the décollement acts as a fluid flow barrier and causes excess pore pressure in the underthrust sediments (e.g., Gamage & Screaton, 2006; Saffer & Tobin, 2011). Although previous studies have reported that fault-normal permeability can be several orders of magnitude lower than the wall-rock (e.g., Faulkner & Rutter, 1998), neither the permeability is low enough, nor is the major reverse fault zone sufficiently thick to seal the fluid pressure according to the theoretical fluid pressure barrier model (Deming, 1994). This is also corroborated by the measured permeability of sheared sediment samples at Site 1174 (Ikari & Saffer, 2012), which is 1~2 orders of magnitude higher than the estimated permeability required for a fluid barrier (Gamage & Screaton, 2006). Therefore, the porosity offset across the shallow décollement reflects different consolidation processes above and below the décollement, instead of a fluid barrier. Our experimental work therefore supports the view of Flemings and Saffer (2018) that the additional porosity loss in the accreted section results from a higher mean effective stress and shear-induced compaction caused by the tectonic loading.

Our experimental data do not support previous speculations by Flemings and Saffer (2018) that pore pressure in the accreted section is higher than in the underthrust sediment as predicted by the intact sediment model (Figure 2-7c). However, if near lithostatic pore fluids dissipate from the major reverse fault zones, the pore pressure can rise up in the wall rock and exceed our estimates based on consolidation experiments, as shown in our coupled pore pressure dissipation and chemical transport model (Figure 2-7c). Therefore, our experimental estimates represent the lower bound of in situ pore pressure. On the contrary, the intact sediment model may predict the upper

bound because it assumes constant friction angle and compressibility (λ). Recent studies have shown that the friction angle (Casey et al., 2016) and compressibility (Casey, 2014) decrease with increasing stress. These two overestimated values at high stress will lead to overestimation of pore pressure. The weak fault model shows a good agreement with experimental data, hinting that the stress state in the prism might be controlled by the presence of preexisting weak faults or that the accreted intact sediment is not at Coulomb failure (Huffman & Saffer, 2016; Flemings & Saffer, 2018). An outer prism not in Coulomb failure would also be consistent with the dynamic Coulomb wedge theory that predicts stress relaxation of the prism in the post-seismic interval in which the sediment is brought back to a stable elastic regime (Wang & Hu, 2006).

2.5.3 Near Lithostatic Pore Pressure along Décollement

For the top of the major reverse fault zone at 714 and 721 mbsf, near lithostatic pore pressure is revealed from the experimental tests, which we relate to fault activity as discussed in section 3.3. However, unloading by transient lithostatic pore pressure should not be reflected in the pore pressure estimates by consolidation tests. We speculate that the disturbance from deformation in the major reverse fault zone destroys the fabric of sediment and causes memory loss of past maximum effective stress. This speculation is supported by the optical microscopic observation from Maltman et al. (1993) that intense fabric reorientation is visible in the shear zone at Site 808. Furthermore, these authors also observed hydraulically fragmented breccia at 788 mbsf, which provides evidence that lithostatic pore pressure ever occurred in this horizon. If the hydraulic brecciation is present in the major reverse fault zone at Site C0023, the fabric of sediment might be further destroyed. With the most conservative estimation of excess pore pressures without any correction for secondary consolidation and diagenesis (i.e., using Equation (2-7) with OCR = 1), excess pore pressures of 4.2 and 5.4 MPa are still higher than that of surrounding sediments and correspond to 84% and 93% of the lithostatic stress, respectively (Figure 2-7c). The high excess pore pressures are also supported by the low Cl^- anomalies at corresponding depths, which are common signals for the transient and localized updip migration along a temporarily dilatant fault in response of lithostatic pore pressure (Bolton et al., 1998; Tobin et al., 2001). In addition, based on boundary conditions and assumptions described in section 3.3, our coupled pore pressure dissipation and chemical transport model predicted the observed Cl^- anomaly (Figure 2-7e) and the remaining present pore pressure was similarly high to experimental estimates (Figure 2-7c), which we also see as a prove for the reliability of the fault zone pore pressure estimates. Along the décollement, the density change during unloading is small (e.g., Nobes et al., 1991), but the high pore pressure may cause a decrease in the seismic velocity (e.g., Tobin et al., 1994) and lead to a reverse-polarity of seismic reflections (e.g., Moore et al., 1995). Therefore, our data support that the impedance-decreasing décollement found by Park et al. (2014) could be at least partially attributed to the increase of pore pressure within the fault zone. The reflection of décollement in

the seismic profile (Figure 2-1b) might represent a highly overpressured horizon, which also marks the migration path of freshened pore fluids.

Further, the coupled pore pressure dissipation and chemical transport model shows that the high excess pore pressures can be maintained when a duration of 100 years for the transient lateral fluid flow is employed (Figure S2-3). This duration, in which both the lithostatic pore pressure and low Cl^- concentration are maintained at the fault, is similar to the fault sealing rate (70 years) used by Gratier et al. (2003). Instead, it is considerable shorter than previous estimates for the Nankai margins of 80 kyrs (Saffer & Bekins, 1999). We explain the difference with the number and the ~100 m wide distribution of the fault strands as well as relatively small excursions assumed to be attributable to updip fluid migration (Saffer & McKiernan, 2009) in our model. This greatly reduces the diffusion time compared to previous models (Saffer & Bekins, 1998, 1999) which attribute all the geochemical anomalies to episodic fluid flow and consider a single thick fault strand. Also, our results of frequently active fault strands are in line with studies on biomarker thermal maturity indicators that identified seismic faults in drill cores recovered from the Japan Trench subduction zone (Rabinowitz et al., 2020). These results show that even fault zones that have hosted earthquakes with displacement ≥ 10 m ruptured repeatedly during a period of 36 kyrs.

The view of transient fluid flow along the subduction thrust is not at odds with the proposed continuous pore pressure increase across the accreted and underthrust sequence, because excess pore pressure along the faults will eventually reduce to the background pore pressure in times of inactivity. Due to the temporal proximity of the last fault activity, the lithostatic pore pressure may not have fully dissipated to the background values. Such an overpressure is not captured by previous laboratory data and any numerical methods applied in this study or previous ones, because they do not account for porosity change by unloading through transient pore pressure increase. Based on the best fit of our coupled pore pressure dissipation and chemical transport model, excess pore pressure could be high in the depth interval between 600 and 780 mbsf.

Setting a constant pore pressure gradient (equivalent to λ_p = 0.71) and the general decreasing trend of chlorinity (Figure 2-2c) as initial conditions, the best fit of the Cl^- profile in our coupled pore pressure dissipation and chemical transport model only requires a moderate fluid freshening. This led us speculate on the fluid source depth. While low Cl^- values are commonly associated with deep fluids, typical geochemical signatures for a deep-seated origin, such as elevated B, Li or CH_4 concentrations (e.g., Kastner et al., 1991; You et al., 1996), are missing in the respective horizons at site C0023 (Heuer et al., 2017). We therefore relate the fluid origin to an overpressured zone along the décollement downdip at a depth of advanced clay dehydration but below peak formation temperature of thermogenic hydrocarbons (100–150°C). These assumption contrasts the previous view of episodic fluid flow along the entire fault surface after earthquake rupture but supports the emerging picture of a heterogeneous plate boundary with overpressured and permeable patches along the fault surface that shift in time and space (Saffer, 2015). A possible

trigger for the spatially limited fluid flow could be the propagation of the frontal thrust which is rooted to the subduction thrust close to Site C0023 (Figure 2-1b).

2.5.4 Mechanical Strength of Décollement and Its Implication

Because pore fluid pressure is a critical parameter that determines the mechanical strength and slip behavior of faults (Saffer & Tobin, 2011), we computed the shear strength using the effective stress at 714 and 721 mbsf and a friction coefficient of 0.27 for Muroto décollement reported by Ikari and Kopf (2017). The resulting shear strength is as low as 0.4 to 0.8 MPa, lower than the 2~3 MPa previously estimated by Tobin and Saffer (2009) and also lower than the ~2 MPa suggested by Kopf and Brown (2003) as well as Skarbek and Saffer (2009). Instead, it is similar to the inferred coseismic shear strength (0.54 MPa and 0.22-1.32 MPa) in the 2011 Tohoku earthquake from temperature anomaly after the event by Fulton et al. (2013) and from high-velocity friction experiments without excess pore pressure by Ujiie et al. (2013), respectively. Although we do not have pore pressure estimates for the décollement, the excess pore pressure there should be equally high because lithostatic pore pressure transients migrated along that horizon (Figure 2-7c). Faulkner et al. (2011) proposed that propagation through material with very low shear strength is energetically favorable as it provides little resistance and may explain how a large rupture is not arrested from propagating to the trench as in the Tohoku earthquake. Moreover, overpressured shallow décollement zones with low effective stress are conditionally stable and can be easily destabilized by a sudden dynamic slip (Park et al., 2014). Laboratory data by Saffer and Marone (2003) further show that under low effective stress conditions the tendency for velocity strengthening behavior diminishes. Therefore, if the reverse-polarity of seismic reflections along the décollement horizon offshore Shikoku Island (Park et al., 2014) represents similarly high pore pressure as revealed at Site C0023, seismic slip could be propagated to the trench and cause tsunami hazard offshore SW Japan when a large earthquake occurs.

2.6 Conclusions

We characterized the pore pressure regime and fluid flow processes in the shallow Nankai Trough subduction zone based on robust pore pressure estimates from consolidation experiments and numerical models. From our results, excess pore pressures increase continuously across the accreted and underthrust sediments, with nearly constant pore pressure ratios. We suggest that both accreted and underthrust sediments constitute one hydrogeological system and the décollement is not a fluid barrier as previously believed. Near lithostatic pore pressure along the subduction thrust seems to be attributable to the propagation of the frontal thrust which causes repeated lithostatic pore pressure transients migrated along faults in the last 3 kyrs. The resulting extremely low shear strength is similar to the inferred coseismic shear strength in the 2011 Tohoku earthquake, which triggered massive near-trench displacement and a catastrophic tsunami.

Supplementary Material

The supplementary material contains 1 text, 3 figures and 3 tables to support the main article. Text S2-1 describes the construction procedures for estimating the preconsolidation pressure by modified Casagrande method (McNulty et al., 1978). Figures S2-1 and S2-2 show the results of estimated preconsolidation pressure based on modified Casagrande method (McNulty et al., 1978) and Pacheco Silva method (1970), respectively. Figure S2-3 shows the modeled profiles of the excess pore pressure and Cl- concentration by the coupled pore pressure dissipation and chemical transport model. Table S2-1 lists the details of the whole round samples used in this study. Table S2-2 lists the experimental results of the tested samples. Table S2-3 lists the collected consolidation data in the Nankai Trough from 400 to 1100 mbsf.

Text S2-1. Construction procedures for estimating the preconsolidation pressure by modified Casagrande empirical graphical approach after McNulty et al. (1978).

a). Determine the recompression line by regressing the first several data points.

b). Determine the virgin compression line by regressing the last several data points.

c). Determine the transition curve between recompression line and virgin compression line by regressing the data points in between.

d). Draw the bisector of the angle between recompression line and virgin compression line, and determine the intersection of the bisector and transition curve. The intersection is the point with maximum curvature (McNulty et al., 1978).

e). Draw a horizontal line through the maximum curvature point.

f). Draw the tangent to the transition curve at maximum curvature point and bisect the angle between the tangent and the horizontal.

g). The effective pressure at the intersection point of the bisector and virgin compression line gives the approximate value of the preconsolidation pressure.

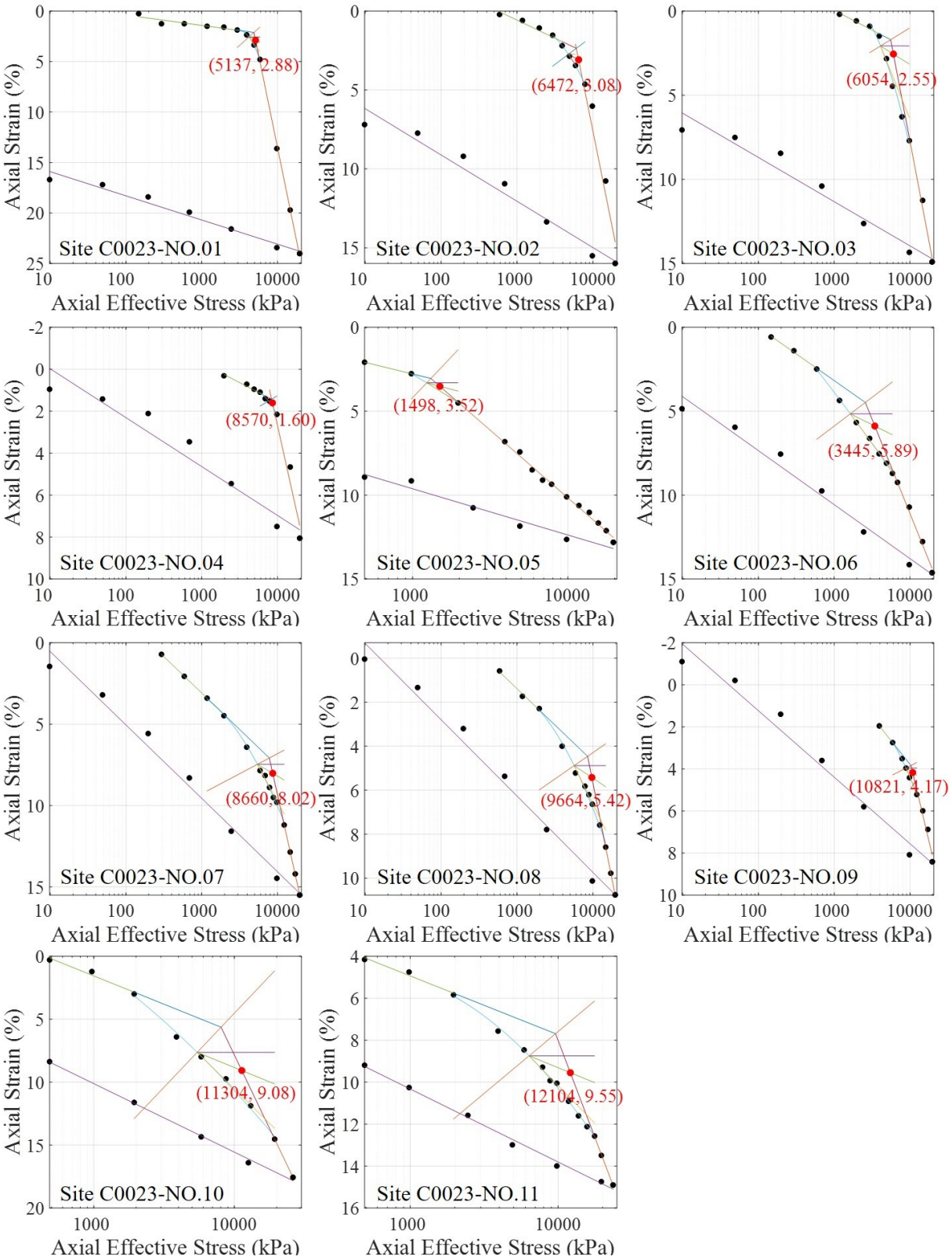

Figure S2-1. Estimations of the preconsolidation stress based on modified Casagrande empirical graphical approach after McNulty et al. (1978).

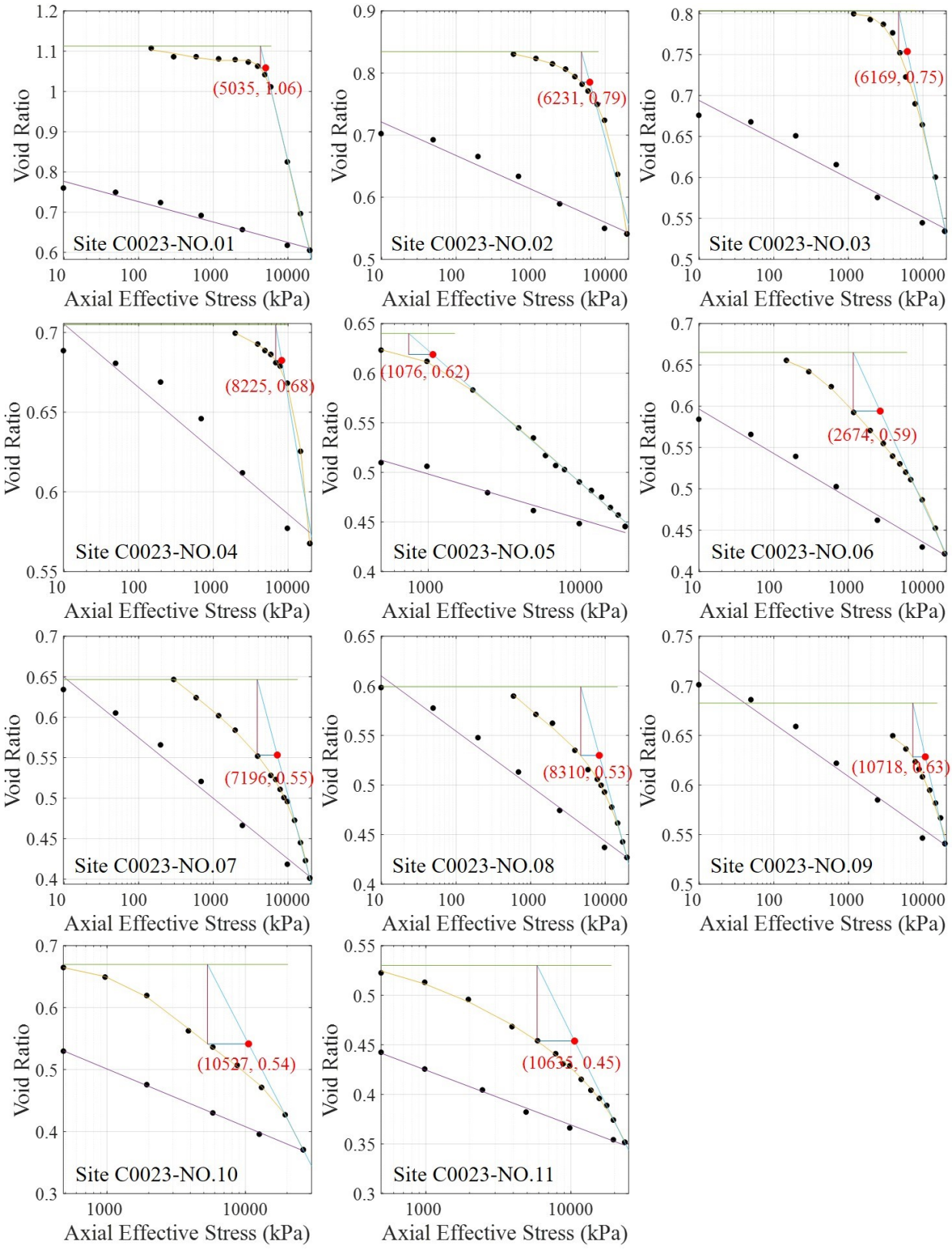

Figure S2-2. Estimations of the preconsolidation stress based on Pacheco Silva method (1970).

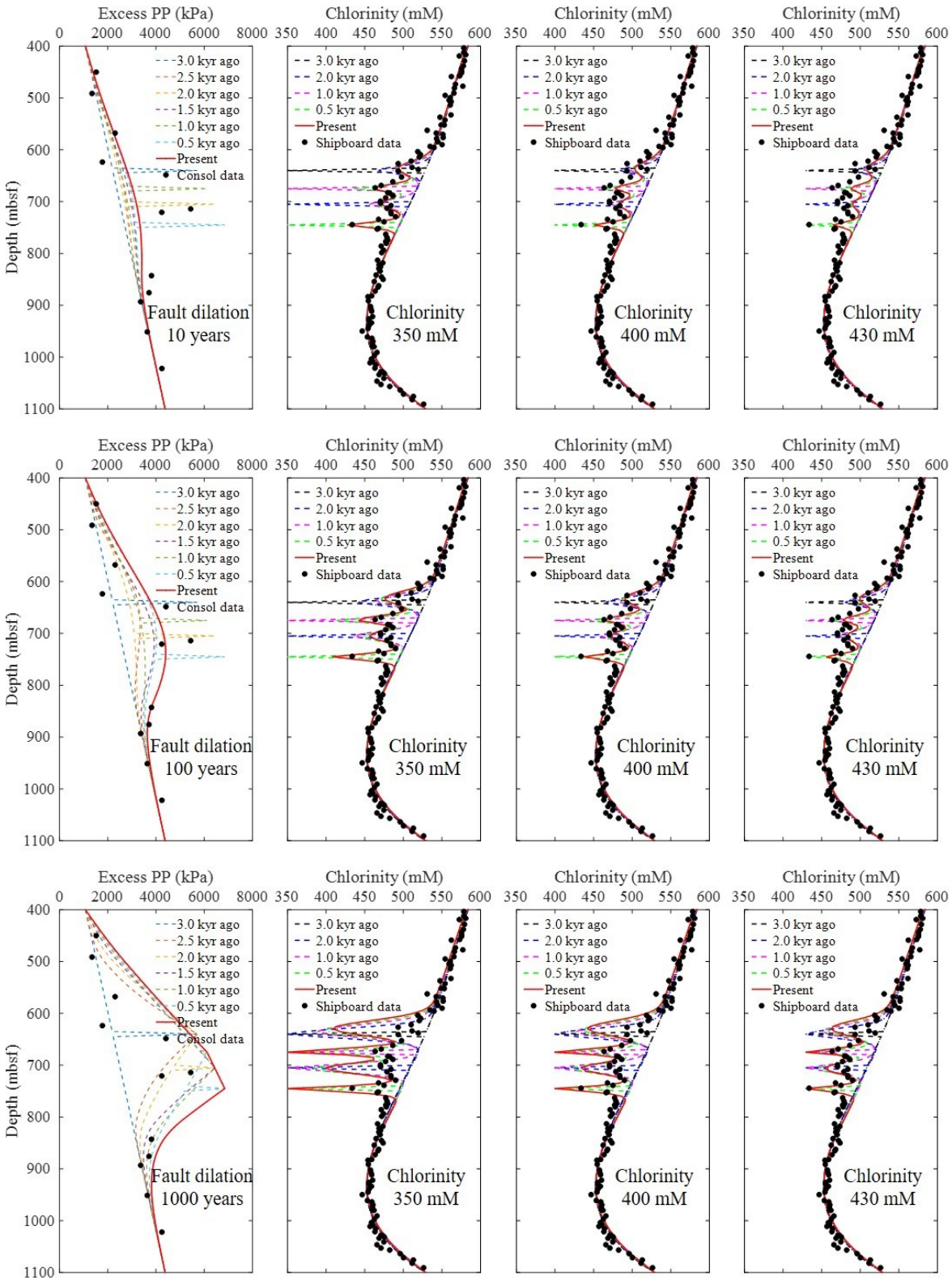

Figure S2-3. The modeled profiles of the excess pore pressure and Cl- concentration using different durations of fault dilation and Cl- concentrations of the influx fluid. PP=pore pressure.

Table S2-1. Details of the whole round samples in this study.

Sample NO.	J-CORES sample ID	Leg/Exp.	Sample source	Sample code	Bottom Depth [m CSF-A, DSF, MSF, WSF]
NO.01	CKY000000000006889400	370	C0023A-20R-3 WR, 10.0--30.0 cm	370AHWR	449.885
NO.02	CKY000000000006931400	370	C0023A-24R-7 WR, 62.0--80.0 cm	370AHWR	492.26
NO.03	CKY000000000007013900	370	C0023A-33R-8 WR, 15.0--35.0 cm	370AHWR	568.97
NO.04	CKY000000000007088600	370	C0023A-40R-3 WR, 120.0--141.0 cm	370AHWR	625.03
NO.05	CKY000000000007315200	370	C0023A-54R-2 WR, 0.0--20.0 cm	370AHWR	713.795
NO.06	CKY000000000007343100	370	C0023A-55R-3 WR, 97.0--112.0 cm	370AHWR	721.32
NO.07	CKY000000000007562700	370	C0023A-80R-7 WR, 130.0--151.0 cm	370AHWR	842.45
NO.08	CKY000000000007738200	370	C0023A-84R-4 WR, 10.0--30.0 cm	370AHWR	875.355
NO.09	CKY000000000007753600	370	C0023A-86R-3 WR, 92.0--115.0 cm	370AHWR	892.83
NO.10	CKY000000000007821000	370	C0023A-92R-3 WR, 115.0--136.5 cm	370AHWR	950.775
NO.11	CKY000000000007915900	370	C0023A-99R-3 WR, 0.0--20.0 cm	370AHWR	1023.195

Table S2-2. Experimental results of the tested samples.

Sample NO.	Depth (mbsf)	σ_v (kPa)	P_{hy} (kPa)	σ'_{vh} (kPa)	σ'_{pc} (kPa)				Cr	Cc	Ce
					Casagrande	Pacheco Silva	Maximum	Minimum			
NO.01	450	8225	4520	3704	5137	5035	5808	4714	0.01	0.34	0.02
NO.02	491	9044	4945	4098	6472	6231	7744	6263	0.01	0.26	0.02
NO.03	568	10586	5706	4880	6054	6169	7744	5314	0.02	0.19	0.02
NO.04	624	11683	6261	5422	8570	8225	9680	7986	0.01	0.14	0.02
NO.05	714	13595	7177	6419	1498	1076	1936	1100	0.02	0.06	0.02
NO.06	721	13738	7244	6494	3445	2674	4840	3374	0.02	0.09	0.02
NO.07	843	16324	8466	7859	8660	7196	9680	7159	0.03	0.15	0.03
NO.08	876	17020	8794	8226	9664	8310	9680	8279	0.02	0.12	0.02
NO.09	893	17387	8965	8421	10821	10718	12100	8586	0.03	0.11	0.02
NO.10	951	18636	9552	9084	11304	10527	13068	10551	0.03	0.17	0.04
NO.11	1022	20161	10262	9899	12104	10635	15488	10394	0.02	0.13	0.02

Table S2-3. Collected consolidation data in the Nankai Trough from 400 to 1100 mbsf.

Site	Depth (mbsf)	σ_v (MPa)	P_{hy} (MPa)	σ'_{vh} (MPa)	σ'_v (MPa)	σ'_{pc} (MPa)	OCR	OCD (MPa)	Data sources
1173	391.27	6.39	3.93	2.46	2.46	3.17	1.29	0.71	Bellew, 2004
1173	443.74	7.38	4.46	2.92	2.92	5.69	1.95	2.77	Bellew, 2004
1173	529.64	9.06	5.32	3.74	3.74	6.21	1.66	2.47	Bellew, 2004
1173	476	8.08	4.78	3.30	3.20	4.00	1.25	0.80	Morgan and Ask, 2004
1174	881	17.45	8.85	8.60	5.20	13.80	2.65	8.60	Morgan and Ask, 2004
808	1004	19.99	10.09	9.90	6.40	13.00	2.03	6.60	Morgan and Ask, 2004
808	1098	21.83	11.03	10.80	7.70	13.50	1.75	5.80	Morgan and Ask, 2004
C0011	433.6	7.18	4.36	2.82	2.82	5.05	1.79	2.23	Guo and Underwood, 2014
C0011	473.75	7.90	4.76	3.14	3.14	5.75	1.83	2.61	Guo and Underwood, 2014
C0011	495.61	8.33	4.98	3.35	3.35	5.75	1.72	2.40	Guo and Underwood, 2014
C0011	554.74	9.46	5.57	3.89	3.89	6.73	1.73	2.84	Guo and Underwood, 2014
C0011	580.72	9.95	5.83	4.12	4.12	9.52	2.31	5.40	Guo and Underwood, 2014
C0011	637.77	11.07	6.41	4.66	4.66	6.08	1.30	1.42	Guo and Underwood, 2014
C0011	669.2	11.67	6.72	4.95	4.95	7.76	1.57	2.81	Guo and Underwood, 2014
C0011	712.71	12.52	7.16	5.36	5.36	11.37	2.12	6.01	Guo and Underwood, 2014
C0011	748.62	13.25	7.52	5.73	5.73	8.72	1.52	2.99	Guo and Underwood, 2014
C0011	405.63	6.65	4.07	2.58	2.58	3.35	1.30	0.77	Hüpers and Kopf, 2012
C0011	406.49	6.67	4.08	2.59	2.59	2.21	0.85	-0.38	Hüpers and Kopf, 2012
C0011	629.57	10.90	6.32	4.58	4.58	5.62	1.23	1.04	Hüpers and Kopf, 2012
C0011	749.38	13.26	7.53	5.73	5.73	11.78	2.06	6.05	Hüpers and Kopf, 2012
C0011	780.41	13.88	7.84	6.04	6.04	11.16	1.85	5.12	Hüpers and Kopf, 2012
C0011	782.27	13.92	7.86	6.06	6.06	11.56	1.91	5.50	Hüpers and Kopf, 2012
C0011	493	8.27	4.95	3.32	3.32	5.64	1.70	2.32	Kitajima and Saffer, 2014
C0011	663	11.55	6.66	4.89	4.89	12.25	2.50	7.36	Kitajima and Saffer, 2014
C0011	763	13.53	7.66	5.87	5.87	11.25	1.92	5.38	Kitajima and Saffer, 2014
C0011	781	13.90	7.85	6.05	6.05	6.76	1.12	0.71	Kitajima and Saffer, 2014
C0011	862	15.53	8.66	6.87	6.87	17.31	2.52	10.44	Kitajima and Saffer, 2014

Chapter 3: The Effect of Consolidation State on Pore Pressure Prediction in an Accretionary Prism Using a Porosity-Based Critical State Soil Mechanics Approach

Junli Zhang[1], Andre Hüpers[1], Stefan Kreiter[1], Takeshi Tsuji[2], and Achim J. Kopf[1]

[1]MARUM—Center for Marine Environmental Sciences and Faculty of Geosciences, University of Bremen, Bremen, Germany
[2]Department of Earth Resources Engineering, Kyushu University, Fukuoka, Japan

Corresponding author: Junli Zhang (jzhang@marum.de)

Abstract

Pore fluid pressure is a key parameter to understand subduction zone processes because it governs the hydro-mechanical properties of the sediment material. However, direct pore pressure observations in accreted sediments are rare. Flemings and Saffer (2018, https://doi.org/10.1002/2017JB015025) recently proposed a porosity-based approach to predict pore pressure based on critical state soil mechanics. In our study, we advanced their work by introducing the consolidation state of sediments into the model and applied the new model to the Nankai accretionary prism off Muroto Peninsula. Our results reveal that the overconsolidated sediment in the Nankai Trough generates 40%~50% less excess pore pressure than the normally consolidated sediment, suggesting that overconsolidation inhibits the development of excess pore pressure. Based on the pore pressure estimates, we quantify the shear stress and shear strength along the décollement in the Nankai Trough. The shear strength is below 2.2 MPa, obviously larger than the shear stress (<0.4 MPa) along the décollement. This implies that the accretionary prism is not at Coulomb failure, which is in good agreement with the dynamic Coulomb model that the sediment in the outer wedge is brought back to a stable elastic regime in the postseismic interval.

3.1 Introduction

Pore fluid pressure is intimately associated with fluid flow and structural development of sediments and rocks in subduction zones (Saffer & Tobin, 2011). Previous studies have shown that pore pressure not only determines the absolute strength of faults (e.g., Tobin & Saffer, 2009), but also exerts a critical control on the overall geometry of the subduction complex (e.g., Davis et al., 1983; Wang & Hu, 2006), the fault slip behavior (e.g., Kitajima & Saffer, 2012; Liu & Rice, 2007) and the distribution of seismogenic zones (e.g., Moore & Saffer, 2001). To date, elevated pore pressure has been invoked to explain the small critical taper of accretionary wedge (e.g., Dahlen, 1990), the fault reactivation (e.g., Behrmann, 1991; Sibson et al., 1988), the occurrence of tsunamigenic slip near the trench (e.g., Seno, 2002), the wide seismogenic zone (e.g., Fagereng & Ellis, 2009), as well as a series of new modes of slip including slow slip events (e.g., Song et al., 2009), low frequency earthquakes and very low-frequency earthquakes (e.g., Ito & Obara, 2006).

Therefore, pore pressure is a key parameter to understand the hydro-mechanical processes in subduction zones.

Porosity-based prediction methods have been widely used to quantify the pore pressure in underthrust sediments of subduction zones, because porosity can be derived from pre-drilling seismic velocity (e.g., Tobin & Saffer, 2009), logging while drilling (LWD) data (e.g., Hoffman & Tobin, 2004) or moisture and density (MAD) measurements (e.g., Screaton et al., 2002). The applied approach typically involves a comparison between observed porosity and that of a normal consolidation curve (e.g., Saffer, 2003; Skarbek & Saffer, 2009). The latter is based on one-dimensional consolidation theory and depends on a relationship between porosity and vertical effective stress. One major limitation of this approach is the assumption that consolidation is only governed by vertical effective stress, which is not the case in an accretionary prism where the stress environment is complex. Time-variant mean effective stresses and shear stresses control the consolidation of sediments in accretionary prisms (e.g., Kitajima et al., 2017), thus porosity-based pore pressure predictions with realistic stress environments are rare for accreting sediments.

Building on critical state soil mechanics, Flemings and Saffer (2018) recently proposed a new porosity-based approach to predict the pore pressure in subduction zones, which also allows the pore pressure prediction in the accretionary prism. This method assumes the accretionary prism is in a state of Coulomb failure and the deformation behavior follows the Modified Cam Clay (MCC) critical state model (Roscoe & Burland, 1968). By neglecting the elastic deformation, the pore pressure and stress magnitudes at any stress state can be predicted. Although this method provides a complete pathway to predict the pore pressure in both accretionary prism and underthrust sediments by relating porosity change to variation of mean effective stress and shear stress, the consolidation state of sediments, which has important impact on the model performance (e.g., Swarbrick, 2001), is not considered. In this paper, we (1) advance upon their work by introducing the consolidation state of sediments into the model, and (2) explore the effect of overconsolidation on pore pressure estimates by applying the newly modified method to the Nankai Trough accretionary prism.

3.2 Geological Setting

The Nankai Trough subduction zone forearc off the southwest coast of Japan (Figure 1) is formed by the subduction of the Philippine Sea plate to the northwest beneath the Eurasian plate with a present-day convergence rate of 4-6 cm/yr (Seno et al., 1993; Miyazaki & Heki, 2001). Ocean drilling expeditions have been undertaken in the Nankai Trough along three regional transects: Ashizuri, Muroto and Kumano, all named after the respective peninsulas. In this study, we focus on the Muroto transect, where a very low wedge taper angle indicates low shear strength and elevated pore pressure along the subduction thrust (Brown et al., 2003). The Muroto transect has been investigated by Ocean Drilling Program (ODP) and International Ocean Discovery Program (IODP) expeditions. ODP Leg 131 penetrated and cored the accretionary prism and underthrust

section at Site 808, located 3 km landward of the trench (Taira et al., 1991). In subsequent ODP Leg 190, Sites 1173 and 1174 as well as several other sites were drilled (Moore et al., 2001). Site 1173 is a reference site and was drilled 11 km outboard of the trench, whereas Site 1174 is a less-deformed analog to Site 808 and was drilled to 1120 meters below seafloor (mbsf) at 2 km landward of the trench (Moore et al., 2001). Recently IODP Expedition 370 established Site C0023, close to Sites 808 and 1174, to investigate the limits of life in the deep subseafloor biosphere and drilled the borehole to 1177 mbsf (Heuer et al., 2017).

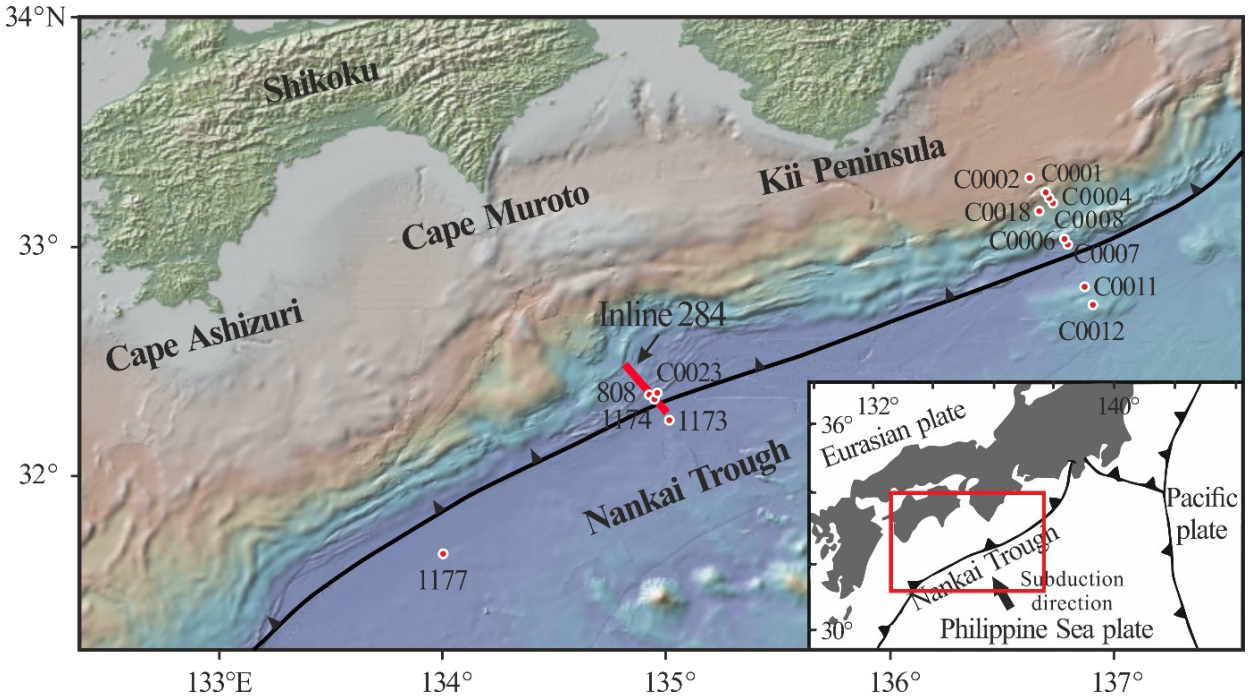

Figure 3-1. Bathymetry map of the Nankai Trough and locations of the seismic profile and ODP/IODP drill sites used in this study. Figure made with GeoMapApp (www.geomapapp.org; Ryan et al., 2009). Thick red line shows the location of the seismic Inline 284. Solid dots mark drill sites. Inset: The tectonic background of the Nankai Trough after Moore et al. (2001). IODP, International Ocean Discovery Program; ODP, Ocean Drilling Program.

The strata in the Nankai Trough subduction zone off Cape Muroto includes five lithostratigraphic units (e.g., Moore et al., 2001). Above the basaltic basement, a ~15-50 m thick middle Miocene volcaniclastic facies is recognized and is composed of volcaniclastic tuff and variegated mudstones (Taira et al., 1991; Heuer et al., 2017). Overlying the volcaniclastic facies, a middle Miocene - Pliocene lower Shikoku Basin (LSB) facies, mainly comprising heavily bioturbated hemipelagic mudstones with traces of disseminated ashes, is developed, with thickness ranging from ~420 to ~470 m (Taira et al., 1991; Heuer et al., 2017). The facies change from LSB to upper Shikoku Basin (USB) is defined by the appearance of recognizable volcanic tuff layers (Moore et al., 2001; Heuer et al., 2017). The Pliocene to Quaternary USB facies is ~140-210 m thick and consists of hemipelagic mudstones with interbeds of tuffs and tuffaceous sedimentary rocks (Heuer et al.,

2017). With the plate moving towards the trench, a ~480-540 m thick trench-wedge (TW) facies containing turbidite and bioturbated mudstones, siltstones, sandstones, and volcanic tuffs deposits on USB facies (Taira et al., 1991; Moore et al., 2001; Heuer et al., 2017). At the top of the trench-wedge sediment, a ~5-20 m thick slope-apron facies lies and includes mud, clayey silt and fine-grained sand (Taira et al., 1991; Moore et al., 2001).

The porosity at Sites 808, 1174 and C0023 generally decreases with depth and a consistent porosity increase across the décollement is present (Figure 2). Higher mean effective stress and shear-induced compaction driven by the tectonic loading lead to an additional porosity loss in the accretionary prism compared to reference Site 1173 (Figure 2, Flemings & Saffer, 2018). The relatively high porosity beneath the décollement has been interpreted as inhibited fluid expulsion and excess pore pressure (Gamage & Screaton, 2006). Also, pore water freshening is widely observed along the décollement and suggests up-dip migration of freshened fluids to the trench (Brown et al., 2001; Saffer & McKiernan, 2009), which is in good agreement with the nearly lithostatic pore pressure along the décollement (Zhang et al., 2021).

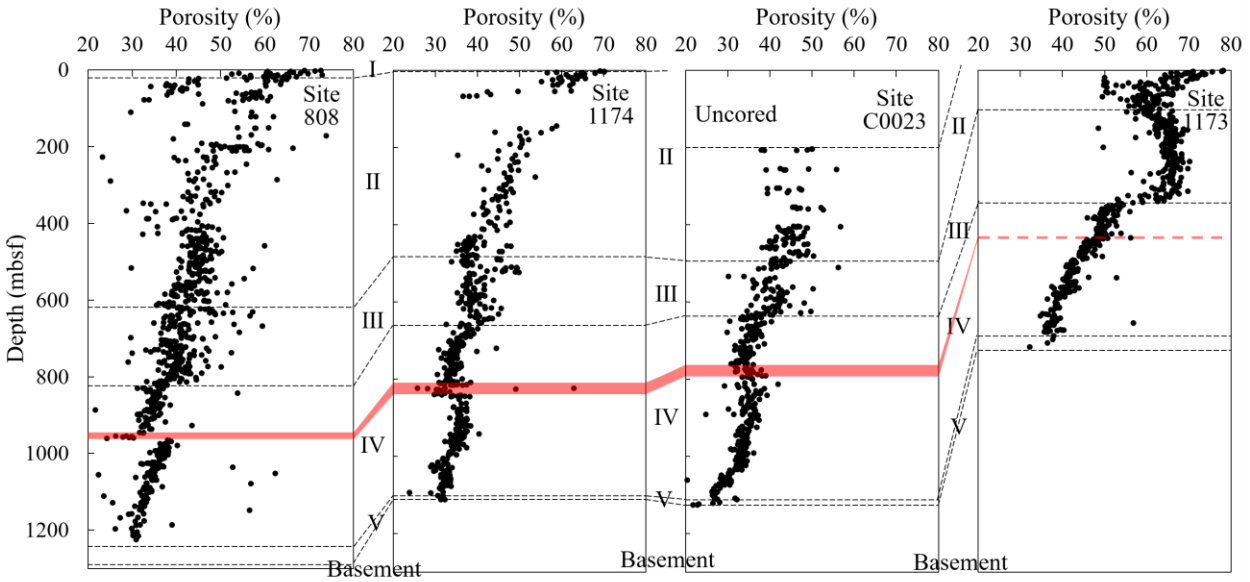

Figure 3-2. Porosity profiles at Sites 808, 1174, C0023 and 1173. The porosity data are collected from Taira et al. (1991), Moore et al. (2001), Heuer et al. (2017) and Zhang et al. (2021). I = slope-apron facies, II = trench-wedge facies, III = upper Shikoku Basin facies, IV= lower Shikoku Basin facies, and V = volcaniclastic facies. Red shading marks the location of the décollement. The stratigraphically equivalent depth of décollement at Site 1173 is marked by a red dashed line.

3.3 Concepts and Models

3.3.1 Stress and Pressure

The lithostatic stress (vertical total stress or overburden stress) is the stress caused by the weights of solid particles and pore fluids and can be calculated by the integral of the bulk formation density as follows:

$$\sigma_v(z_0) = g \cdot \int_0^{z_0} \rho(z) \cdot dz \tag{3-1}$$

where σ_v is lithostatic stress, g gravity acceleration, ρ the depth-variant bulk formation density, and z depth. According to the principle of effective stress (Terzaghi, 1943), the lithostatic stress is carried by the solid particle skeleton and pore fluids, as expressed by:

$$\sigma_v = \sigma_v^{'} + P \tag{3-2}$$

where $\sigma_v^{'}$ is the in situ vertical effective stress and P is the pore pressure.

The stress state of a sediment element can be represented by three perpendicular principal effective stresses, $\sigma_1^{'}$, $\sigma_2^{'}$ and $\sigma_3^{'}$, which are the normal stresses on three perpendicular planes (e.g., Davis & Selvadurai, 1996; Kitajima et al., 2012; Lin et al., 2016). $\sigma_1^{'}$ is the maximum principal effective stress, $\sigma_2^{'}$ is the intermediate principal effective stress, and $\sigma_3^{'}$ is the minimum principal effective stress. In subduction zones, $\sigma_1^{'}$ and $\sigma_3^{'}$ are normally considered to be vertical and horizontal respectively in underthrust complex, whereas that in accretionary prism are assumed to be horizontal and vertical (e.g., Moore & Tobin, 1997; Tsuji et al., 2008).

3.3.2 Consolidation

Consolidation is the gradual volume reduction of fully saturated sediments with increasing effective stress (Terzaghi, 1943; Knappett & Craig, 2012). If the sediment is consolidated under uniaxial compression with zero lateral strain, the process is called K_0 consolidation, where K_0 is the ratio of horizontal to vertical effective stress (e.g., Knappett & Craig, 2012). The maximum vertical effective stress that the sediment has sustained in its consolidation history is termed preconsolidation stress $\sigma_{pc}^{'}$ (Casagrande, 1936). The quantitative relation between $\sigma_v^{'}$ and $\sigma_{pc}^{'}$ is given by overconsolidation ratio (OCR):

$$OCR = \frac{\sigma_{pc}^{'}}{\sigma_v^{'}} \tag{3-3}$$

The sediment is said to be normally consolidated when *OCR* = 1, whereas it is called overconsolidated when *OCR* > 1. However because $\sigma_v^{'}$ can never be less than $\sigma_{pc}^{'}$, *OCR* < 1 does not exist in strict sense (e.g., Knappett & Craig, 2012). But it is also common to replace $\sigma_v^{'}$ by hydrostatic vertical effective stress $\sigma_{vh}^{'}$ in equation (3-3) to calculate *OCR* owing to difficulty in obtaining $\sigma_v^{'}$, which leads to OCR<1 (e.g., Saffer, 2003; Kitajima & Saffer, 2014). In this study, we refer to the value derived from $\sigma_{vh}^{'}$ as *OCR*'. In practice, $\sigma_{pc}^{'}$ is commonly determined by the yield point in consolidation tests which marks the deformation transition from recompression to virgin compression (e.g., Knappett & Craig, 2012). Many previous studies have shown that although some sediments have never experienced unloading, consolidation tests yield higher $\sigma_{pc}^{'}$ than $\sigma_v^{'}$ (e.g.,Bjerrum, 1973; Graham et al., 1983; Leonards & Ramiah, 1960). This can be attributed to secondary consolidation and diagenesis which cause a strengthening of the sediments and shift the yield point to higher stress (e.g., Bjerrum, 1973; Locat & Lefebvre, 1986). Generally, these sediments are treated as overconsolidated sediments because they demonstrate similar material characteristics to those which have experienced unloading (e.g., Morgan & Ask, 2004).

The Nankai Trough is one of the world's best studied convergent margins and numerous consolidation tests were conducted to infer the consolidation state of the sediments on the incoming Philippine Sea plate. In contrast to Zhang et al. (2021), we compiled all possible consolidation data in the Nankai Trough (Karig, 1993; Morgan & Ask, 2004; Bellew, 2004; Hüpers & Kopf, 2012; Guo & Underwood, 2014; Daigle & Dugan, 2014; Kitajima & Saffer, 2014; Zhang et al., 2021) to calculate the *OCR* values (Figure 3). The data are from drill sites seaward and landward of the deformation front along the Muroto, Kumano and Ashizuri transects (Figure 1). The $\sigma_v^{'}$ values at seaward reference Sites 1173, 1177, C0011 and C0012 were inferred from $\sigma_{vh}^{'}$ where low sedimentation rates prevented pore pressure in excess of hydrostatic (e.g., Screaton et al., 2002; Kitajima & Saffer, 2014), while the $\sigma_v^{'}$ values from underthrust sediments at Sites 808, 1174 and C0023 were derived from porosity-based pore pressure predictions (e.g., Screaton et al., 2002; Morgan & Ask, 2004). The *OCR* values from the accretionary prism were unavailable due to the difficulty in obtaining $\sigma_v^{'}$, we therefore used *OCR*' to show the consolidation state of accreting sediments (Dugan & Daigle, 2011; Saffer et al., 2011; Guo et al., 2011; Zhang et al., 2021). For $\sigma_{pc}^{'}$ values, all the data from Site C0012 were corrected for the erosional unloading / removed overburden of 0.45 MPa at 15 mbsf and 1.04 MPa at 85 mbsf, respectively (Kitajima & Saffer, 2014). Despite the scatter, *OCR* values give evidence for overconsolidated sediment in the Nankai Trough (Figure 3). The *OCR* values less than 1 above 500 mbsf might be attributed to small excess pore pressures which lead to an overestimation of $\sigma_v^{'}$. Excluding these data, the *OCR* values in the Nankai Trough generally range from 1.30 to 2.50. For the prism sediments, the *OCR*' values are extremely scattered at shallow depth, but remain relatively stable below ~100 mbsf

(Figure 3). This might be explained by the fact that the sediment at shallow depth has lower effective stress and its consolidation state is easily affected by the other processes like earthquake loading. Although the *OCR*' values of the accreting sediments are in a similar range with the *OCR* values from the underthrust sediments and reference sites, the *OCR* values of the accreting sediments should be larger, because (1) excess pore pressure in the accretionary prism decreases $\sigma_v^{'}$ (e.g., Zhang et al., 2021) and (2) horizontal tectonic loading increases $\sigma_{pc}^{'}$ (e.g., Saffer, 2003).

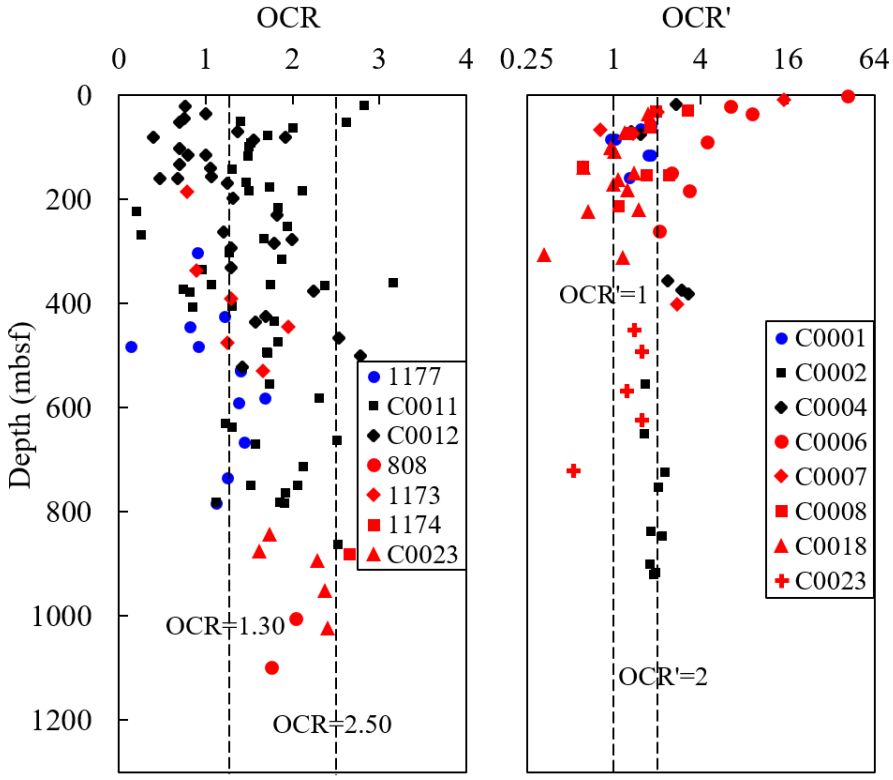

Figure 3-3. Profile of *OCR* and *OCR*' values in the Nankai Trough. The *OCR* vaules are from reference sites and underthrust sediments. The *OCR*' vaules are from accreted sediments. Data are collected from Karig (1993), Morgan and Ask (2004), Bellew (2004), Dugan and Daigle (2011), Saffer et al. (2011), Guo et al. (2011), Hüpers and Kopf (2012), Guo and Underwood (2014), Daigle and Dugan (2014), Kitajima and Saffer (2014) and Zhang et al. (2021).

3.3.3 Models

Flemings and Saffer (2018) proposed a porosity-based approach to predict the pore pressure in subduction zones, which assumes (1) the underthrust section is in a state of K_0 consolidation, (2) the accretionary prism is in a state of Coulomb failure, (3) $\sigma_1^{'}=\sigma_h^{'}$ and $\sigma_3^{'}=\sigma_v^{'}$ in the accretionary prism, where $\sigma_h^{'}$ represents the horizontal effective stress in the subduction direction, (4) the deformation behavior of the sediment follows the elasto-plastic Modified Cam Clay (MCC) model

under plane strain condition (Roscoe & Burland, 1968), and (5) the elastic deformation is negligible compared to plastic deformation. They showed the stress path of the sediment in the Nankai Trough based on a normal consolidation state. However the sediment in the Nankai Trough is overconsolidated, we therefore took the consolidation state of the sediment into consideration and expanded the method to overconsolidated sediments. For ease of description, we refer to their original model as normally consolidated (NC) model and our modified model as overconsolidated (OC) model. In the following section, we briefly describe the MCC model under plane strain condition (Roscoe & Burland, 1968), the stress path of sediments as they enter the accretionary prism (e.g., Karig, 1990; Kitajima & Saffer, 2014) and the approach proposed by Flemings and Saffer (2018) to predicted pore pressure, before we introduce our OC model.

The MCC model (Roscoe & Burland, 1968) is an elasto-plastic constitutive model in critical state soil mechanics, which links consolidation, shear strength and elastic and plastic deformations (Azizi, 2000). Under plane strain condition, the stress state of the sediment in subduction zones can be described by the mean principal effective stress s' and the maximum shear stress t in the plane of shearing:

$$s' = \frac{\sigma'_v + \sigma'_h}{2} \tag{3-4a}$$

$$t = \frac{\sigma'_v - \sigma'_h}{2} \tag{3-4b}$$

It should be noted that s' is different from the mean effective stress in the Cambridge triaxial compression theory, where the mean effective stress $p = (\sigma_1' + \sigma_2' + \sigma_3')/3$, while t always has the same value as the deviator stress $q = (\sigma_1' - \sigma_3')/2$, but might be negative. In the s'-t space (Figure 4), the slope (η_K) of an arbitrary line can be calculated by:

$$\eta_K = \frac{1-K}{1+K} \tag{3-5}$$

where K is the arbitrary effective stress ratio of σ'_h to σ'_v. The stress ratios under K_0 consolidation condition, at Coulomb failure (K_τ) and critical state (K_{cs}) are all dependent on the friction angle of sediments (Roscoe & Burland, 1968). Therefore, K_0, K_τ and K_{cs} and thus corresponding η_{K_0}, η_τ and η_{cs} can be determined if the friction angle is known.

According to the MCC model (Roscoe & Burland, 1968), under any constant effective stress ratio (K) condition, the void ratio of sediments is a function of mean effective stress:

$$e = e_K - \lambda \cdot \ln(s') \tag{3-6a}$$

where e is the void ratio corresponding to s', e_K the void ratio at an average stress of unity, and λ the slope on the ln(s')-e plot. The ln(s')-e relationship at any stress state (K) can be derived when that at one specific state is known (e.g., Azizi, 2000). In s'-t space (Figure 4), the yield surface (gray dash line) is the boundary between elastic and plastic deformation. Assuming that the elastic deformation is negligible, it also represents the iso-void ratio surface, which describes the stress evolution under undrained condition.

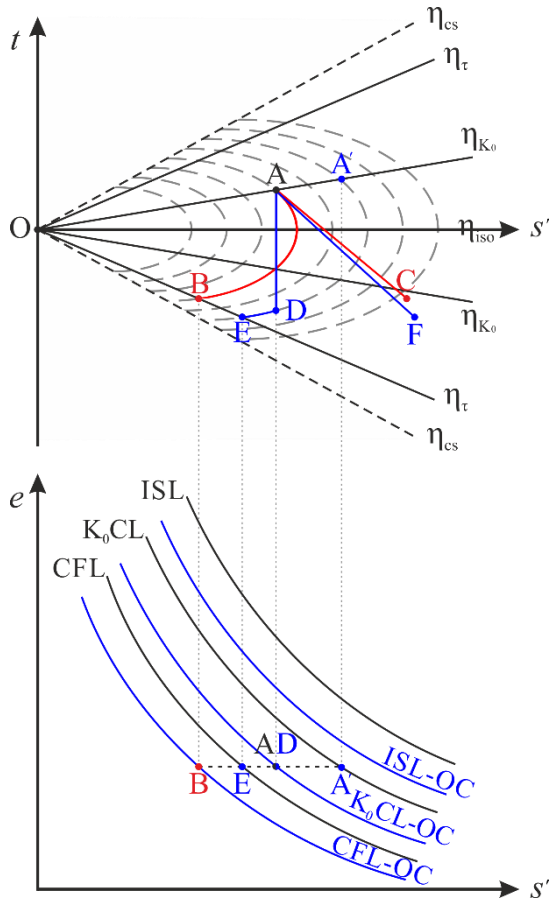

Figure 3-4. Evolution of stress and void ratio under different stress conditions for both normally consolidated and overconsolidated sediments. ISL = isotropic stress consolidation line; K_0CL = K_0 consolidation line; CFL = Coulomb failure line; ISL-OC = isotropic stress consolidation line for overconsolidated sediments; K_0CL-OC = K_0 consolidation line for overconsolidated sediments; CFL-OC = Coulomb failure line for overconsolidated sediments.

In subduction zones, the sediment passing into the accretionary prism is initially deposited outside the prism and the burial of sediments is generally considered as K_0 consolidation (e.g., Yamamoto et al., 2013). Therefore the stress path of sediments firstly follows OA in Figure 4. With the sediments accreted on the overriding plate, the horizontal stress increases and the average of the principal stresses follows AC until the sediment reaches Coulomb failure. If the sediment is undrained, the average of principal effective stresses follows AB and crosses the Coulomb failure

line at point B. The stress difference between points C and B is the excess pore pressure generated due to horizonal compression under undrained condition.

Using moisture and density (MAD) measurements at reference Site 1173, Flemings and Saffer (2018) established the ln(s')-e relationship under K_0 consolidation condition for sediments along Muroto transect. Based on the MCC model under plane strain condition and the stress path of normally consolidated sediments in subduction zones, they further derived the stress ratio (K_τ) and the ln(s')-e relationship at Coulomb failure by assuming a constant friction angle and then calculated the excess pore pressure under undrained condition.

However as described in section 3.2, the sediment in the Nankai Trough is widely overconsolidated. For overconsolidated sediments, the effective stress path under undrained condition does not follow AB in Figure 4. Instead, s' remains constant inside the elastic wall and then decreases on the Roscoe surface after passing point D and finally reaches Coulomb failure at point E (see Roscoe and Burland (1968) and related publications (e.g., Azizi, 2000) for detailed theory). In s'-t space (Figure 4), the preconsolidation stress of overconsolidated sediments corresponds to point A', the stress path DE is on the iso-void ratio line crossing point A' (Figure 4). On the other hand, the mean principal stress follows AF. Hence the excess pore pressure for overconsolidated sediments under undrained condition is the stress difference between points F and E.

As illustrated in Figure 4, overconsolidated sediments have smaller e at the same average effective stress, compared with normally consolidated sediments. To reach the same e for normally consolidated sediments, the average effective stress should increase to $s_{oc}' = OCR \cdot s'$. Substituting it into equation (3-6a), we have:

$$e = e_K - \lambda \ln(OCR) - \lambda \ln(s') \tag{3-6b}$$

Defining $e_{Koc} = e_K - \lambda \ln(OCR)$, it represents the void ratio at an average stress of unity for overconsolidated sediments and $\lambda \ln(OCR)$ denotes the magnitude of decreased void ratio relative to that of normally consolidated sediments (Figure 4). Considering the sediments along Muroto transect is overconsolidated, the established ln(s')-e relationship (Flemings & Saffer, 2018) under K_0 consolidation condition can be written as:

$$e = e_{K_0 oc} - \lambda \cdot \ln(s') \tag{3-6c}$$

The ln(s')-e relationship for normally consolidated sediments under K_0 consolidation condition can be acquired, since $e_{K_0} = e_{K_0 oc} + \lambda \cdot \ln(OCR)$. Based on the MCC model under plane strain condition (Roscoe & Burland, 1968), the stress ratio (K_τ) and the ln(s')-e relationship for normally consolidated sediments at Coulomb failure can be derived. The pore pressure under undrained condition is calculated as follows: (1) using the ln(s')-e relationship at Coulomb failure and e to

compute s' at point E; (2) utilizing s' and K_τ to estimate $\sigma_v^{'}$; and (3) employing equation (3-2) to calculate the pore pressure, where σ_v is calculated by equation (3-1).

Consequently, the equation to calculate the pore pressure in an accretionary prism from void ratio for overconsolidated sediments is:

$$P = \sigma_v - (1-\sin\phi)\cdot\exp(\frac{e_{K_0 oc}+\lambda\cdot\ln(OCR)+\lambda\cdot\ln(C)-e}{\lambda}) \tag{3-7}$$

where ϕ is the friction angle of sediments and C is a dimensionless quantity dependent on the friction angle. C is given by:

$$C = \frac{M^2+3\cdot\sin^2\phi}{2\cdot\left(M^2+3-\sqrt{3M^2+9}\right)} \tag{3-8}$$

where M is the slope of critical state line in the average effective stress-deviator stress space based on MCC model (Roscoe & Burland, 1968) and can be calculated from the friction angle:

$$M = \frac{6\cdot\sin\phi}{3-\sin\phi} \tag{3-9}$$

In comparison, the equation to calculate the pore pressure in underthrust section from void ratio for overconsolidated sediments is:

$$P = \sigma_v - \sqrt{1+\frac{M^2}{3}}\cdot\exp(\frac{e_{K_0 oc}-e}{\lambda}) \tag{3-10}$$

3.4 Model Applications

The NC model by Flemings and Saffer (2018) contains two sub-models: an intact sediment model and a weak fault model. The intact sediment model assumes the accretionary prism is in a state of Coulomb failure without effects of faults, while the weak fault model hypotheses that the stress state is affected by the properties of preexisting weak faults such that the accretionary prism reaches Coulomb failure in advance or the accretionary prism is not at Coulomb failure (Flemings & Saffer, 2018). In this study, we applied the normally consolidated intact sediment and weak fault models as well as our OC model to (1) Sites 808, 1174 and C0023 to compare the results with experimental data, and (2) Muroto transect where porosity profile can be derived from seismic velocity data to characterize the two-dimensional pore pressure distribution in the Nankai Trough.

3.4.1 Single-Site Pore Pressure Estimates

The MAD data at Sites 808, 1174 and C0023 (Figure 2) were employed to estimate the pore pressure. However, because the MAD measurements were conducted at atmospheric pressure, the

void ratio has to be corrected for rebound (e.g., Hamilton, 1976; Rea & Gaillot, 2004; Kitajima et al., 2017). Although our model assumes that the elastic deformation is negligible compared to plastic deformation, our rebound correction is to obtain more accurate in situ void ratio values and does not contradict with the assumption in the model. Following Rea and Gaillot (2004), the void ratio correction Δe was estimated by:

$$\Delta e = \log(\sigma'_v) \cdot c_e \tag{3-11}$$

where c_e is the expansion index. We computed σ'_v by subtracting the hydrostatic pore pressure from lithostatic stress which is estimated by equation (3-1) using uncorrected shipboard bulk density data (Taira et al., 1991; Moore et al., 2001; Heuer et al., 2017). For c_e values, an average c_e = 0.023 determined by consolidation tests on samples from Site C0023 was employed (Zhang et al., 2021). We then subtracted Δe from measured void ratio and substituted the corrected void ratio into equations (3-7) and (3-10) to estimate the pore pressure. In the calculations, a sediment friction angle of 15°, an *OCR* = 1.76 averaged from Sites 1173, 1174, 808, and C0023, and $e_{K_0 oc}$ =1.16 and λ =0.463 after Flemings and Saffer (2018) were used.

The sediment friction angle of 15° not only corresponds to the friction coefficient of 0.27 reported by Ikari and Kopf (2017), but also is similar to the estimated value of 17° from the classical Coulomb wedge theory. Based on the theory of noncohesive critical Coulomb wedges (Dahlen, 1984; Wang & Hu, 2006), the critical taper angle is calculated by:

$$\alpha + \beta = \psi_b^c - \psi_0^c \tag{3-12}$$

where α is the surface slope, β is the décollement dip, ψ_b^c is the angle between $\sigma_1^{'}$ and the décollement surface at critical state, and ψ_0^c is the angle between $\sigma_1^{'}$ and the slope surface at critical state. ψ_b^c and ψ_0^c are determined by:

$$\psi_b^c = \frac{1}{2} \cdot \arcsin\left(\frac{\sin\phi_b^{'}}{\sin\phi}\right) - \frac{1}{2} \cdot \phi_b^{'} \tag{3-13a}$$

$$\psi_0^c = \frac{1}{2} \cdot \arcsin\left(\frac{\sin\alpha^{'}}{\sin\phi}\right) - \frac{1}{2} \cdot \alpha^{'} \tag{3-13b}$$

where $\phi_b^{'}$ and $\alpha^{'}$ are defined by:

$$\phi_b^{'} = \arctan\left[\left(\frac{1-\lambda_b^*}{1-\lambda^*}\right) \cdot \tan\phi_b\right] \tag{3-14a}$$

$$\alpha' = \arctan\left[\left(\frac{1-\rho_w/\rho}{1-\lambda^*}\right) \cdot \tan\alpha \right] \quad (3\text{-}14b)$$

where λ_b^* and λ^* are the generalized Hubbert-Rubey fluid pressure ratio along the décollement and within the accretionary prism, respectively, ρ_w is the density of pore water, and ϕ_b is the friction angle of the décollement. To simplify the calculation, $\phi = \phi_b$ was assumed. Then we utilized $\lambda^* = 0.7$ and $\lambda_b^* = 0.9$ after Zhang et al. (2021), α = 1.5° and β =2.6° after Saffer and Bekins (1998), $\rho_w = 1.024$ cm^3/g (e.g., Dugan & Germaine, 2008), and $\rho = 2.126$ averaged from Site C0023 to solve equations (3-12) to (3-14) and obtained the sediment friction angle of 17°.

In addition, we calculated the pore pressure by NC model using the same parameters with our OC model. For the weak fault model, a weak fault friction angle of 5° after Flemings and Saffer (2018) was used. Then the pore pressure estimates by both NC and OC models were compared with the experimental data. To explore the effects of *OCR* on pore pressure estimates, we also calculated the normalized pore pressure results under different *OCR* values using data from Site 1174 at 200, 400, 600 and 800 mbsf, respectively, because the porosity fluctuation at Site 1174 is relatively small (Figure 2).

3.4.2 Two-Dimensional Pore Pressure Distribution

To characterize the two-dimensional pore pressure distribution along Muroto transect, we transformed the seismic velocity into porosity and thus void ratio and then estimated the pore pressure by both NC and OC models. The seismic interval velocity by Costa Pisani et al. (2005) that was calibrated using borehole data was employed. Although previous research reported velocity-porosity transforms in the Nankai Trough, the transform equations were either based on wireline logging (e.g., Hoffman & Tobin, 2004) or focusing on the Kumano transect (e.g., Kitajima et al., 2017). We therefore established a new equation by combining seismic interval velocity with shipboard porosity measurements. The velocity model of inline 284 (Costa Pisani et al., 2005) and the corrected shipboard porosity at Site 808 were employed, since inline 284 crosses Site 808. We firstly extracted the velocity data close to Site 808 from inline 284 and then picked the velocity data located ±1 m from porosity measurements, because the sampling depths of seismic velocity and porosity were not matched. Erickson and Jarrard (1998) proposed an empirical velocity-porosity transform for global siliciclastic sediment which takes shale fraction and consolidation history into account and merges different velocity-porosity trends above and below critical porosity in one equation. We followed their method and used an equation in the form as below:

$$Vp = 1/(i \cdot n + j) + (k \cdot Vsh + l) \cdot \{\tanh[20 \cdot (n - n_c)] - |\tanh[20 \cdot (n - n_c)]|\} + w \quad (3\text{-}15)$$

where Vp is seismic interval velocity, n porosity, Vsh shale fraction, n_c critical porosity, and i, j, k, l and w are empirical parameters. In equation (3-15), $1/(i \cdot n + j)$ represents the part of time-

average relationship (Wyllie et al., 1956), whereas $(k \cdot Vsh + l) \cdot \{\tanh[20 \cdot (n - n_c)] - |\tanh[20 \cdot (n - n_c)]|\}$ accounts for the effects of shale fraction, consolation history and critical porosity referred from Erickson and Jarrard (1998). In this study, a Vsh = 0.32 after Hoffman and Tobin (2004) and a n_c = 0.42 observed on cross plots of seismic velocity and corrected porosity (Figure 5) were used. The other empirical parameters (i.e. *i, j, k, l and w*) are constrained by fulfilling the following assumptions: (1) n = 1 when the velocity is equivalent to a water velocity of 1.5 km/s; (2) n = 0 and Vsh = 0 when the velocity equals to the average sand velocity of 5.49 km/s (Raymer et al., 1980); (3) n = 0 and Vsh = 1 when the velocity equals to the average shale velocity of 4.3 km/s (Erickson & Jarrard, 1998). Consequently only two empirical parameters are independent variables. We therefore used i from 0 to 10 and w from -5 to 5 with an interval of 0.01 to calculate porosity from velocity data. The best fit empirical parameters (i = 1.80, j = 0.24, k = 0.60, l = -0.16 and w = 1.01) were determined when the misfit between the predicted and measured porosity is minimum.

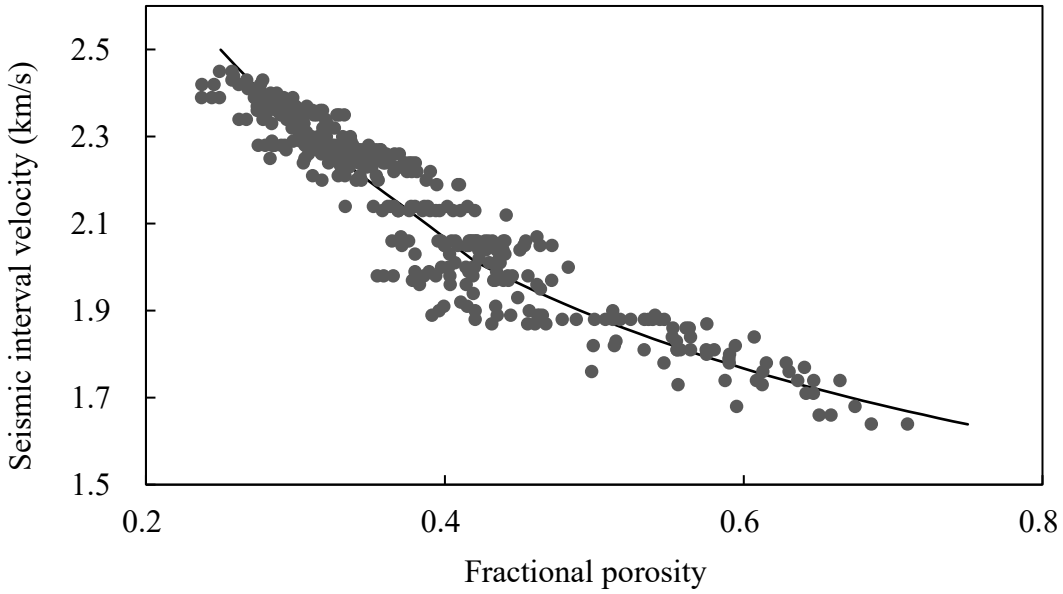

Figure 3-5. Fractional porosity (φ) versus seismic interval velocity (Vp) at Site 808. The black line represents the regression formula following equation (3-15).

With the best fit equation, we transformed the seismic velocity into porosity, from which we calculated the bulk formation density using a water density of 1.024 cm^3/g and an experimentally determined average grain density of 2.79 cm^3/g at Site C0023. Then we computed σ_v with equation (3-1). Similar with Sites 808, 1174 and C0023, we assumed a friction angle of 15° (Casey et al., 2016) and OCR = 1.76 and employed equations (3-7) and (3-10) to estimate the pore pressure distribution along Muroto transect by both NC and OC models, after transforming the porosity into void ratio.

3.5 Results

3.5.1 Sites 808, 1174 and C0023

Our results show excess pore pressure in both accreting and underthrusting sediments at Sites 808, 1174 and C0023 (Figure 6). For each site, NC (intact sediment and weak fault) and OC models predict same excess pore pressure in the subducted sediments, while different excess pore pressure is predicted by these models in the accretionary prism. The OC model generates 40%-50% lower excess pore pressure on average than that by intact sediment model. In comparison, the pore pressure estimates by OC and weak fault models are in good agreement. Moreover, in contrast to a sharp decrease of excess pore pressure across the décollement from the intact sediment model, OC and weak fault models reveal a continuous pore pressure increase across the accreted and underthrust sequence. Based on the results by our OC model, Site 808 has relatively higher excess pore pressure throughout the profile with main pore pressure ratios ($\lambda_P = P/\sigma_v$) of 0.7-0.9, whereas the pore pressure ratios at Sites 1174 and C0023 are mainly in a range of 0.6-0.8 and 0.7-0.8, respectively. For the underthrust sequence, the excess pore pressure at Site 808 generally ranges from 5 MPa to 7 MPa while that at Sites 1174 and C0023 are dominantly between 3 MPa and 5 MPa. In respect of the accreting sediments, the pore pressure increases from hydrostatic to 5 MPa in excess of hydrostatic at Site 808 and 4 MPa at Sites 1174 and C0023, respectively.

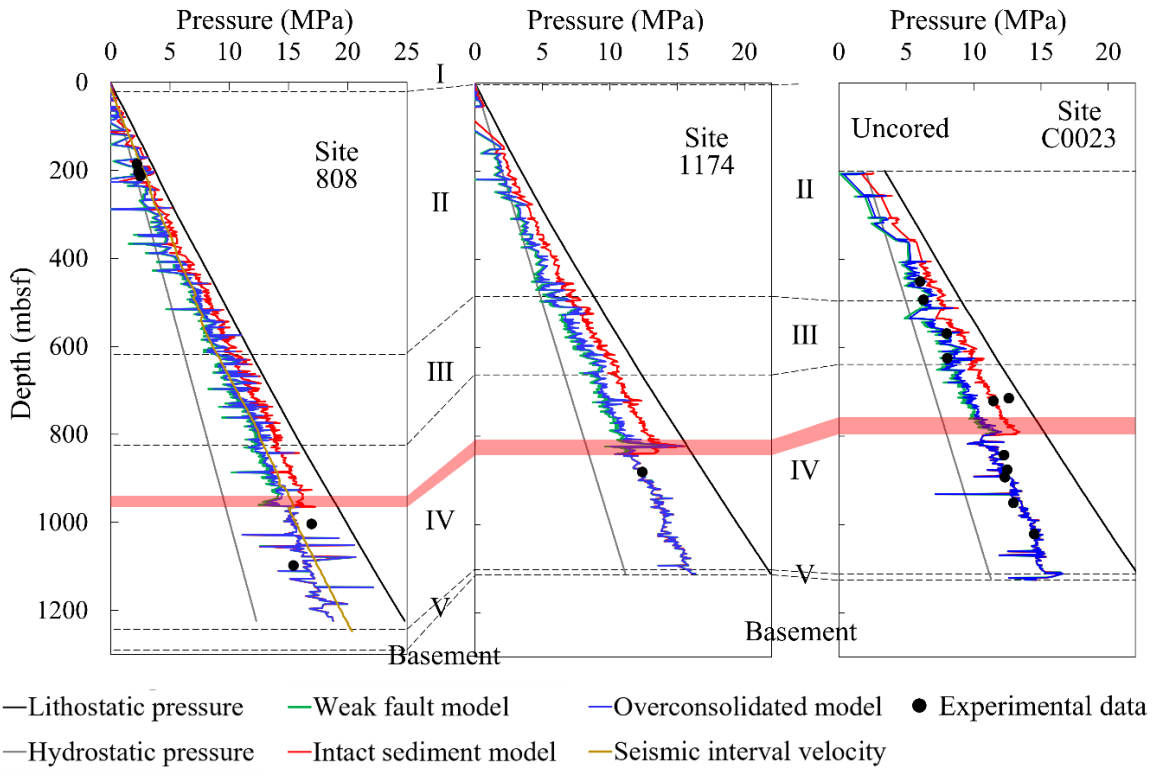

Figure 3-6. Estimated pore pressures at Sites 808, 1174 and C0023. Experimental data are from Karig (1993), Moran et al. (1993), Morgan and Ask (2004) and Zhang et al. (2021). I = slope-

apron facies, II = trench-wedge facies, III = upper Shikoku Basin facies, IV= lower Shikoku Basin facies, and V = volcaniclastic facies. Red shading marks the location of the décollement.

At Site 1174, P/P_{intact}, which is defined as the ratio of estimated pore pressure with OC model to that estimated by intact sediment model and equivalent to pressure coefficient *B* (section 6.1), decreases with increasing *OCR* values (Figure 7). The P/P_{intact} values at 200, 400, 600 and 800 mbsf consistently decrease from 1 and reach 0.42, 0.59, 0.63, and 0.64, respectively, when *OCR* values increase to 3. Similar to P/P_{intact}, the pore pressure ratio ($\lambda_P = P/\sigma_v$) also decreases with the increase of *OCR* (Figure 7). The pore pressure ratios are in a range of 0.78-0.85 when *OCR* = 1, and gradually decrease to 0.33-0.55 when *OCR* values rise to 3.

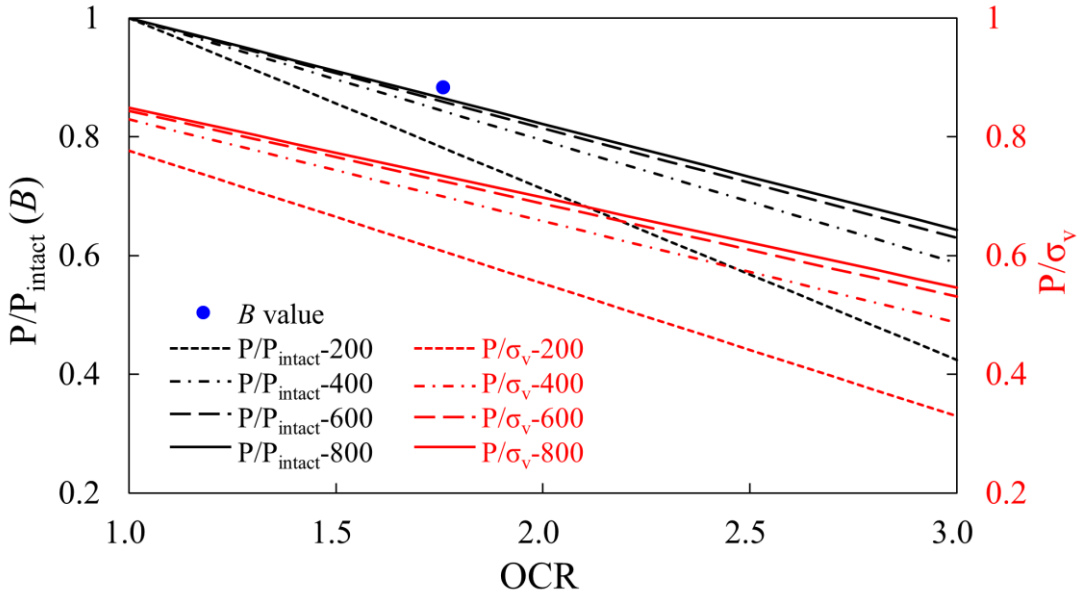

Figure 3-7. The normalized pore pressure results under different *OCR* values using data from Site 1174 at 200, 400, 600 and 800 mbsf show the effects of *OCR* on estimated pore pressures. P_{intact}= pore pressure estimates by intact sediment model. Note that P/P_{intact} is equivalent to pressure coefficient *B*.

3.5.2 Muroto Transect

Our data show wide-spread excess pore pressure along Muroto transect from both intact sediment and OC models (Figure 8). The excess pore pressure increases progressively landward from the trench and the maximum excess pore pressure reaches to as large as 20 MPa. Similar to the results of Site C0023, the intact sediment model predicts higher excess pore pressure and indicates a distinct decrease of excess pore pressure across the décollement, whereas the excess pore pressure predicted by our OC model is lower and obvious variation of excess pore pressure is absent from the accretionary prism to underthrust section. Also, the excess pore pressure increases with depth in general. Based on the results by OC model, the excess pore pressure is lower than 5 MPa above

5000 mbsl (meters below sea level) while it increases to 12 MPa at 6000 mbsl and reaches to as large as 20 MPa at the base of underthrust section.

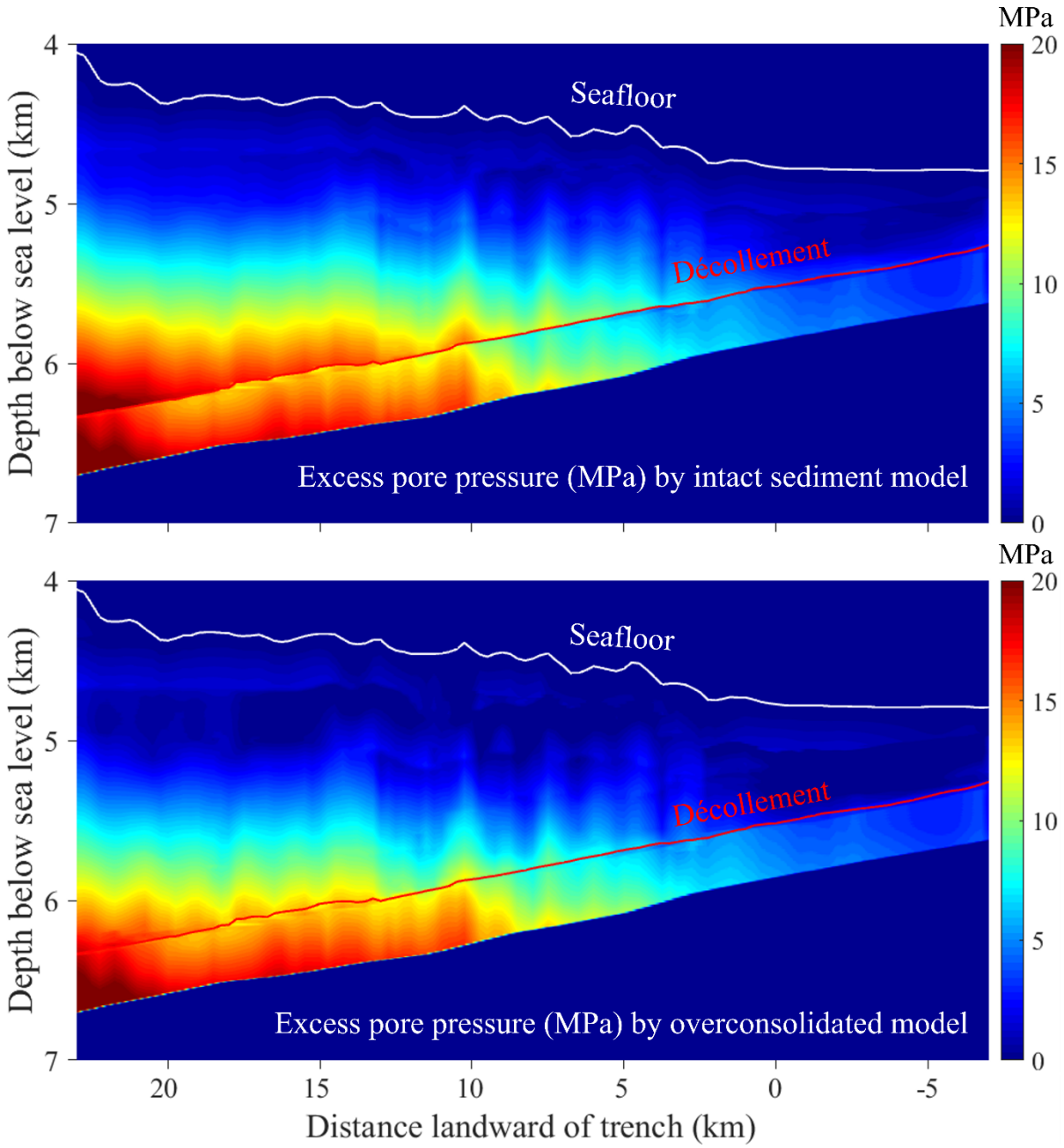

Figure 3-8. Estimated pore pressures by both intact sediment model and overconsolidated model along inline 284 seismic section in the Nankai Trough.

3.6 Discussion

3.6.1 Pore Pressure Estimates

The results from our OC model for both single-sites and the Muroto transect reveal wide-spread excess pore pressure in both underthrust sediments and accretionary prism (Figures 6 and 8). The excess pore pressure increases with depth and distance from the trench and is in unison with the concept of pore pressure distribution in the accretionary prism (e.g., Ienaga et al., 2006; Flemings & Saffer, 2018). The pore pressure estimates at Sites 808, 1174 and C0023 are consistent with previous results by consolidation experiments (Karig, 1993; Morgan & Ask, 2004; Zhang et al., 2021) as well as porosity inversion based on hydrogeological models (Skarbek & Saffer, 2009), corroborating the validity of our OC model in pore pressure prediction. We also note that the pore pressure estimates by the weak fault model using a weak fault friction angle of 5° are generally consistent with the experimental results as well. But a preexisting fault weaker than the décollement is disputable in the accretionary prism, considering the décollement has a low friction coefficient of 0.27 (Ikari & Kopf, 2017) and a high pore pressure ratio of 0.9 (Zhang et al., 2021). In comparison, our OC model relates pore pressure estimates to consolidation state and reproduces the experimental data without introducing a weak fault. Another hint showing pore pressure is related to the consolidation state is that Tsuji et al. (2008) obtained similar pore pressure results along the Muroto transect to ours by considering crack sealing. These authors established a theoretical acoustic velocity-mean effective stress relationship based on differential effective medium theory and estimated the in situ mean effective stress (and thus pore pressure) by iteratively fitting the stress-dominated velocity to seismic velocity. They accounted for cementation associated with heating by using landward decrease of crack concentration (crack sealing). However, the two high excess pore pressures above the décollement derived from uniaxial consolidation experiments at Site C0023 were absent in our results (Figure 6), because (1) the velocity model flattens the gathers (Costa Pisani et al., 2005) and (2) porosity change by unloading through transient pore pressure increase is relatively small (e.g., Nobes et al., 1991). Based on the results from both single-sites and Muroto transect, the pore pressure increases continuously across the décollement and supports the recent view that the décollement may not be a fluid barrier in the Nankai Trough (Zhang et al., 2021).

Compared to the results from Flemings and Saffer (2018) as well as our own pore pressure estimates by the intact sediment model, the OC model predicts 40% ~ 50% less excess pore pressure in accreting sediments (Figure 6), implying that the overconsolidation inhibits the development of excess pore pressure. Further, it is clear that the pore pressure results decrease with increasing *OCR* (Figure 7). But with the consolidation of sediments (increasing depth), the inhibition effects of *OCR* on pore pressure development weakens. Compared with the pore pressure estimates by intact sediment model, an $OCR = 3$ causes a decrease of 58% and 36% pore pressure for sediments at 200 and 800 mbsf, respectively. For the underthrust section, both intact

sediment model and our OC models yield same pore pressure, which is attributed to the consolidation state of the sediments at the reference site. The equation (3-6a) was built on reference Site 1173 where sediments are overconsolidated, therefore the overconsolidation state has been taken into account when predicting pore pressure by the NC model.

The inhibition effects of *OCR* on pore pressure development can be explained by the concept of pore pressure coefficients (Skempton, 1954). With the increase of total stress, the pore pressure change ΔP under undrained condition is:

$$\Delta P = B \cdot [\Delta\sigma_3 + A \cdot (\Delta\sigma_1 - \Delta\sigma_3)] \tag{3-16a}$$

$$B = \frac{m_v}{m_v + n \cdot \beta_f} \tag{3-16b}$$

where $\Delta\sigma_1$ and $\Delta\sigma_3$ are increments of maximum and minimum principal stress, A and B are pressure coefficients, and m_v and β_f are compressibility of the formation and pore fluids, respectively. B is also called loading efficiency (e.g., Sawyer et al., 2008). For normally consolidated sediments, m_v is far larger than β_f, making $B \approx 1$. In contrast, m_v decreases substantially for overconsolidated sediments, causing the decrease of B. Therefore, compared with normally consolidated sediments, the overconsolidated ones generate less excess pore pressure under undrained loading condition. Our consolidation experiments at Site C0023 yield average m_v values of 1.7×10^{-9} Pa^{-1} in the unloading phase. The B value for overconsolidated sediments is estimated using $m_v = 1.7\times10^{-9}$ Pa^{-1}, n=0.45 and $\beta_f = 5\times10^{-10}$ Pa^{-1} (Fetter, 2013). The result of B = 0.88 is similar to the P/P_{intact} values (0.85, 0.86, 0.87) from Site 1174 at 400, 600 and 800 mbsf when *OCR*=1.76 (Figure 8).

3.6.2 Implications for Stability of the Subduction Thrust Faults

Based on the mechanics of earthquakes and faulting, the friction stability of the fault is described by the friction stability parameter ζ:

$$\zeta = (a\text{-}b) \cdot \sigma_e \tag{3-17}$$

where a and b are velocity-dependent frictional properties of material, and σ_e is the effective normal stress on the slip plane (Scholz, 1998). The fault with negative ζ is either unstable (large negative values of ζ) or conditionally stable (small negative values of ζ), while positive ζ indicates the fault is intrinsically stable. It has been recognized that the diagenetic processes in the subduction zone drives the velocity dependence $(a\text{-}b)$ to more negative (Moore & Saffer, 2001). Our study suggests that the diagenetic processes not only exert effects on $(a\text{-}b)$, but also prevents the increase of excess pore pressure by strengthening the sediment and increasing the consolidation state (e.g., Morgan & Ask, 2004), which facilitates the instability of faults and thus the generation of earthquakes.

With the pore pressure results along the décollement, we calculated the shear stress and shear strength, respectively. Shear strength is the maximum shear stress that the sediment can sustain before shear failure takes place, and was calculated by the effective stress acting on the fault plane times a friction coefficient of 0.27 after Ikari and Kopf (2017). The effective stress and shear stress on the fault were calculated from the component of $\sigma_v^{'}$ and $\sigma_h^{'}$ on the fault plane using a décollement dip angle of 2.6° (Saffer & Bekins, 1998). The shear strength is below 2.2 MPa (Figure 9), lower than previous estimates of 4 MPa by Tobin and Saffer (2009), where a higher friction coefficient of 0.4 was used. In contrast, the shear stress along the décollement is below 0.4 MPa, obviously lower than the estimated shear strength (Figure 9). This implies that the accretionary prism is not at Coulomb failure, which is consistent with the dynamic Coulomb model that the sediment in the outer wedge is brought back to a stable elastic regime in the postseismic interval (Wang & Hu, 2006).

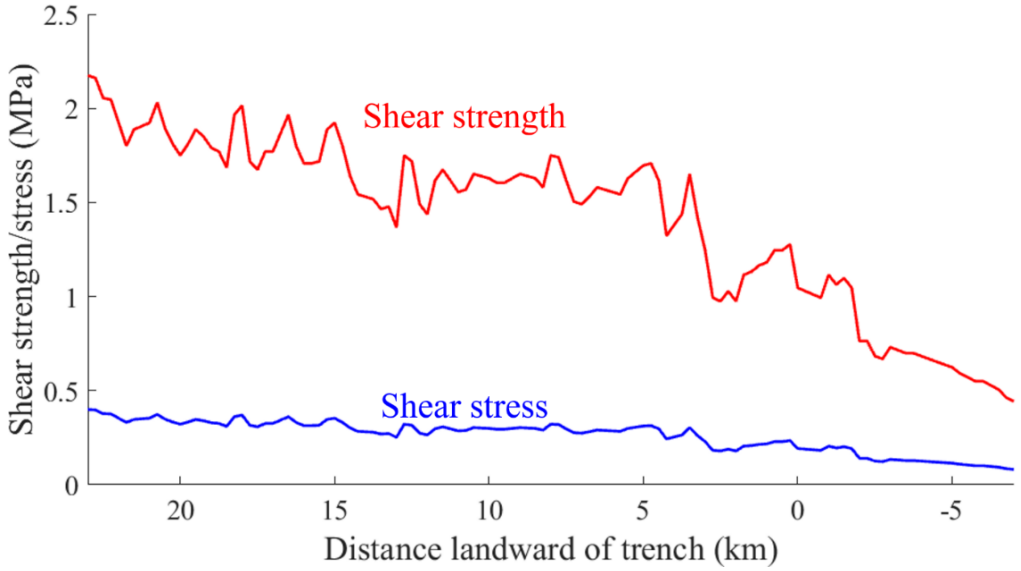

Figure 3-9. The stress state of the décollement in the Nankai Trough inferred from the pore pressure results by overconsolidated model.

According to the theory of dynamic Coulomb wedge, when the wedge is in a stable state, ψ_b^c and ψ_0^c in equation (3-12) become ψ_b and ψ_0, and there is always an equivalent solution to the critical state for a given wedge geometry. ψ_b is the angle between $\sigma_1^{'}$ and the décollement surface at stable state, whereas ψ_0 is the angle between $\sigma_1^{'}$ and the slope surface. With a friction coefficient of 0.27 after Ikari and Kopf (2017) as well as the same parameters in section 4.1, we solved equation (3-12) at stable state using equations (3-16) and (3-17) in Wang and Hu (2006) and obtained an in situ effective stress ratio $K = 0.61$. This value is similar to $K = 0.59$ calculated from the friction angle of 15°. In NC and OC models, a key parameter determined by the state of Coulomb failure is η_τ which controls the pore pressure results (Figure 4). Based on equation (3-

5), η_τ is a function of effective stress ratio K. Therefore, although both NC and OC models assume a state of Coulomb failure which is not applicable to Nankai accretionary prism, the error of pore pressure estimates should be small considering the difference between $K = 0.59$ and $K = 0.61$ is negligible. Our study shows that NC and OC models are not limited to the accretionary prism at Coulomb failure, but can be expanded to a dynamic Coulomb wedge in a stable state, if the in situ effective stress ratio is acquired.

3.6.3 Implications for Submarine Landslides in Subduction Zones

In subduction zones, the submarine landslide is another destructive threat to populated coastal cities in addition to earthquakes (e.g., Hornbach et al., 2010). Many submarine landslides are triggered by earthquakes (e.g., Stigall & Dugan, 2010). But it has been widely recognized that the recurrence rates of submarine landslide are obviously lower than those of large earthquake in high seismicity areas (e.g., McAdoo et al., 2000; McAdoo et al., 2004; Strozyk et al., 2010). Seismic strengthening, which hypothesizes that small earthquakes tend to strengthen the slope material by seismic loading, has been invoked to explain this phenomenon (e.g., Locat & Lee, 2002). Ikari and Kopf (2015) further related seismic strengthening to overconsolidation where apparent increases of cohesion and thus shear strength were observed in clayey sediments when $OCR > 4$. Based on our results, we suggest that overconsolidation can suppresses the development of excess pore pressure during and after earthquakes, which inhibits the shear strength of slope material from decreasing and reduces the likelihood of slope failure. This is supported by recent undrained cyclic triaxial tests where the excess pore pressure in overconsolidated clays after cyclic loading is obviously less than that in normally consolidated clays (Shi et al., 2018). Using the pore pressure estimates in the Nankai Trough, $OCR=2$ inhibits 50% excess pore pressure while $OCR=4$ inhibits 90% excess pore pressure. Therefore, our findings provide a supplement to the explanation for the slope failure behavior in seismically active regions. Compared with Ikari and Kopf (2015), our explanation is applicable to all kinds of slope material and does not require OCR values to reach 4.

3.7 Conclusions

In this study, we explored the effect of overconsolidation on pore pressure development by introducing the consolidation state of sediments into the model proposed by Flemings and Saffer (2018). The overconsolidated sediment in the Nankai Trough generates 40%~50% less excess pore pressure than the normally consolidated sediment, suggesting that overconsolidation inhibits the development of excess pore pressure. The lower excess pore pressure in overconsolidated sediments is attributed to the decrease of loading efficiency. This provides a supplement to the explanation for the slope failure behavior in seismically active regions: overconsolidated sediments suppress the pore pressure build-up and thus inhibit the shear strength of slope material from decreasing, which reduces the likelihood of slope failure. But on the other hand, the inhibition

of excess pore pressure development in the deep-seated sediment facilitates the instability of faults and thus the generation of earthquakes by driving the friction stability parameter ζ more negative. Our pore pressure estimates yield a low shear strength (< 2.2 MPa) of the décollement in the Nankai accretionary prism off Muroto Peninsula, while the shear stress (< 0.4 MPa) is even considerably lower. This implies that the accretionary prism is not at Coulomb failure.

Chapter 4: Pore Pressure Prediction and Modeling in the North Sumatra Subduction Zone: Implications for Tsunami Hazard

Junli Zhang[1], Andre Hüpers[1], Huan Li[2], and Achim Kopf[1]

[1]MARUM—Center for Marine Environmental Sciences and Faculty of Geosciences, University of Bremen, Bremen, Germany

[2]School of Earth Sciences, University of Melbourne, Melbourne, Australia

Corresponding author: Junli Zhang (jzhang@marum.de)

Abstract

As a critical parameter controlling the dynamics of subduction zones, pore fluid pressure has not been well quantified in the North Sumatra subduction zone where the 2004 great Sumatra-Andaman earthquake occurred. Using consolidation experiments and numerical modeling work, we provide robust estimates of pore pressure at IODP Sites U1480 and U1481, ~225 km seaward of the trench. Our data reveal moderate excess pore pressure in a horizon which is considered as a proto-décollement. We further simulated the pore pressure evolution through a one-dimensional sedimentation-flow model which accounts for the sedimentation rate and silicate dehydration. The modelling results show that ~50% of the excess pore pressure at the present is attributed to high sedimentation rate while the other half is caused by silicate dehydration. With the rapid burial and progressive silicate dehydration, the excess pore pressure continuously increases and reaches a high level corresponding to a pore pressure up to 96% of lithostatic stress. At the deformation front, silicate dehydration contributes ~66% of the excess pore pressure and correspondingly the overpressure contribution from rapid sedimentation decreases to ~34%. Based on our results, high excess pore pressure is inferred along the décollement and is invoked to explain the landward-vergent frontal thrusts. We suggest that the high excess pore pressure in the near-trench faults facilitates the propagation of coseismic slip all the way to the trench and, thus, potentially increases the tsunami size in the 2004 great Sumatra-Andaman earthquake.

4.1 Introduction

The plate-boundary thrust faults in subduction zones host the largest earthquakes (Pacheco & Sykes, 1992). Based on the prevailing model of seismogenic behavior in subduction zones, the material in the outer subduction thrust system is aseismic and the seismic rupture cannot propagate to the trench (e.g., Moore & Saffer, 2001). However, coseismic slip extending closely to the trench was inferred in the 2004 Sumatra-Andaman and 2011 Tohoku earthquakes (e.g., Bletery et al., 2016; Fujiwara et al., 2011). Multiple studies using different approaches consistently suggested that the 2004 Sumatra-Andaman earthquake had a large rupture extent and a slip of 10-20 m near the trench was estimated (Chlieh et al., 2008; Henstock et al., 2006; Rhie et al., 2007). For

comparison, more than 60 m horizontal displacement and an uplift of 5 m were measured in the frontal wedge after the 2011 Tohoku event (Ito et al., 2011). This challenges the classical subduction earthquake model. To understand the mechanism of shallow coseismic rupture, increasing attention has been paid to the physical and mechanical properties of the forearc wedge.

In the North Sumatra subduction zone where the 2004 Sumatra-Andaman earthquake occurred, several key features have been revealed by seismic reflection profiles. The oceanic plate is covered by thick sediment succession up to 5 km (McNeill & Henstock, 2014). A high amplitude negative polarity (HANP) seismic horizon was found ~500 m above the oceanic crust and was interpreted as a candidate that will develop into the plate-boundary décollement (Dean et al., 2010). Different deformation styles were observed and landward vergence of the frontal thrusts was discovered in the near-trench rupture zone with highest slips (Moeremans et al., 2014). The thick sedimentary sequence is considered to facilitate lithification of the sediments and to shift the seismogenic zone more seaward relative to the normal earthquakes (Geersen et al., 2013; Gulick et al., 2011). Recent geochemistry modeling work further suggests that complete silicate dehydration is achieved prior to subduction and is thought to drive the unexpected large shallow slip (Hüpers et al., 2017). The HANP reflector represents a low-velocity layer (Qin & Singh, 2017) and might also be related to the dehydration of silicates (Hüpers et al., 2017). Regarding the main tsunami source, the large near-trench rupture has been linked to the unusual landward-vergent frontal thrusts in the accretionary prism (Cubas et al., 2016; Moeremans et al., 2014).

Although previous studies have expanded our knowledge of the North Sumatra forearc wedge, pore pressure as a critical parameter controlling the dynamics of subduction zones, has not been well quantified in the region. In this study, we sampled the incoming sediments and conducted uniaxial consolidation experiments to investigate the pore pressure seaward of the trench. The experimental pore pressure estimates were compared with the results derived from moisture and density (MAD) data. Through a one-dimensional sedimentation-flow model, which accounts for the sedimentation rate and silicate dehydration, we further simulated the pore pressure evolution and inferred the pore pressure state in the accretionary prism. Based on our pore pressure results, we explain the key features in the North Sumatra subduction zone and provide a plausible explanation for the occurrence of large tsunamis such as that in 2004.

4.2 Geological Setting

The North Sumatra subduction zone is located at the northern plate boundary where the Indo-Australian plate is subducting beneath the Sunda plate with a subduction velocity of ~4 cm/year (McNeill & Henstock, 2014) (Figure 4-1). Many earthquakes including the M_w 9.2 2004 Sumatra-Andaman (Ammon et al., 2005) and the M_w 8.6 2005 Nias (Walker et al., 2005) events happened in this region. To investigate the properties of the incoming sediments to the North Sumatra and explore their effect on the generation of earthquakes and tsunamis, recent International Ocean Discovery Program (IODP) Expedition 362 recovered the sediment succession at Sites U1480 and

U1481 (McNeill et al., 2017a). The drill sites are ~225 km seaward of the trench (Hüpers et al., 2017). The recovered sediment represents the southern portion of the ruptured material in the 2004 earthquake before subduction and six lithologic units were identified (McNeill et al., 2017a): Unit I is the Nicobar Fan succession and comprises calcareous clay, fine grained sand and clay, and silty clay; Unit II is also the Nicobar Fan facies, composed of sandy silt and fine-grained sand dominated upper subunits and silt/siltstone and clay/claystone dominated lower subunits; Unit III is the prefan pelagic deposit and mainly contains claystone and tuffaceous silty claystone; Unit IV and V are igneous and intercalated pre-fan pelagic materials including basaltic flow, tuffaceous and volcaniclastic sandstone, volcanic breccia, calcareous claystone and chalk; Unit VI is basalt and interpreted as oceanic crust. Among them, Unit III is thought to correspond to the HANP seismic layer and will develop into the plate-boundary décollement (McNeill et al., 2017a).

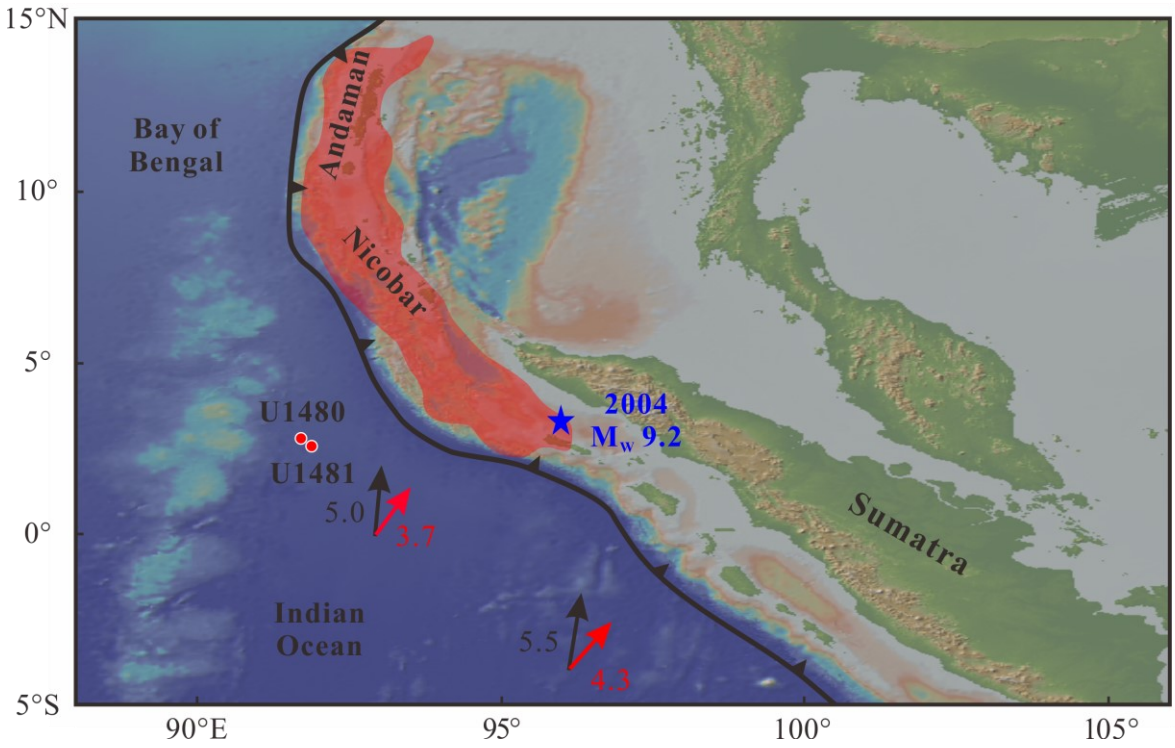

Figure 4-1. Geological setting of the North Sumatra subduction zone and the locations of IODP Sites U1480 and U1481. Figure made with GeoMapApp (www.geomapapp.org; Ryan et al., 2009). Red shading marks the major rupture zones in the M_w 9.2 2004 earthquake (Meltzner et al., 2012). Arrows and numbers indicate subduction directions and velocities (McNeill & Henstock, 2014).

The MAD data at Sites U1480 and U1481 (Figure 4-2) show that the porosity decreases rapidly from ~80% to ~50% in Unit I, after which the decreasing rate of porosity becomes slow and the porosity gradually decreases to ~30% at 1497 mbsf (meters below seafloor). This gradient of porosity decrease is lower compared to other incoming sediments to subduction zones such as Northern Barbados (e.g., Moore & Saffer, 2001) or Nankai Trough (e.g., Henry et al., 2012a, 2012b; Saito et al., 2010a, 2010b). The general decreasing trend of porosity in sand/sandstone and

mud/mudstone is similar, whereas the porosity of calcareous claystone, tuffaceous mudstone and sandstone as well as igneous rock shows obvious deviation. For mud/mudstone, abnormal high porosity is observed in Unit III, which might imply a fluid-rich horizon. In the depth profile of chloride concentration (Figure 4-2), the chlorinity at Site U1480 increases slowly from ~560 mM at the seafloor to ~580 mM at the bottom of Unit II, followed by a sudden decrease to as low as 522 mM in Unit III. At Site U1481, a similar sharp decrease is visible in Unit III but shifts downward to a depth of 1367-1495 mbsf. Geochemical modeling suggests that the rapid decrease of chlorinity is attributed to the silicate dehydration (Hüpers et al., 2017). Together with the scattered but somewhat increased porosity, excess pore pressure is expected in Unit III.

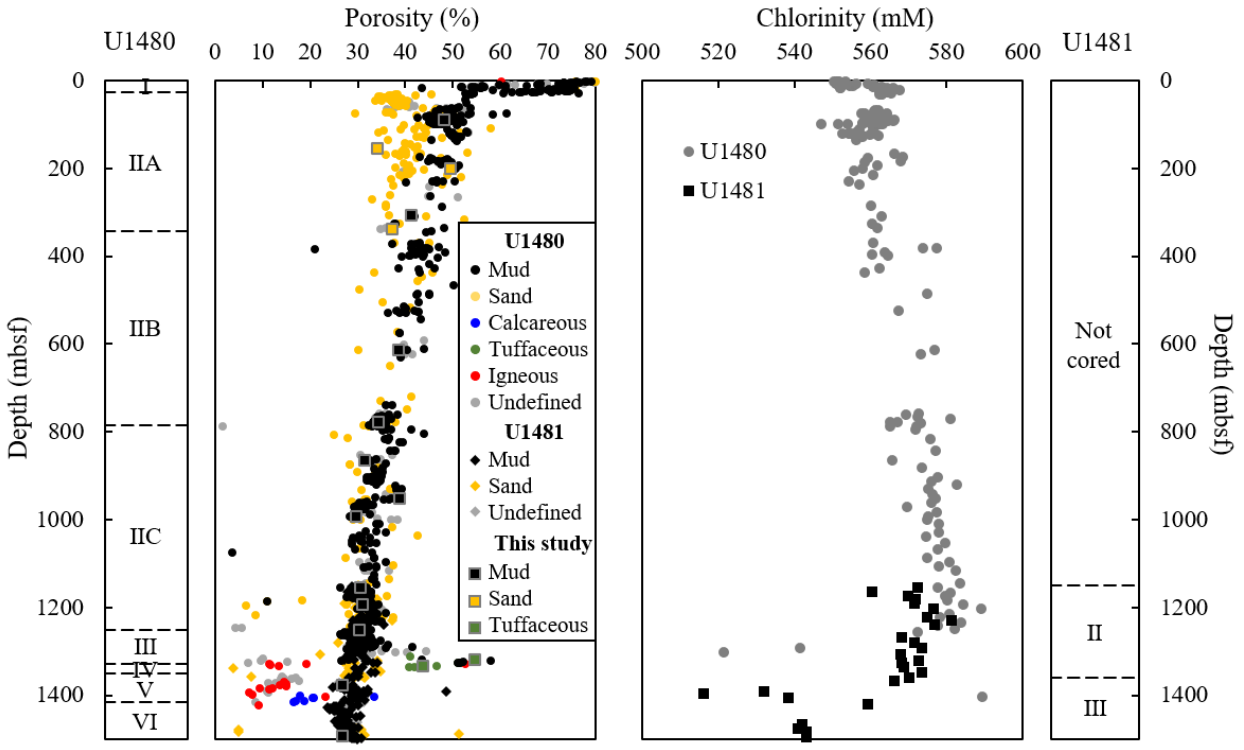

Figure 4-2. Depth profiles of porosity and chlorinity at IODP Sites U1480 and U1481 after McNeill et al. (2017a). Roman numerals indicate lithologic units. Calcareous represents calcareous claystone. Tuffaceous represents tuffaceous mudstone and sandstone.

4.3 Experimental Analysis

4.3.1 Sample Material and Consolidation Experiment

In this study, we investigated a total of 17 whole round samples collected from IODP Sites U1480 and U1481. Fourteen samples originate from Site U1480 between 89 and 1333 mbsf and include mud/mudstone, sand/sandstone, tuffaceous claystone and tuffaceous sandstone, whereas three mudstone samples are from 1193 to 1492 mbsf at Site U1481 (Table S4-1). All the samples were sealed and stored in the core liner at 4 °C to maintain the natural water content after recovery.

The samples were hand-trimmed into cylinders with a constant diameter of 25.4 mm and a height of ~10 mm. Then we conducted consolidation experiments in accordance with ASTM D2435/D2435M-11 (ASTM International, 2011) to derive the preconsolidation stress and pore pressure for each sample. The preconsolidation stress represents the maximum vertical effective stress that the sediment has experienced (Casagrande, 1936) and is denoted by σ'_{pc}. For the consolidation experiments, a uniaxial incremental loading oedometer was used. The samples were placed in the oedometer cell and kept saturated with artificial seawater (35‰), after which we applied load on the samples and increased the load regularly. The load applied on the samples was initially doubled, and then smaller increments were used when the load approached σ'_{pc}, so that σ'_{pc} can be determined more precisely (e.g., Brumund et al., 1976). Because σ'_{pc} was unknown before the test, we took the hydrostatic vertical effective stress (σ'_{vh}) as a reference, where σ'_{vh} is the lithostatic stress (σ_v) less the hydrostatic pore pressure (P_{hy}). The lithostatic stress was calculated by the integral of the shipboard measured bulk density data. During the consolidation test, each load was maintained for 24 hours to dissipate the excess pore pressure completely. Based on the σ'_{vh} estimates, the expected σ'_{pc} stresses cover a large range of 0.7-17.5 MPa. Therefore, we increased the maximum load for deep samples to produce more data points at higher stresses, so that σ'_{pc} could be determined with more precision. In this study, a maximum load of up to 46.5 MPa was employed, which means our data generally can be applied to a depth of 4-5 kmbsf (kilometers below seafloor). For each sample, the change of the sample height under each load was recorded continuously by a linear variable displacement transducer (LVDT) throughout the experiments. We then derived the permeability under different stresses using the continuous time-deformation data (Taylor, 1948).

4.3.2 Evaluation of Consolidation Behavior

The consolidation behavior of the samples is illustrated in semi-logarithmic stress-strain and square-root time-strain plots (Figures 4-3 and 4-4). In the stress-strain plot (Figure 4-3), the loading curve is divided into two parts by a yield point which is normally interpreted as σ'_{pc}. The loading curve before σ'_{pc} represents the elastic recompression phase, whereas after σ'_{pc} deformation is elasto-plastic and called virgin consolidation (e.g., Knappett & Craig, 2012). In this study, we estimated σ'_{pc} by a modification of the widely used Casagrande method (McNulty et al., 1978) and the Becker method (1987). To evaluate the uncertainty of σ'_{pc} estimates, we also determined the maximum and minimum σ'_{pc} values. Following Saffer (2003), the maximum and minimum values from the modified Casagrande method were acquired from the applied stress at which the strain starts to deviate from the virgin compression and recompression lines, respectively (Figure 4-3). For the Becker method, the maximum σ'_{pc} value was obtained similarly as in the modified

Casagrande method, whereas the minimum σ'_{pc} value was derived by extrapolating the post-yield line to zero work (Figure 4-3). Considering the estimated maximum and minimum σ'_{pc} values give over-conservative estimates, we took the smaller maximum σ'_{pc} and larger minimum σ'_{pc} values as the final estimates (e.g., Zhang et al., 2021). The laboratory data are shown in the supplementary material (Table S4-2).

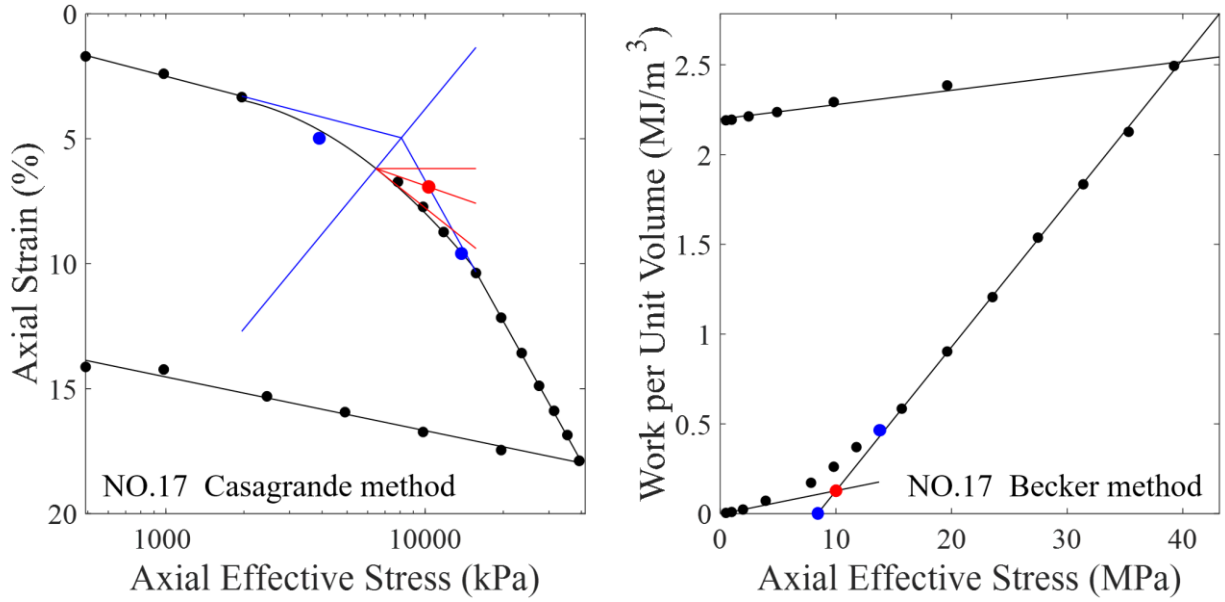

Figure 4-3. An example of the preconsolidation stress estimates based on the modification of the widely used Casagrande method (McNulty et al., 1978) and the Becker method (1987). Red dots mark the estimated preconsolidation stress. Blue dots mark the minimum and maximum possible preconsolidation stress.

Based on the continuous time-deformation data (Figure 4-4), we determined the coefficient of consolidation (c_v) under different stresses following the Taylor method (1948). With the estimated c_v values, we calculated the degree of progressive consolidation with time using the theory of consolidation (e.g., Knappett & Craig, 2012). The result was compared with the experimental data to check the accuracy of c_v values (Figure 4-4). Then the c_v value was employed to estimate the permeability by (e.g., Knappett & Craig, 2012):

$$k = c_v \cdot m_v \cdot \mu \tag{4-1}$$

where k is the permeability, m_v is the coefficient of volume compressibility calculated from the experimental data and μ is the viscosity of pore water (0.001 Pa s) at room temperature.

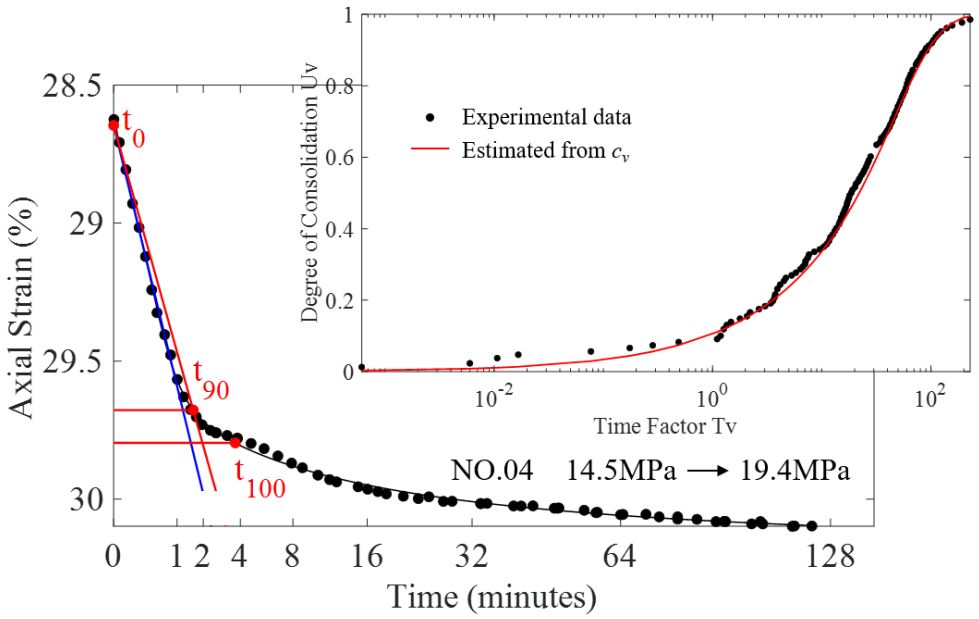

Figure 4-4. An example of the c_v calculation procedure using time-deformation curve by Taylor method (1948). Inset: Evaluation of the calculated c_v by comparing the time factor-consolidation degree curve from experimental data with that estimated from c_v value.

In this study, the σ'_{pc} estimates from the modified Casagrande method (McNulty et al., 1978) and the Becker method (1987) are quite similar (Figure 4-5). The σ'_{pc} values generally increase with depth and several lower values than σ'_{vh} are revealed (NO.04-06, NO.14, NO.17). The consolidation state of sediments is typically evaluated by the overconsolidation ratio (*OCR*) which is defined as the ratio of σ'_{pc} to the in situ vertical effective stress (σ'_v) (e.g., Knappett & Craig, 2012). *OCR* = 1 indicates normally consolidated sediments, while *OCR* > 1 indicates overconsolidated sediments (e.g., Knappett & Craig, 2012). Although σ'_v is unknown, it should be similar to σ'_{vh} or less than σ'_{vh} in case of overpressure at a uniaxial burial stress regime (e.g., Kitajima & Saffer, 2014; Screaton et al., 2002). We therefore compared σ'_{pc} with σ'_{vh} and found most σ'_{pc} values are larger than σ'_{vh} values at the same depth (Figure 4-5). These samples are inferred to be overconsolidated, which might result from secondary consolidation and diagenesis (e.g., Bjerrum, 1973; Locat & Lefebvre, 1986). This is supported by the observed authigenic clays and carbonates as well as elevated $^{87}Sr/^{86}Sr$ ratio in pore fluids (Torres et al., 2020). For the samples with $\sigma'_{pc} < \sigma'_{vh}$, we concluded that the sediments are overpressured.

Also, we defined the in situ permeability by matching the applied stress with σ'_v (see section 3.3 for σ'_v calculation). The permeability generally decreases with depth and a decrease by nearly

three orders of magnitude is observed (Figure 4-5). The samples with $\sigma'_{pc} < \sigma'_{vh}$ have relatively low permeability ($k < 1.5\times10^{-17}$ m^2), which is consistent with the inference of overpressure. For the sand sample at 337 mbsf (NO.05), the corresponding permeability is increased by one order of magnitude ($k = 2.0\times10^{-16}$ m^2). This implies that it might be isolated by low-permeability mud, which inhibits the drainage of pore fluids and causes the excess pore pressure.

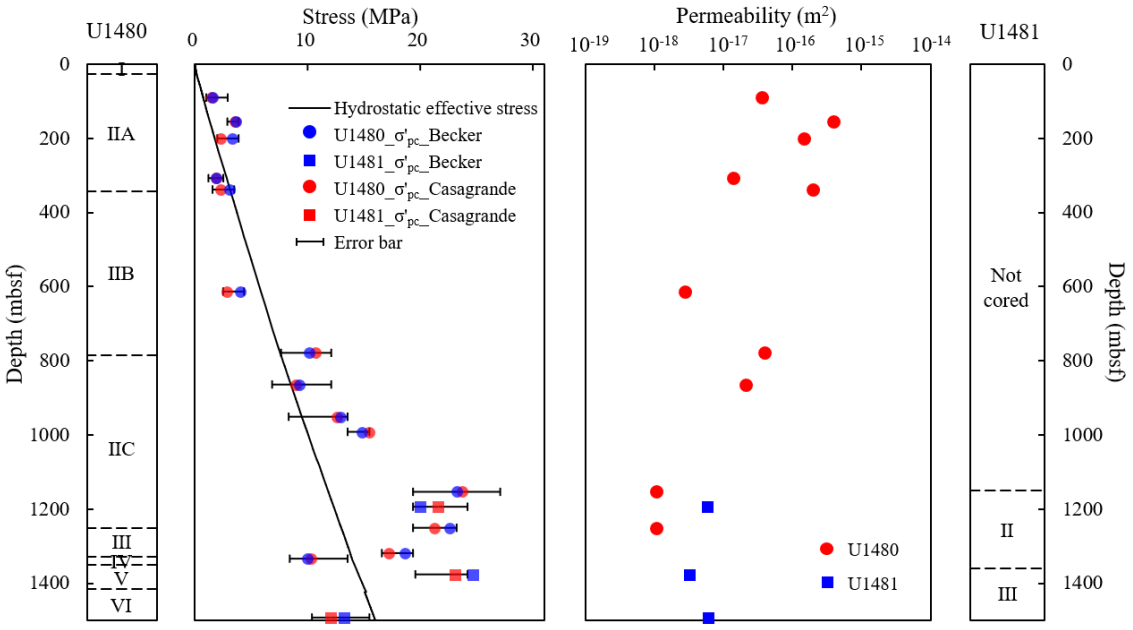

Figure 4-5. Estimated preconsolidation stress and in situ permeability at IODP Sites U1480 and U1481.

4.3.3 Estimates of Pore Pressure

Based on the Terzaghi's effective stress theory and the definition of *OCR*, the pore pressure *P* can be estimated after Zhang et al. (2021) by:

$$P = \sigma_v - \frac{\sigma'_{pc}}{OCR} \tag{4-2}$$

To calculate the *OCR* values, we assumed $\sigma'_v = \sigma'_{vh}$ in Units IIA and IIB considering that (1) the porosity decreases continuously with depth (Figure 4-2), (2) the lithology is dominated by sand/sandstone, and (3) most of the linear sedimentation rate (LSR) is relatively low (McNeill et al., 2017b). However, the data with $\sigma'_{pc} < \sigma'_{vh}$ (NO.04-06) were excluded since the assumption ($\sigma'_v = \sigma'_{vh}$) does not apply. In contrast, although the LSR at 81-206 mbsf is up to 362 m/Myr, the data were included because (1) the samples are mainly sand, and (2) the subsequent loading rate (LSR above this horizon) is relatively low (McNeill et al., 2017b). Based on the estimated *OCR*

values, we acquired an average *OCR* = 1.86 and calculated the pore pressure at Sites U1480 and U1481 by equation (4-2).

For an uniaxial burial stress regime, the porosity/void ratio (*e*) is mainly governed by $\sigma_v^{'}$ and hence porosity/void ratio is widely used to estimate pore pressure (e.g., Screaton et al., 2002). Many equations for pore pressure prediction using porosity/void ratio or other equivalent parameters have been proposed (e.g., Eaton, 1972; Flemings & Saffer, 2018; Rubey & Hubbert, 1959). In this study, we used a method building on the relationship between the specific volume (1+*e*) and $\sigma_v^{'}$ to derive pore pressure (Butterfield, 1979). This method considers the compressibility variation under different stress levels and has been successfully applied to a large stress range (e.g., Long et al., 2011). The equation is expressed in a form as:

$$\ln(v) = \lambda \cdot \ln(\sigma_v^{'}) + \ln(v_0) \tag{4-3}$$

where v is the specific volume, v_0 is the specific volume under an effective stress of unity and λ is the slope on the ln(v)-ln($\sigma_v^{'}$) plot (Figure 4-6). We used our consolidation data from the virgin compression phase to derive the empirical parameters in equation (4-3). However, the data points under relatively low effective stress (< 3 MPa) are absent because the stress in virgin compression is high. To determine an equation that can be applied to the whole depth range, we included the shipboard MAD data above 200 mbsf. The $\sigma_v^{'}$ was assumed to be equal to $\sigma_{vh}^{'}$, because (1) the sand content is high, (2) the recent LSR is low (McNeill et al., 2017b), and (3) the in situ permeability is relatively high (Figure 4-5). The combination of the consolidation and MAD data yielded a λ = -0.14 and a ln(v_0) = 1.65 (Figure 4-6). This equation can be applied from the seafloor to a depth of 4-5 kmbsf, because the data points cover a stress range of 0-46.5 MPa. With this equation, we estimated the pore pressure at Sites U1480 and U1481 using MAD data.

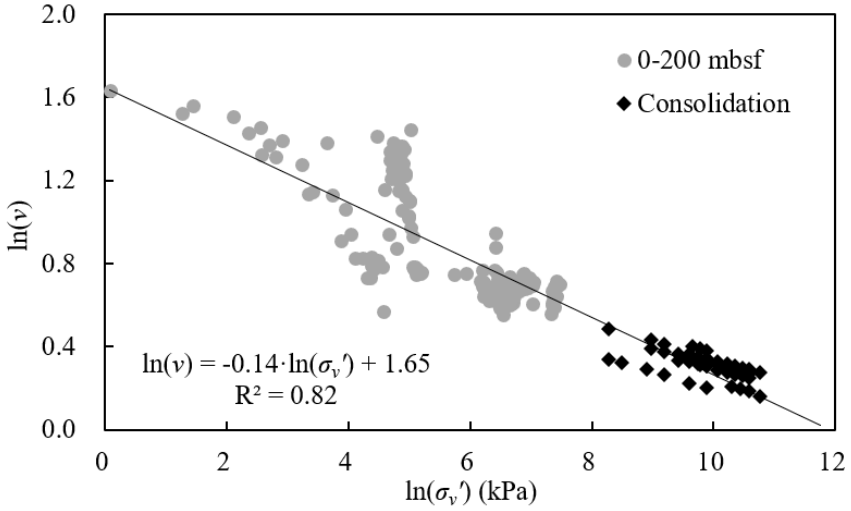

Figure 4-6. The relationship between specific volume and vertical effective stress for

mud/mudstone at IODP Sites U1480 and U1481 derived from MAD measurements at 0-200 mbsf and consolidation data.

Our results show that the pore pressure estimates derived from Casagrande method and Becker method are similar (Figure 4-7, equation (4-2)). The maximum pore pressure difference between these two methods is 0.87 MPa and the difference as a percentage is generally below 6.4%. The error bar is relatively narrow and its width is smaller than 2.8 MPa with one exception of 4.2 MPa at 1153 mbsf. For the convenience of description, only results by the modified Casagrande method are discussed.

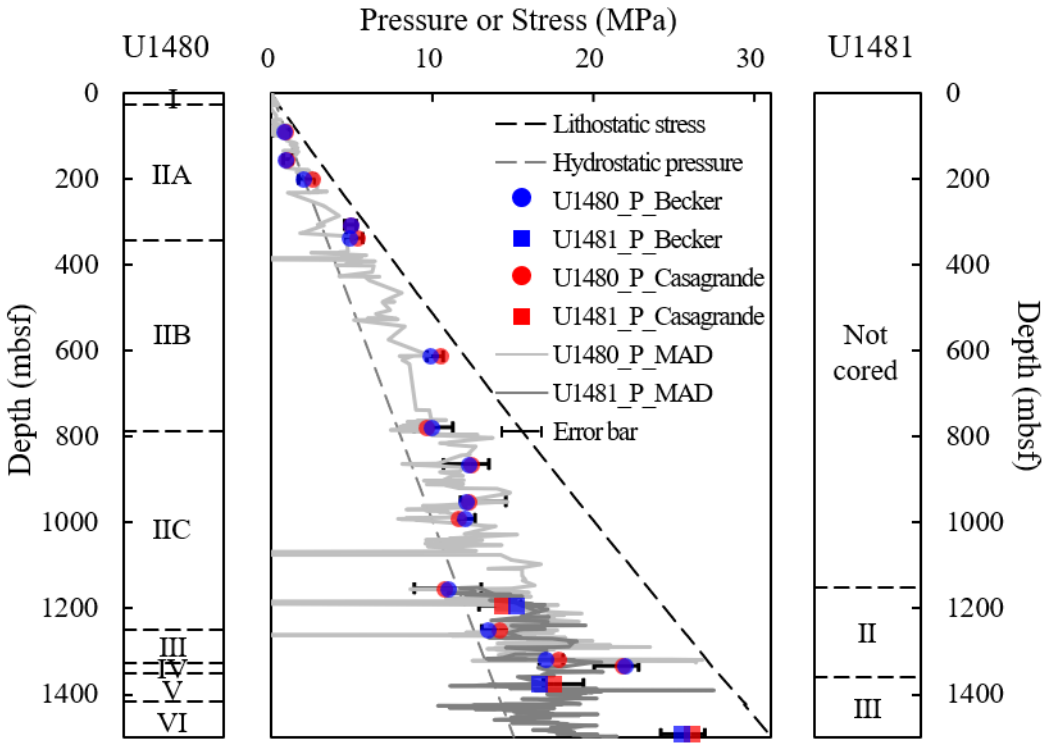

Figure 4-7. Pore pressure estimates derived from consolidation and MAD data at IODP Sites U1480 and U1481.

The experimental pore pressure estimates from Unit IIA show that the upper part of Unit IIA is hydrostatic while the lower portion is overpressured with an excess pore pressure up to 1.9 MPa. The pore pressure results from MAD data are in good agreement with experimental estimates and indicate the excess pore pressure is not continuous. This is consistent with the concept that although the high sand content does not facilitate excess pore pressure generation, high pore pressure can be maintained when the sediment such as the sand sample at 337 mbsf is isolated by low-permeability mud (e.g., Zhang et al., 2019). For the Units IIB and IIC, our experimental data also reveal excess pore pressure in a range of 1.6-4.3 MPa. The pore pressure estimates are consistent with the results from MAD data. Despite fluctuation, the MAD pore pressure estimates

show that overpressured sediment is distributed throughout Units IIB and IIC with an average excess pore pressure of 2.4 MPa.

In contrast to Unit II, our experimental pore pressure data indicate a high average excess pore pressure of 6.9 MPa in Units III and IV. The pore pressure results from MAD data are generally consistent with the experimental estimates. The high pore pressure in Unit III is in agreement with the observed HANP reflection in the seismic profile which is considered as potential candidates for the localization of the décollement (Dean et al., 2010). Geochemistry modeling shows that the transition from opal-A to opal-CT to quartz is nearly completed in Unit III (Hüpers et al., 2017), which explains the distinct higher excess pore pressure relative to Unit II. Considering the lithology in Unit IV is mainly composed of tuffaceous and volcaniclastic sandstone, basaltic flows and volcanic breccia, we suggest that the high pore pressure in Unit IV might be produced by pressure transmission from highly overpressured Unit III.

4.4 Numerical Modeling of Pore Pressure Evolution

4.4.1 Numerical Model and Implementation

To investigate the pore pressure evolution in the horizon of the potential décollement as the sediment approaches the subduction zone, we used a one-dimensional sedimentation-flow model, which accounts for the sedimentation rate and silicate dehydration. Following Gordon and Flemings (1998), the pore pressure evolution is described by:

$$\frac{\partial P}{\partial t} = \frac{1}{S_{t1}} \cdot \frac{\partial}{\partial z}\left[\frac{k}{\mu} \cdot \left(\frac{\partial P}{\partial z} - \rho g\right)\right] + \gamma \cdot \frac{\partial \sigma_v}{\partial t} + \frac{1}{S_{t2}} \cdot \frac{\partial V}{\partial t} \tag{4-4}$$

$$S_{t1} = m_{v1} + \varphi \cdot \beta_f \tag{4-5}$$

$$S_{t2} = m_{v2} + \varphi \cdot \beta_f \tag{4-6}$$

$$\gamma = \frac{m_{v1}}{m_{v1} + \varphi \cdot \beta_f} \tag{4-7}$$

where t is the time, S_t is the storage coefficient, z is the burial depth, k is the vertical permeability, μ is the temperature-dependent viscosity of pore water, ρ is the water density, g is the gravity acceleration, γ is the loading efficiency, $\frac{\partial V}{\partial t}$ is the fluid production rate generated by silicate dehydration, φ is the porosity, m_v is the coefficient of volume compressibility for the formation, and β_f is the coefficient of volume compressibility for the pore water. Because the m_v value for the formation is different in the loading and unloading phases, we included m_{v1} and m_{v2} which represent the coefficients of volume compressibility for the formation in the loading and unloading

phases, respectively. Correspondingly, we had S_{f1} and S_{f2} which represent the storage coefficients for the fluid drainage (loading) and fluid generation (unloading), respectively.

Our numerical model covers a time range of -9.5 Ma before present (onset of Unit II deposition) to 6.4 Myr into the future when a final depth of 5 kmbsf was reached, corresponding to the maximum burial depth of the incoming sediment at the deformation front (McNeill & Henstock, 2014). For the boundary conditions, we assumed a hydrostatic boundary at the seafloor and no fluid flow at the base of the system. In our simulation, we adopted ρ = 1024 kg/m^3 (e.g., Zhang et al., 2021) and $\beta_f = 4.4\times10^{-10}$ Pa^{-1} (e.g., Fetter, 2013). The porosity was governed by the vertical effective stress based on equation (4-3) and a hydrostatic pore pressure was assigned to the sediment at the time of burial. The vertical permeability was derived from the porosity according to the log-linear permeability-porosity relationship established using our consolidation data (Figure 4-8). The temperature dependent viscosity of pore water followed Huyakorn and Pinder (1978) and the temperature was calculated by a thermal gradient of 44.4°C/km (McNeill et al., 2017b). The fluid production rate was the sum of fluid production from opal-A to opal-CT to quartz and clay dehydration with a clay content of 50% to a final burial depth of 5 kmbsf in Hüpers et al. (2017). Based on the definition of the coefficient of volume compressibility, we derived m_{v1} from equation (4-3):

$$m_{v1} = \frac{-\lambda}{\sigma_v^{'} \cdot v} \tag{4-8}$$

Therefore, a pore pressure dependent m_{v1} value was used in our simulation. In contrast, a constant m_{v2} =2×10^{-9} Pa^{-1} averaged from our consolidation data in the unloading phase was utilized. For the sedimentation loading $\frac{\partial \sigma_v}{\partial t}$, we used two constant sediment rates to simplify the calculation. An average sediment rate of 372 m/Myr from -9.5 Ma to the present was assigned to the Nicobar Fan sediment, which fulfils the current burial depth of Unit III reaching ~1327 mbsf. For the subsequent sedimentation, we specified an average sediment rate of 1780 m/Myr until 6.4 Myr after the present to make the burial depth of Unit III reach ~5 kmbsf. These two sedimentation rates are higher but equivalent to the average LSR of 139 m/Myr and 575 m/Myr used by Hüpers et al. (2017), because a high initial porosity of 80% was assumed in our model.

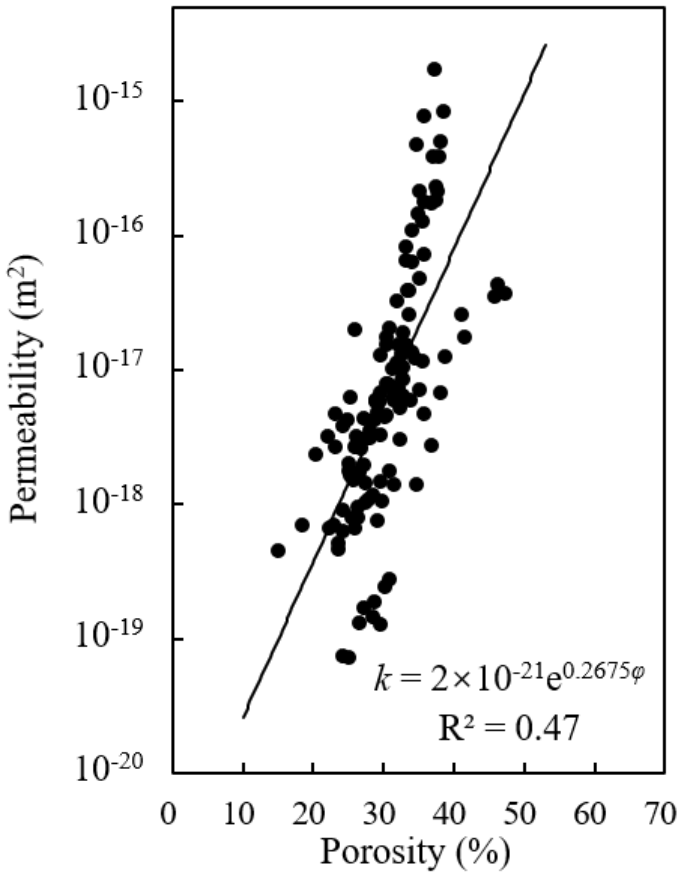

Figure 4-8. The relationship between porosity and permeability at IODP Sites U1480 and U1481 derived from consolidation data.

4.4.2 Modeling Results and Implications

Our modeling results (Figure 4-9) show that the modeled pore pressure estimates are well constrained by the average pore pressure derived from consolidation experiments. The pore pressure in Unit III increases with time continuously and reaches a peak pore pressure ratio (P/σ_v) of 0.96 in 4.18 Myr. The modeled excess pore pressure at the present is 6.0 MPa whereas that at the deformation front is 37.7 MPa. The assigned two high average sedimentation rates lead to constant overpressure generation rates of 1.2 and 5.6 MPa/Myr, respectively. In comparison, the silicate dehydration overpressure rate increases with time and reach a peak rate of 26.4 MPa/Myr at 3.74 Myr, after which the overpressure generation rate decreases continuously. The silicate dehydration overpressure rate is divided into two stages. The first stage (from -8 Ma to the present) is mainly related to the transition from opal-A to opal-CT to quartz, whereas the second phase (from the present to 6.4 Myr) is dominated by clay mineral dehydration (Hüpers et al., 2017). Also, we quantified the overpressure contribution from both rapid sedimentation and silicate dehydration by the integral of overpressure generation rate over the time. For the present state, ~50% of the excess pore pressure is attributed to the silicate dehydration while the other half is caused by the

high sedimentation rate. With the progressive clay dehydration, the silicate dehydration makes an increasing contribution to the overpressure generation. At the deformation front, the overpressure contribution from silicate dehydration increases to ~66%. Correspondingly, the overpressure contribution from rapid sedimentation decreases to ~34%. In comparison with previous studies emphasizing the excess pore pressure driven by silicate dehydration (Geersen et al., 2013; Gulick et al., 2011; Hüpers et al., 2017), our results further suggest an overpressure contribution from high sedimentation rate and provide quantitative constraints. This explains the relatively low but wide-spread excess pore pressure in the Nicobar Fan sediment estimated by both the consolidation and MAD data. Further, the existence of excess pore pressure provides a plausible explanation for the obvious lower decreasing rate of porosity relative to other subduction zones.

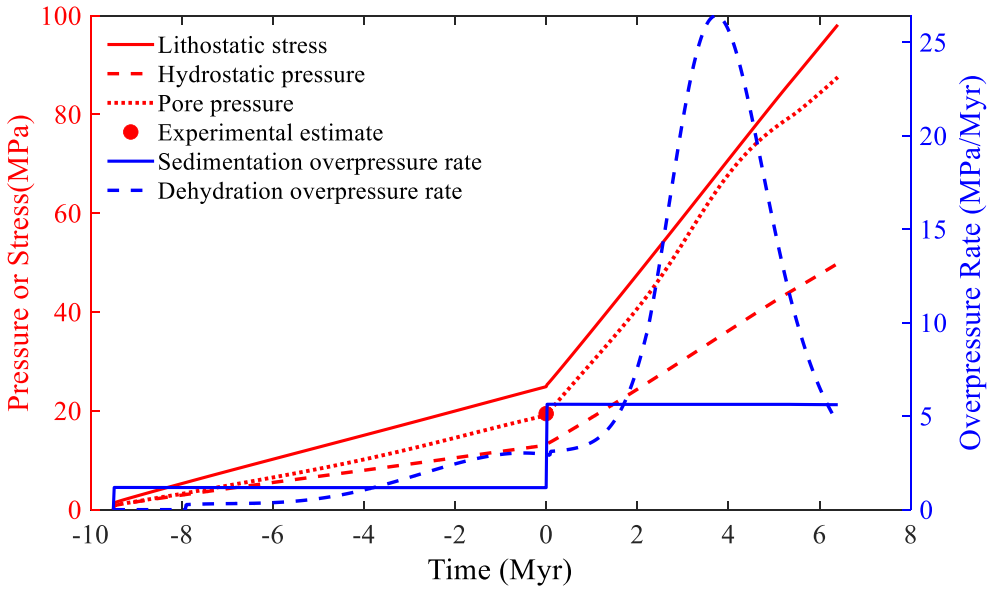

Figure 4-9. Modeled pore pressure evolution and overpressure rate generated by sedimentation and dehydration at IODP Site U1480. Present time is 0 Myr. The experimental estimate (red dot) represents the average pore pressure derived from consolidation data.

Although our numerical model is one-dimensional and simplifies the sedimentary processes and silicate dehydration, the modeled pore pressure estimates support the existence of a low-velocity layer in the seismic profile (Qin & Singh, 2017) which may be the proto-décollement (Dean et al., 2010). In an extensional stress setting, Behrmann (1991) suggested that in a normal faulting regime hydrofracture can occur when the pore pressure ratio reaches 0.7-1. The critical pore pressure ratio depends on the cohesion of sediments. Considering the present pore pressure ratio is larger than 0.7, the sediment in Unit III could be hydrofractured. The hydrofracture increases the permeability of sediments and leads to the updip migration of overpressured fluids. The updip migrated overpressure fluids may lead to further hydrofracture in overlying sediments and create large scale normal faults. This is supported by the frequently observed high angle normal fault in the seismic profile (McNeill et al., 2017b). These normal faults may serve as fluid flow pathways and facilitate

dewatering of overpressured thick sediments. However, high pore pressure is still maintained considering (1) dewatering can be partially compensated by continuous silicate dehydration and (2) the HANP reflector is clearly observed seaward from the deformation front (Dean et al., 2010).

In the North Sumatra accretionary prism, previous studies revealed the uncommon landward-vergent frontal thrusts (e.g., McNeill & Henstock, 2014; Moeremans et al., 2014). The landward vergence of the frontal thrusts was simply interpreted to be related to a low basal shear strength (e.g., Adam et al., 2004) or a thick incoming sediment succession (Moeremans et al., 2014) supported by sandbox experiments with low basal friction showing conjugate thrusts (Seely, 1977). Further analog experiments using a ductile basal layer suggested that the landward vergence is associated with a certain range of strain rates (Gutscher et al., 2001), while Cubas et al. (2016) argued that the sudden decreases of the friction along the megathrust caused by dynamic weakening is responsible for the formation of landward-vergent frontal thrusts through mechanical analysis. In comparison, Zhou et al. (2016) accounted for the lateral friction in sandbox experiments and proposed that both low basal friction and landward-directed lateral friction exerted by the lateral strike-slip faults are the key factors resulting in landward-vergent structures. The landward-vergence of frontal thrust in the North Sumatra seems can be explained by this mechanism. Although strike-slip faults parallel to the subduction direction are not observed, the increased subduction velocity to southeast may induce an additional landward force. Together with the significantly decreased basal friction by high excess pore pressure, the landward-vergent frontal thrusts is likely to form in the accretionary prism and cause large near-trench rupture during earthquakes (e.g., Cubas et al., 2016; Moeremans et al., 2014).

Based on the previously reported seismic profile, the HANP reflector becomes less clear and uncontinuous landward from the trench (Dean et al., 2010), which implies that the décollement is heterogeneous and the pore pressure beneath the outer prism may drop to a low level if sufficient drainage happens. Low pore pressure patches are very likely to exist because the silicate dehydration has been completed before plate subduction (Hüpers et al., 2017) such that the discharged fluids cannot be compensated by the water released from dehydration. Based on our interpretation, the uncontinuous reflector might represent interweaved patches with high and low pore pressures, while the absence of HANP could indicate sufficient dewatering. Given that the negative polarity is observed up to ~20 km landward from the trench (Dean et al., 2010), high pore pressure might be widely distributed. This is supported by the distribution of landward-vergent frontal thrusts (Moeremans et al., 2014). An earlier explanation for the 2004 Sumatra tsunamigenic earthquake mainly focuses on the advanced diagenesis driven by thick sediment which shifts the seismogenic zone and coseismic slip seaward (Geersen et al., 2013; Hüpers et al., 2017). We suggest that the weak décollement mechanism cannot be ruled out. Park et al. (2014) proposed that the tsunamigenic earthquake is related to the different behaviors in unstable and conditionally stable patches. The low pore pressure patches act as unstable regions and initiate earthquakes, whereas the high pore pressure patches are conditionally stable and facilitate the propagation of

coseismic slip when a nearby earthquake is triggered. Although the thickly buried sediment does shift the earthquake nucleation seaward, the near-trench coseismic slip may be enhanced by the high excess pore pressure.

In summary, the thick sediment in the North Sumatra subduction zone enhances the diagenesis (e.g., Geersen et al., 2013) and elevates the pore pressure by rapid burial. The complete silicate dehydration not only alters the frictional behavior of sediments and shifts the seismogenic zone seaward (e.g., Hüpers et al., 2017), but also further weakens the sediments by generating high excess pore pressure. The resulting low basal friction and the landward-directed lateral friction exerted by higher subduction velocity to the southeast lead to the landward-vergent frontal thrusts (Zhou et al., 2016) which is regarded as an important source of shallow slip (e.g., Cubas et al., 2016; Moeremans et al., 2014). Therefore, when an earthquake nucleates in the seaward shifted seismogenic zone, the near-trench weak faults provide little resistance such that the coseismic slip propagates all the way to the trench (Faulkner et al., 2011) and results in tsunami hazard, as seen in the M_w 9.2 2004 Sumatra-Andaman event.

4.5 Conclusions

Based on consolidation experiments and numerical model, mainly hydrostatic to low excess pore pressure is reveled at IODP Sites U1480 and U1481, while a horizon which is considered as potential candidates for the localization of the décollement shows moderate excess pore pressure. The excess pore pressure results from high sedimentation rate and silicate dehydration according to a one-dimensional sedimentation-flow model which accounts for the sedimentation rate and silicate dehydration. Extending landward, the excess pore pressure increases continuously and the dehydration of silicate makes an increasing contribution to the generation of excess pore pressure. The pore pressure in the proto-décollement horizon reaches >90% of the lithostatic stress before plate subduction and thus high excess pore pressure is inferred along the décollement in the North Sumatra subduction zone. Together with the landward-directed lateral friction exerted by higher subduction velocity to the southeast (McNeill & Henstock, 2014), the high excess pore pressure might lead to the landward vergence of frontal thrusts. We further suggest that the high excess pore pressure significantly decreases the resistance along faults which make the coseismic slip propagate all the way to the trench and increases the tsunami size when an earthquake happens. This provides a plausible explanation for the occurrence of the M_w 9.2 2004 Sumatra-Andaman tsunamigenic earthquake.

Supplementary Material

Table S4-1. Details of the whole round samples in this study.

Sample NO.	Site	Hole	Unit	Depth (mbsf)	Lithology
NO01	U1480	E	IIA	89	Mud
NO02	U1480	F	IIA	154	Sand
NO03	U1480	F	IIA	199	Sandy mud
NO04	U1480	F	IIA	306	Mud
NO05	U1480	F	IIA	337	Find sand
NO06	U1480	F	IIB	612	Mud
NO07	U1480	G	IIB	778	Mud
NO08	U1480	G	IIC	863	Mud
NO09	U1480	G	IIC	950	Mud
NO10	U1480	G	IIC	991	Mud
NO11	U1480	G	IIC	1153	Mud
NO12	U1480	G	IIC	1250	Mud
NO13	U1480	G	IIIB	1318	Tuffaceous clay
NO14	U1480	G	IV	1333	Tuffaceous sand
NO15	U1481	A	II	1193	Mud
NO16	U1481	A	III	1376	Mud
NO17	U1481	A	III	1492	Mud

Table S4-2. Results of the consolidation experiments

Sample NO.	Depth (mbsf)	σ_v (Pa)	P_{hy} (Pa)	σ'_{hy} (Pa)	σ'_{pc_Casa} (Pa)	σ'_{pc_Becker} (Pa)	σ'_{pc_min} (Pa)	σ'_{pc_max} (Pa)
NO01	89	1624277	894446	729831	1461015	1561394	1005653	2904042
NO02	154	2814542	1522487	1292055	3554604	3638650	2874075	3872057
NO03	199	3758659	2006275	1752383	2240337	3322947	1980013	3872057
NO04	306	5901176	3077019	2824158	1838637	1872353	1192317	2516837
NO05	337	6498960	3386921	3112039	2273148	3097837	1558809	3484851
NO06	612	12001423	6151225	5850198	2808823	3990428	2496210	4356064
NO07	778	15371351	7812841	7558511	10707351	10098685	7647218	12100177
NO08	863	17183760	8672128	8511632	8943623	9267456	6849631	12100177
NO09	950	19026861	9544775	9482086	12634239	12935057	8318359	13552198
NO10	991	19921797	9956136	9965661	15481721	14826569	13552198	15488226
NO11	1153	23428470	11582694	11845776	23703635	23278628	19360283	27104396
NO12	1250	25544552	12558106	12986447	21266989	22586731	19360283	23232339
NO13	1318	27031088	13245415	13785673	17214084	18639677	17834416	19360283
NO14	1333	27327165	13391476	13935690	10310637	10008074	8413896	13552198
NO15	1193	25888969	11974803	13914165	21593658	19979859	19360283	24200353
NO16	1376	29890425	13805926	16084499	23078538	24705886	19569255	24200353
NO17	1492	32503745	14981550	17522195	12008817	13195461	10384855	15488226

Chapter 5: Pore Pressure Prediction in the North Hikurangi Subduction Zone: Implications for Slow Slip Events

Junli Zhang, Matt Ikari, Andre Hüpers, and Achim Kopf

MARUM—Center for Marine Environmental Sciences and Faculty of Geosciences, University of Bremen, Bremen, Germany

Corresponding author: Junli Zhang (jzhang@marum.de)

Abstract

Slow slip events (SSEs) are one type of slip in the full spectrum of fault-slip behaviors and remain incompletely understood. In this study, we estimated the pore pressure in the Northern Hikurangi subduction zone and investigated the effects of pore pressure on SSEs. Consolidation experiments on samples from IODP Site U1520 show that the sediment in trench-wedge facies is underconsolidated whereas that in pelagic and volcaniclastic facies is overconsolidated. Lithology, biostratigraphy and seismic reflection data suggest that the trench-wedge facies are stratigraphically equivalent to the horizon where the active Pāpaku splay fault occurs at IODP Site U1518. Based on the consolidation data on trench-wedge facies, a pore pressure prediction equation for Site U1518 is derived using critical state soil mechanics. Pore pressure 77% of lithostatic stress is revealed at the top of the Pāpaku fault, whereas the pore pressure at the bottom increases to 93% of lithostatic stress. Previous studies have shown that SSEs in the North Hikurangi subduction zone may propagate to a depth of < 2 km below seafloor (kmbsf). Therefore, SSEs at 2 kmbsf are simulated under above pore pressure conditions according to the rate-and-state friction theory. The modeling results are comparable to the natural SSEs and indicate that high pore pressure decreases the recurrence interval of SSEs.

5.1 Introduction

Slow slip events (SSEs) are one type of slip in the full spectrum of fault-slip behaviors, where the fault slip occurs episodically with too low velocity to produce earthquakes (Wallace, 2020). It has attracted great attention due to its close relationship with ordinary earthquakes. For example, Koulali et al. (2017) show that SSEs can trigger large earthquakes by increasing static stress on the fault plane. In turn, SSEs can also be triggered by distant large earthquakes, because earthquakes may cause static stress increases (e.g., Wallace et al., 2018) or induce positive stress perturbation through passing seismic waves (e.g., Wallace et al., 2017).

Although the mechanism governing SSEs is not completely understood, it is accepted that SSEs may be attributed to the transitional stability of faults (e.g., Saffer & Wallace, 2015). High pore pressure is a potential factor causing the transition, because highly overpressured sediments is conditionally stable (Scholz, 1998) and is considered favorable for silent slip (e.g., Kodaira et al.,

2004). On the other hand, laboratory friction experiments reveal contrasting frictional properties at different orders of magnitude of velocity, where weak clay-rich fault material behaves as velocity-strengthening at high sliding velocity and velocity-weakening at low sliding velocity, respectively (Ikari & Kopf, 2017). The velocity when the velocity-weakening frictional behavior transitions to velocity-strengthening is referred as the cut-off velocity (e.g., Shibazaki & Iio, 2003). This transitional friction behavior is favorable for the nucleation of unstable slip at low sliding velocity, but suppresses the slip propagation at higher velocity (e.g., Saito et al., 2013), which has been considered as one mechanism of SSEs (e.g., Saffer & Wallace, 2015). Based on this concept, Im et al. (2020) conduct numerical simulations and reproduce natural SSEs. They suggest that SSEs can be explained by the transitional frictional behavior at different velocities without requiring high pore pressure (Im et al., 2020).

However, although a variety of geological environments can host SSEs (e.g., Wallace & Beavan, 2010; Wallace, 2020), one common characteristic is that SSEs mostly, if not all, occur in highly overpressured regions (Saffer & Wallace, 2015). Therefore, pore pressure is inferred to have an important impact on SSEs. To understand the effects of pore pressure on SSEs, we sampled the incoming sediments in the North Hikurangi subduction zone where shallow SSEs are well documented (Wallace et al., 2016). Through uniaxial consolidation experiments and well-established pore pressure prediction equation, we estimated the pore pressure at IODP Sites U1520 and U1518. Under the acquired pore pressure conditions, we simulated the shallow SSEs in the North Hikurangi subduction zone and investigated the effects of pore pressure on SSEs.

5.2 Geological Setting

The Hikurangi subduction zone is located at the plate edge where the Pacific Plate is subducting westward beneath the North Island of New Zealand (Figure 5-1) with along-strike variations in subduction velocity from ~2 cm/year in the south to ~6 cm/year at the northern margin (Wallace et al., 2004). It hosts the best-documented slow slip events (SSEs) with a variety range of size, duration, recurrence interval and occurrence depth (Wallace et al., 2020). SSEs in the North Hikurangi subduction zone may propagate to a depth of < 2 km below seafloor (kmbsf), which provide an ideal opportunity to investigate the shallow SSEs (Wallace et al., 2016; Saffer et al., 2017). Therefore, International Ocean Discovery Program (IODP) Expedition 372/375 recovered the sediment at Sites U1518, U1519, U1520 and U1526, and installed borehole observatories in the Pāpaku fault which might host SSEs (Saffer et al., 2019a).

Site U1520 is ~16 km seaward of the deformation front and six lithologic units were identified (Barnes et al., 2019): Units I-III are trench wedge facies and mainly composed of hemiplegic mud with silt and sand interbeds; Unit IV is pelagic facies and consists of marl dominated upper subunits and calcareous mudstone and chalk dominated lower subunits; Unit V is volcaniclastic facies and the volcaniclastic conglomerate is heavily altered; Unit VI has mixed lithologies and is dominated by volcaniclastic conglomerate and siliceous mudstone. Among them, Unit II is

interpreted to correspond to the distal edge of the Ruatoria debris avalanche based on seismic profile data (Barnes et al., 2019). In comparison, Site U1518 locates in the frontal accretionary prism, ~6.5 km landward of the trench (Saffer et al., 2019a). It penetrated the Pāpaku fault and three lithologic units were recognized (Saffer et al., 2019a). All the three units have similar lithologies including silty clay and mud with thin interbedded silt to silty sand (Saffer et al., 2019b). Unit I is correspondent to the hanging wall of the Pāpaku fault while Unit III represents the footwall (Saffer et al., 2019b). Unit II was considered as the main fault zone and both brittle and ductile deformation were observed (Fagereng et al., 2019).

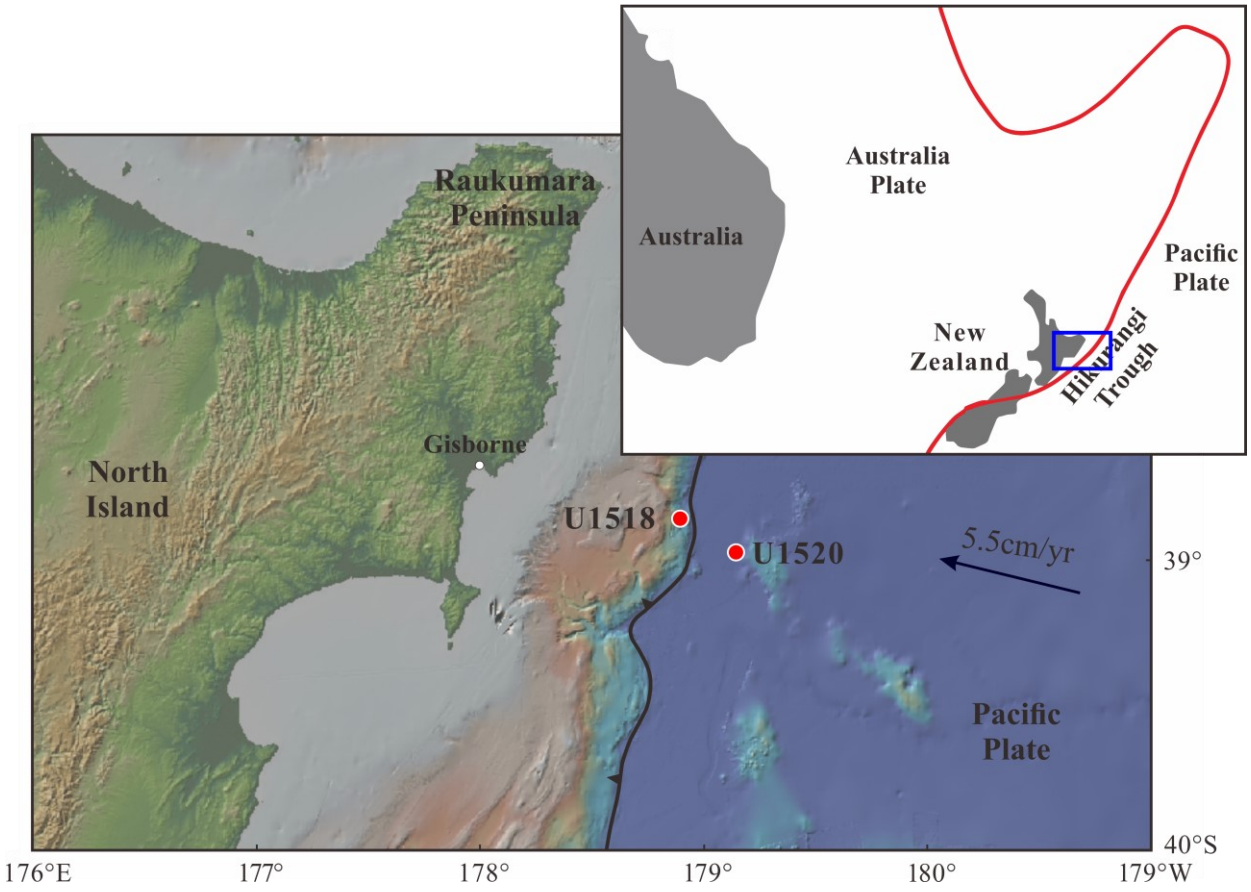

Figure 5-1. Geological setting of the North Hikurangi subduction zone and the locations of IODP Sites U1520 and U1518. Figure made with GeoMapApp (www.geomapapp.org; Ryan et al., 2009). Inset is modified from Wallace (2020).

The moisture and density (MAD) data at Site U1520 show that the porosity decreases rapidly from ~70% to 40-50% in Unit I, after which the porosity remains almost constant until reaching the top of Unit IV (Figure 5-2). Then the porosity decreases from ~50% at 590 meters below seafloor (mbsf) to ~30% at 720 mbsf, followed by a general increase to ~60% at 1000 mbsf despite considerable scatter. In contrast, the porosity profile of Site U1518 shows an obvious decrease from ~70% at seafloor to ~40% at 100 mbsf. Then the porosity only fluctuates slightly to the bottom of the borehole and two small spikes are recognizable at the Unit IA/IB and Unit II/III

boundaries. The broad nearly constant porosity at both Sites U1518 and U1520 is indicative of excess pore pressure.

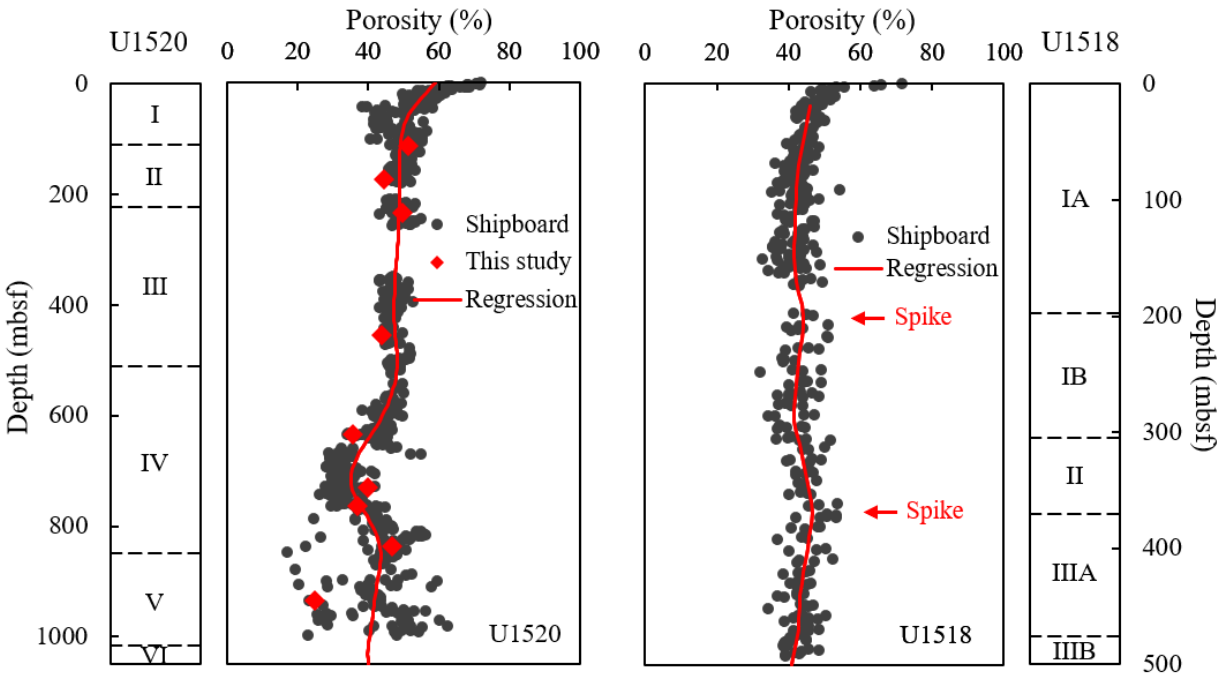

Figure 5-2. Depth profile of porosity at IODP Sites U1520 and U1518 after Saffer et al. (2019a). Roman numerals indicate lithologic units.

5.3 Pore Pressure Estimation and Analysis

5.3.1 Sample Material and Consolidation Experiment

Preconsolidation stress (σ'_{pc}) represents the maximum vertical effective stress that the sediment has experienced (Casagrande, 1936) and can be employed to infer pore pressure reliably (e.g., Saffer, 2003; Dugan & Germaine, 2008; Zhang et al., 2021). In this study, we conducted consolidation experiments on whole round samples collected from IODP Site U1520 to derive the preconsolidation stress and pore pressure. Nine samples are included with four mud/mudstone from Units I-III, three marl/chalk from Unit IV and two volcaniclastic conglomerate from Unit V (Table S5-1). All the samples were sealed and stored in the core liner at 4 °C to maintain the natural water content after recovery.

The samples were hand-trimmed into cylinders with a constant diameter of 25.4 mm and a height of ~10 mm and were tested using a uniaxial incremental loading oedometer in accordance with ASTM D2435/D2435M-11 (ASTM International, 2011). During the consolidation experiments, we kept the samples saturated with artificial seawater (35‰) and applied regularly increased load on the samples. The load was initially doubled, and then smaller increments were used when the

load approached σ'_{pc}, so that σ'_{pc} can be determined more precisely (e.g., Brumund et al., 1976). Considering σ'_{pc} was unknown before the test, we calculated the hydrostatic vertical effective stress (σ'_{vh}) by subtracting the hydrostatic pore pressure (P_{hy}) from the lithostatic stress (σ_v) and used σ'_{vh} as a reference. The lithostatic stress was computed by integrating the bulk density profile acquired from MAD data. Each load in the test was maintained for 24 hours to dissipate the excess pore pressure completely. For each sample, the change of the sample height under each load was recorded continuously throughout the experiment.

5.3.2 Evaluation of Consolidation Behavior

The consolidation behavior of the sediment is typically evaluated in semi-logarithmic stress-strain plot (Figure 5-3). In the stress-strain plot, the loading curve is divided into two parts by a yield point which is normally interpreted as σ'_{pc} (Casagrande, 1936). The loading curve before σ'_{pc} represents the elastic recompression phase, whereas after σ'_{pc} deformation is elasto-plastic and called virgin consolidation (e.g., Knappett & Craig, 2012). In this study, we estimated σ'_{pc} by a modification of the widely used Casagrande method (McNulty et al., 1978) and the Becker method (1987). To evaluate the uncertainty of σ'_{pc} estimates, we also determined the maximum and minimum σ'_{pc} values following the same approach in section 4.3.2. The laboratory data are shown in the supplementary material (Table S5-2).

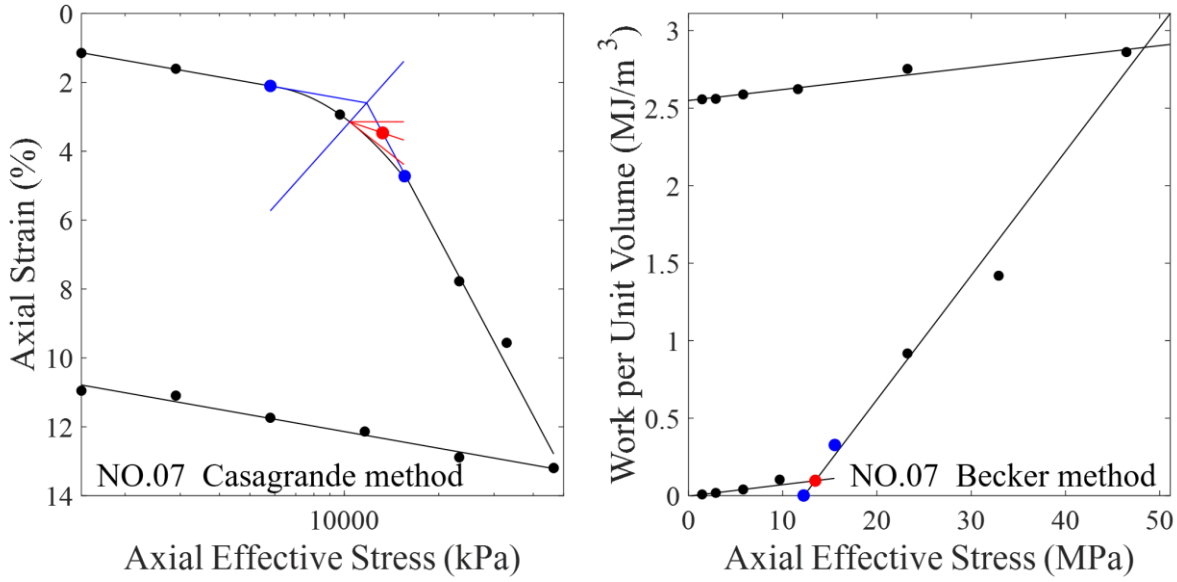

Figure 5-3. An example of the preconsolidation stress estimates based on the modification of the widely used Casagrande method (McNulty et al., 1978) and the Becker method (1987). Red dots

mark the estimated preconsolidation stress. Blue dots mark the minimum and maximum possible preconsolidation stress.

In this study, the σ'_{pc} estimates from the modified Casagrande method (McNulty et al., 1978) and the Becker method (1987) are similar (Figure 5-4). The σ'_{pc} values generally increase with depth and contrasting consolidation state is revealed for Units I-III and Units IV-V. The consolidation state of sediments is typically evaluated by the overconsolidation ratio (OCR) which is defined as the ratio of σ'_{pc} to the in situ vertical effective stress σ'_{v} (e.g., Knappett & Craig, 2012). OCR = 1 indicates normally consolidated sediments, while OCR > 1 indicates overconsolidated sediments (e.g., Knappett & Craig, 2012). However, as σ'_{v} is unknown, we calculated OCR' by the ratio of σ'_{pc} to σ'_{vh}. Many authors denoted this value as OCR directly (e.g., Saffer, 2003; Kitajima & Saffer, 2014). At a uniaxial burial stress regime, σ'_{v} is normally similar to σ'_{vh} or less than σ'_{vh} in case of overpressure (e.g., Kitajima & Saffer, 2014; Screaton et al., 2002). Therefore, the overconsolidated sediment exhibits OCR' > 1 whereas the overpressured sediment shows OCR' < 1.

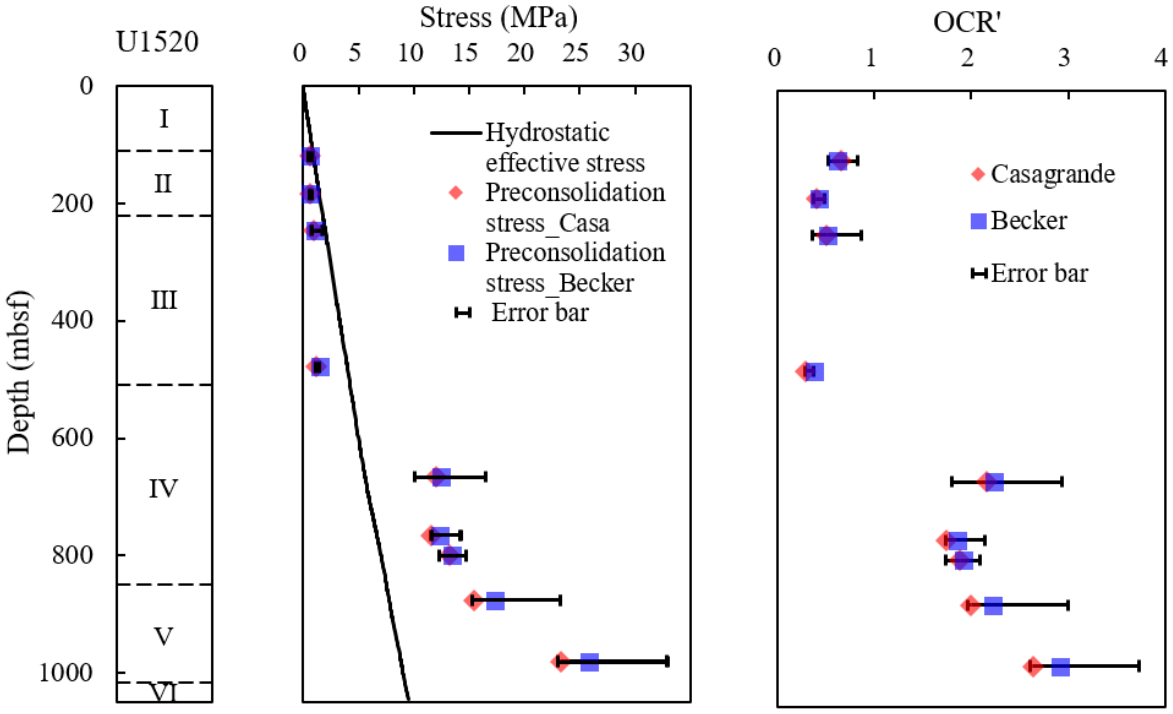

Figure 5-4. Estimated preconsolidation stress and OCR' at IODP Site U1520. Hydrostatic vertical effective stress is plotted for reference.

The σ'_{pc} values of samples recovered from Units I-III are lower than σ'_{vh} values at the same depth and OCR' ranges between 0.28 and 0.65 (Figure 5-4), indicating the sediment is overpressured.

The excess pore pressure is attributed to the high sedimentation rate up to ~1000 m/Ma in Units I-III (Barnes et al., 2019), which inhibits the drainage of pore fluid. This is supported by the nearly constant porosity at corresponding depth (Figure 5-2). In contrast, the samples from Units IV-V are characterized by $\sigma'_{pc} > \sigma'_{vh}$ and the OCR' values are in range of 1.74 - 2.64, showing the sediment is overconsolidated (Figure 5-4). Overconsolidation is commonly the result of ageing/creep, cementation or erosion processes (e.g., Bjerrum, 1973; Locat & Lefebvre, 1986). Lithological description shows that cements are common in Units IV-V (Barnes et al., 2019). Therefore, cementation in Units IV-V may play an important role in strengthening the grain skeleton and preventing the pore space from collapse with increasing overburden. This explains the higher porosity values of 40%-60% at 1000 mbsf compared to other incoming sediments to subduction zones such as Nankai Trough (e.g., Henry et al., 2012a, 2012b; Saito et al., 2010a, 2010b) and North Sumatra (McNeill et al., 2017a).

5.3.3 Pore Pressure Estimates at Site U1520

Based on the Terzaghi's effective stress theory and the definition of OCR, the pore pressure *P* can be estimated after Zhang et al. (2021) by:

$$P = \sigma_v - \frac{\sigma'_{pc}}{\mathrm{OCR}} \tag{5-1}$$

However, accurate OCR is difficult to obtained. For the sediment from Units I-III, we assumed OCR = 1 considering that (1) planktonic foraminifers and calcareous nannofossils represent Holocene age at the seafloor to Pleistocene age at 537 mbsf and thus the ageing/creep effects should be minor, and (2) cements and erosion are uncommon in Units I-III (Barnes et al., 2019). For the sediment from Units IV-V, OCR = 1 does not apply due to strong cementation. We therefore combined equation (5-1) with porosity/void ratio-based pore pressure prediction approach to estimate OCR and pore pressure.

Porosity/void ratio-based approach for pore pressure prediction relies on establishment of an empirical relationship between porosity/void ratio and effective stress. The relationship between void ratio (*e*) and σ'_v is expressed in a form as (e.g., Flemings & Saffer, 2018):

$$e = \lambda \cdot \ln(\sigma'_v) + e_0 \tag{5-2}$$

where e_0 is the void ratio under an effective stress of unity and λ is the slope on the *e*-ln(σ'_v) plot (Figure 5-5). The empirical parameters in equation (5-2) were determined using our consolidation data from the virgin compression phase. Our results show that sediments from different units have different empirical parameters (Figure 5-5). We therefore established the *e*-ln(σ'_v) relationship separately for different units. In addition, the two volcaniclastic conglomerate samples from Unit V also show contrasting *e*-ln(σ'_v) relationships. We suggest the relationship acquired from Sample

NO.08 represents Unit V because the NO.08 porosity falls in the general porosity variation trend while the porosity from NO.09 deviates from the trend obviously (Figure 5-2).

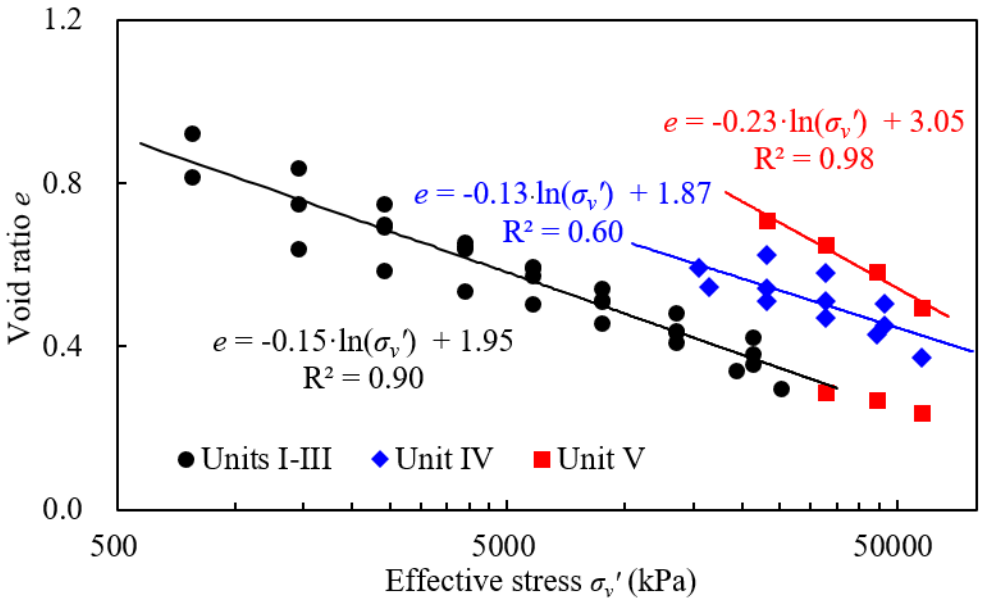

Figure 5-5. The relationship between void ratio and effective stress for sediments at IODP Site U1520 derived from consolidation data.

For the sediment from Units I-III, $\sigma_v^{'}$ and thus pore pressure can be directly estimated by equation (5-2). But for overconsolidated sediment such as from Units IV-V, the e-ln($\sigma_v^{'}$) relationship is shifted towards lower void ratio, which has to be accounted for when estimating pore pressure. Assuming a constant λ, the offset e_d can be estimated by (see section 3.3.3 for details):

$$e_d = \lambda \ln(\mathrm{OCR}) \tag{5-3}$$

Therefore pore pressure for the sediment from Units IV-V can be computed by:

$$e = \lambda \cdot \ln(\sigma_v - P) + e_0 + e_d \tag{5-4}$$

where $e_0 + e_d$ is equivalent to the void ratio under an effective stress of unity for overconsolidated sediments. We further calculated the average depth profile of porosity using regression analysis (Figure 5-2) considering the porosity at Site U1520 is scattered. We then substituted OCRs ranging from 1 to 5 into equations (5-1) and (5-4) to derive the pore pressure and determined the possible OCR for samples from Unit IV when the pore pressure difference is small. The results show that OCR values in Unit IV range from 2.5 to 3.5. However, we suggest that the maximum OCR value in Unit IV could be larger than 3.5, since our discrete samples do not capture where the diagenetic effect is most intense. High Sr concentrations in a range of 1100 to 1300 μM are observed at 600-770 mbsf, indicating strong carbonate recrystallization in Unit IV (Barnes et al., 2019). The most intense carbonate recrystallization is expected at ~720 mbsf where a peak concentration of Ca and

a concave in the Mg concentration profile are visible (Barnes et al., 2019). We therefore assumed hydrostatic pressure and obtained OCR = 4 at ~720 mbsf. By interpolating, we obtained OCR values throughout Unit IV and estimated the pore pressure with equation (5-4). In contrast, substituting OCR = 1-5 into equations (5-1) and (5-4) yielded OCR = 4 for the two samples from Unit V. We therefore employed OCR = 4 to estimate the pore pressure in Unit V with equation (5-4).

Our results show that the pore pressure estimates at Site U1520 derived from Casagrande method and Becker method are similar (equation (5-1), Figure 5-6). The maximum pore pressure difference between these two methods is 0.63 MPa and the difference as a percentage is below 4.9%. The error bar is narrow and its maximum width is 2.5 MPa. For the convenience of description, only results by the modified Casagrande method are discussed.

The experimental pore pressure estimates show that the sediment from Unit I-III is overpressured with pore pressure ratios (P/σ_v) ranging from 0.72 to 0.87. The pore pressure results from MAD data are in good agreement with experimental estimates and indicate the excess pore pressure is continuous throughout Units I-III (Figure 5-6), which is consistent with the high sedimentation rate in Units I-III (Barnes et al., 2019). Based on the pore pressure estimates from MAD data, the excess pore pressure decreases gradually at the top of Unit IV. The experimental pore pressure ratio in Units IV-V is in a range of 0.65-0.77, obviously lower than Units I-III.

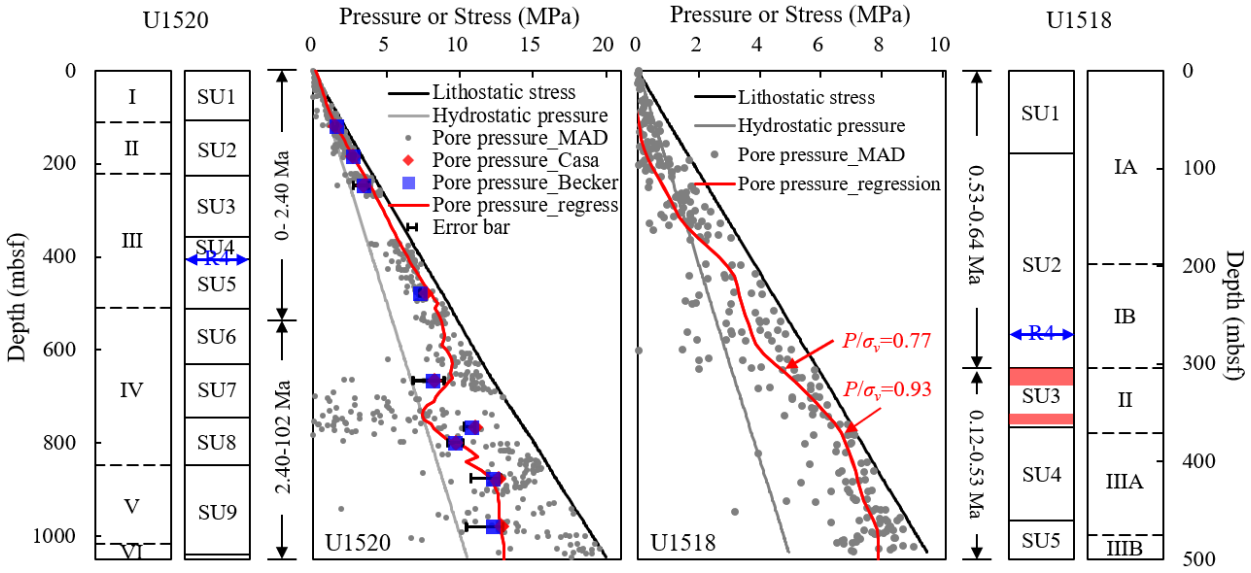

Figure 5-6. Pore pressure estimates derived from consolidation and MAD data at IODP Sites U1520 and U1518. Red thick bars mark the shallow portion of Pāpaku fault which may host SSEs (Fagereng et al., 2019). Red arrows mark the top and bottom of the Pāpaku fault zone at IODP Site U1518 (Saffer et al., 2019b). Blue double arrows mark the Reflector R4 interpreted from seismic profiles (Barnes et al., 2020). Seismic units (SU) and geological time are from Saffer et al. (2019b) and Barnes et al. (2019).

5.3.4 Pore Pressure Estimates at Site U1518

We also estimated the pore pressure at Site U1518 with MAD data. The e-ln($\sigma_v^{'}$) relationship acquired from Units I-III at Site U1520 can be applied to Site U1518, because (1) Planktonic foraminifers and calcareous nannofossils indicate both Units I-III at Site U1520 and all the recovered sediment at Site U1518 represent Quaternary age (Saffer et al., 2019b; Barnes et al., 2019); and (2) a continuous Reflector R4 (Figure 5-6) can be traced between Sites U1520 and U1518 from seismic reflection data (Barnes et al., 2020), which indicates that the oldest Seismic Unit (SU) 2 at Site U1518 might correspond to SU4 (in Unit III) at Site U1520.

However due to the lateral tectonic compaction, the stress orientation in frontal accretionary prism is different from that before entering subduction zones (e.g., Moore & Tobin, 1997; Tsuji et al., 2008), which would cause an underestimation of the pore pressure using equation (5-2) directly. Building on critical state soil mechanics, Flemings and Saffer (2018) recently provided the pathway to predict the pore pressure in both accretionary prism and underthrust sediments. Assuming the accretionary prism is in a state of Coulomb failure, the pore pressure can be estimated by:

$$P = \sigma_v - (1\text{-}\sin\phi) \cdot \exp(\frac{e_{\lambda\tau} - e}{\lambda}) \tag{5-5}$$

where ϕ is the friction angle of sediment material and $e_{\lambda\tau}$ is the void ratio under an effective stress of unity at Coulomb failure (see Flemings and Saffer (2018) for details). $e_{\lambda\tau}$ can be derived from ϕ, λ and e_0 based on the Modified Cam Clay (MCC) critical state model under plane stain conditions (Roscoe & Burland, 1968). Friction experiments reveal a friction coefficient of ~0.44 for shallow sediments (194-213.48 mbsf) in the North Hikurangi (Rabinowitz et al., 2018; Ikari et al., 2020), corresponding to a friction angle of 24°. We therefore employed ϕ = 24°, λ = -0.15 and e_0 =1.95 to calculate $e_{\lambda\tau}$ and estimated the pore pressure at Site U1518 using equation (5-5). Similar with Site U1520, we also established the average depth profile of porosity at Site U1518 using regression analysis (Figure 5-2) and obtained the average pore pressure variation trend (Figure 5-6).

Our results show that the pore pressure at Site U1518 generally increases with depth (Figure 5-6). The estimated pore pressure is lower than the hydrostatic pore pressure within 160 mbsf, but increases rapidly at the bottom of Unit IA and remains relatively high in Unit IB with pore pressure ratios of 0.71-0.77. However, compared with Site U1520 where no lateral tectonic compaction is expected, this pore pressure is still low. This is because, as the hanging wall of the Pāpaku fault, Unit I has been buried in a larger depth and has relatively lower porosity. The pore pressure in Unit I might be underpredicted and our pore pressure estimates represent a lower bound. The pore pressure in Unit II increases continuously and the pore pressure ratio reaches the maximum of 0.93 at the bottom of Unit II. The obvious different pore pressures between the top and bottom of Unit

II (Pāpaku fault) is consistent with the inference that the contrasting properties in the Pāpaku fault zone lead to the mixed deformation behavior (Fagereng et al., 2019). We suggest that the different pore pressures may result from pore fluid drainage during fault slip and reflect the progressive consolidation in the fault zone. In Unit III, the pore pressure continues to increase with a smaller gradient and the pore pressure ratio decreases from 0.93 to 0.81. The higher pore pressure ratio beneath the fault zone implies that the Pāpaku fault may serve as a fluid barrier. Based on the pore pressure results at Sites U1518 and U1520, high excess pore pressure is inferred to be widespread in the North Hikurangi frontal accretionary prism, which explains the occurrence of nearby tsunamigenic earthquake in 1947 (Doser & Webb 2003).

5.4 Numerical Modeling of SSEs

5.4.1 Numerical Model and Implementation

To investigate the effects of pore pressure on SSEs, we used a recently proposed numerical method (Im et al., 2020) to simulate the SSEs in the North Hikurangi subduction zone. According to the rate-and-state friction (RSF) law (e.g., Dieterich, 1979; Ruina, 1983), friction (μ) is a function of slip velocity (V) and state variable (θ), which can be expressed as:

$$\mu = \mu_0 + a \cdot \ln(\frac{V}{V_0}) + b \cdot \ln(\frac{V_0 \cdot \theta}{D_c}) \tag{5-6}$$

where μ_0 is a reference friction coefficient at reference velocity V_0, a and b are empirical parameters determined from velocity step friction, and D_c is critical slip distance to renew surface contacts. Based on the slip law (Ruina, 1983), the evolution of state variable follows:

$$\frac{\mathrm{d}\theta}{\mathrm{d}t} = -\frac{V \cdot \theta}{D_c} \cdot \ln(\frac{V \cdot \theta}{D_c}) \tag{5-7}$$

where t is the time. Friction experiments (Ikari et al., 2013, 2020; Ikari & Kopf, 2017; Rabinowitz et al., 2018) revealed that the RSF parameters a and D_c are velocity-dependent, which can be written as (Im et al., 2020):

$$a = a_0 + S_a \cdot \log_{10}(\frac{V_a + V}{V_a}) \tag{5-8}$$

$$D_c = D_{c0} + S_{D_c} \cdot \log_{10}(\frac{V_{D_c} + V}{V_{D_c}}) \tag{5-9}$$

where a_0 is the reference RSF parameter a at reference velocity V_a, S_a is the slop describing log-linear dependence of parameter a on velocity, D_{c0} is the reference RSF parameter D_c at reference velocity V_{D_c}, and S_{D_c} is the slop describing log-linear dependence of parameter D_c on velocity.

Fault stability depends on a competition between the fault critical weakening rate (stiffness) K_c and the stiffness of the surroundings K (e.g., Scholz, 1998). When $K_c > K$, the drop of shear strength on the fault outpaces the elastic unloading of the surroundings due to slip, which leads to a stress imbalance and drives the slip instability (e.g., Gu et al., 1984; Ranjith & Rice, 1999). In contrast, $K_c < K$ inhibits fault slip by deceleration and results in frictional stability (e.g., Ruina, 1983; Ranjith & Rice, 1999). The critical stiffness K_c is determined by (Rice & Ruina, 1983):

$$K_c = -\frac{\sigma' \cdot V \cdot [\mathrm{d}\mu_{ss}(V)/\mathrm{d}V]}{D_c} \cdot \{1 + \frac{M \cdot V}{\sigma' \cdot D_c \cdot [\partial\mu(V,\theta)/\partial V]}\} \tag{5-10}$$

where σ' is the effective stress on the fault, M is the mass per unit area of the fault zone and $\mu_{ss}(V)$ is the velocity-dependent steady state friction at velocity V. $\mu_{ss}(V)$ is derived from equations (5-6) and (5-7), and can be formulated as follows (e.g., Scholz, 1998):

$$\mu_{ss} = \mu_0 + (a-b) \cdot \ln(\frac{V}{V_0}) \tag{5-11}$$

The fault motion is controlled by the Newton's second law (Im et al., 2017):

$$M \cdot \frac{\mathrm{d}^2\delta}{\mathrm{d}t^2} = K \cdot (\delta_{lp} - \delta) - \mu \cdot \sigma' \tag{5-12}$$

where δ is the fault displacement, δ_{lp} is the load point displacement (i.e., displacement of the surroundings).

To simulate the fault stick-slip motion, Im et al. (2017) derived the discretization equations for fault displacement, velocity, state variable, and friction coefficient based on equations (5-6), (5-7) and (5-12):

$$\delta^{i+1} = \left[\delta^i - (\delta_{lp}^{i+1} - \mu^{i+1} \cdot \sigma' / K)\right] \cdot \cos(\sqrt{K/M} \cdot \Delta t) + \frac{V^i}{\sqrt{K/M}} \cdot \sin(\sqrt{K/M} \cdot \Delta t) + (\delta_{lp}^{i+1} - \mu^{i+1} \cdot \sigma' / K) \tag{5-13}$$

$$V^{i+1} = 2 \cdot \frac{\delta^{i+1} - \delta^i}{\Delta t} - V^i \tag{5-14}$$

$$\theta^{i+1} = \theta^i - \left[\frac{V^{i+1} \cdot \theta^{i+1}}{D_c} \cdot \log(\frac{V^{i+1} \cdot \theta^{i+1}}{D_c})\right] \cdot \Delta t \tag{5-15}$$

$$\mu^{i+1} = \mu_0 + a \cdot \ln(\frac{V^{i+1}}{V_0}) + b \cdot \ln(\frac{V_0 \cdot \theta^{i+1}}{D_c}) \tag{5-16}$$

Following Im et al. (2020), we used equations (5-13)-(5-16) to simulate the shallow SSEs in the North Hikurangi. The RSF parameters a and D_c in equations (5-15) and (5-16) were updated in each time step according to equations (5-8) and (5-9). Equations (5-13)-(5-16) were solved with the Newton-Raphson method until the velocity converges. The input "RSF parameters" include a_0

= 0.005, S_a =0.005, b = 0.01, D_{c0} =10^{-6} m, S_{D_c} =2.5×10^{-6} m, μ_0 = 0.44, V_a = V_{D_c} = V_0 = 10^{-9} m/s. These parameters were not well constrained since friction experiments on different lithology of Hikurangi sediments yielded different values (e.g., Rabinowitz et al., 2018; Boulton et al., 2019; Ikari et al., 2020). But they are realistic for Hikurangi sediments and we tested if these values are capable of generating SSEs. A loading rate of 2×10^{-9} m/s which is similar to the convergence rate (Wallace et al., 2004) was assigned and used to constrain the displacement of the surroundings. Based on the accumulated fault thickness of 28 m and an average bulk density of 2.0 kg/cm^3 from MAD data at Site U1518 (Saffer et al., 2019b), we determined the fault zone mass per unit area M = 55580 kg/m^2. Previous study showed that SSEs in the North Hikurangi subduction zone may propagate to a depth of < 2 kmbsf (Wallace et al., 2016). We tested the possibility of SSEs at 2 kmbsf by inputting other key parameters at that depth. Using an average bulk density of 2.3 kg/cm^3, we estimated the lithostatic stress and then applied the maximum (0.93) and minimum (0.77) pore pressure ratios acquired from the fault zone at Site U1518 to constrain the effective stress on the fault. With the effective stress σ' = 3.2 MPa and σ' = 10.6 MPa, we further defined the stiffness of the surroundings K= 1.5 MPa/mm and K= 2.2 MPa/mm using our consolidation data. To initiate the simulation, we set an initial velocity V_{ini} = 10^{-10} m/s and assumed a steady state to calculate the initial state variable and friction coefficient. The initial fault displacement was set to zero.

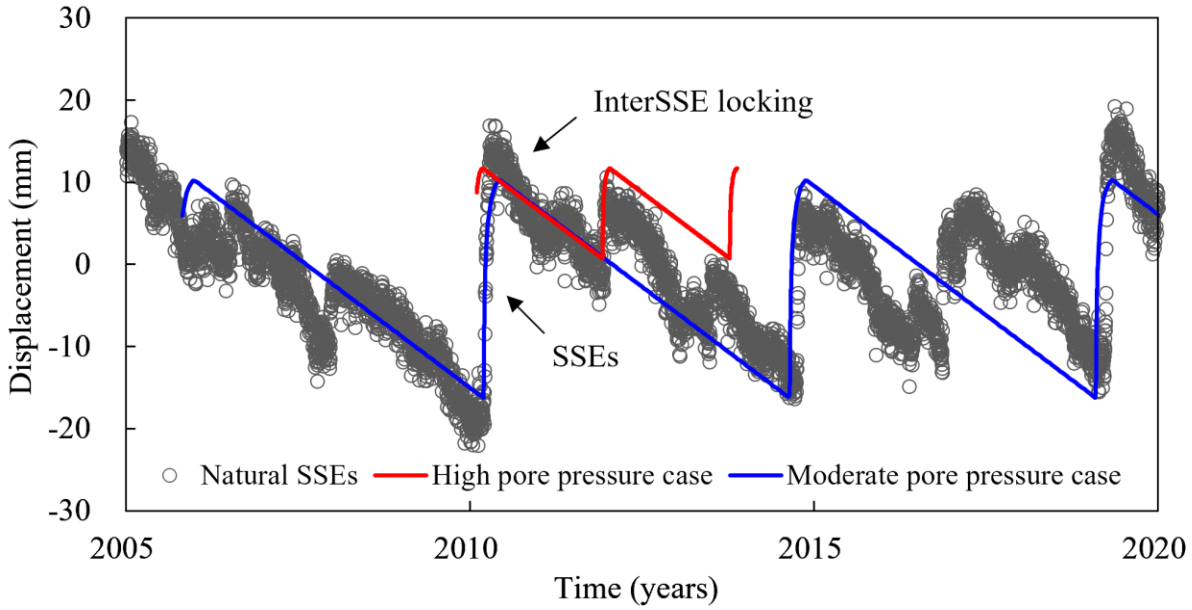

Figure 5-7. Comparison of natural SSEs with simulated SSEs at 2 kmbsf in the North Hikurangi subduction zone. The natural SSEs are observed from GPS data at station GISB. The GPS data are processed by the Nevada Geodetic Laboratory following Blewitt et al. (2018) and are publicly available online (http://geodesy.unr.edu/NGLStationPages/stations/GISB.sta).

5.4.2 Modeling Results and Implications

Our modeling results (Figure 5-7) are comparable to the natural SSEs observed by continuously operating global positioning system (cGPS). The cGPS data are from station GISB where shallow SSEs reoccur every 18 to 24 months (Figure 5-7, Wallace, 2020). The modeling result derived from high pore pressure condition (pore pressure ratio = 0.93) reveals an SSE recurrence interval of ~2 year and a displacement of ~10 mm for each SSE. These data generally match the natural SSEs with small displacement such as in 2011. In comparison, the modeling result derived from moderate pore pressure condition (pore pressure ratio = 0.77) shows an SSE recurrence interval of ~4 years and a displacement of ~30 mm. Although the moderate pore pressure case has obviously larger recurrence interval, its displacement is similar to the maximum SSE displacement observed from station GISB. Further, if we ignore the small displacement SSEs and only count the SSEs with large displacement, their recurrence interval is surprisingly consistent with the prediction of our model under moderate pore pressure condition. Therefore, the natural SSEs observed at station GISB can be simulated by our numerical model basing on well constrained pore pressure conditions.

Also, our modeling results show that the stress drop, peak slip velocity, total slip and recurrence interval of SSEs increase with the effective stress. This is in good agreement with (1) the laboratory observations that many parameters of SSEs including stress drop, peak slip velocity, slip velocity increase, duration, and total slip exhibit positive correlation with effective normal stress (Ikari et al., 2020), and (2) the field observations that the shallow SSEs (with low effective stress) in the North Hikurangi have smaller recurrence interval while the deep SSEs (with high effective stress) in the South Hikurangi have larger recurrence interval (Wallace, 2020). Therefore, we suggest that pore pressure exerts an important control on the characteristic of SSEs and the occurrence of frequent SSEs may indicate the sediments are overpressured. This explains why the tsunamigenic earthquake occurred in the North Hikurangi (Doser & Webb, 2003).

According to the fault-valve model (Sibson, 1990; Sibson et al., 1988), fault activity can increase the fault permeability and will lead to the drainage of pore fluids and thus decrease of excess pore pressure (i.e., increase of effective stress). Therefore, frequent SSEs in highly overpressured regions tend to evolve to become less frequent gradually. As in equation (5-10), increasing effective stress elevates the critical stiffness and drives the fault patch away from near-critical state. When the effective stress is sufficiently high, an earthquake may happen. This let us speculate that SSEs might be not only within the spectrum of fault slip, but also represent a transitional stage from conditionally stable sliding to earthquake slip. When the pore pressure is high, earthquake happens frequently but in a silent and slow way, that is, SSE. The SSEs facilitate the drainage of pore fluids and decrease the pore pressure. With the increase of effective stress, SSEs with a larger displacement occur episodically with a larger recurrence interval. When the effective stress increases to a certain level, ordinary earthquake happens. The evolution of SSEs to ordinary

earthquake is consistent with the observation that many known SSEs wrap around areas where ordinary earthquakes have also occurred (Saffer & Wallace, 2015).

We also note that one important issue missing in our discussion is frictional properties of sediments which exert a critical control on the fault slip behavior (e.g., Im et al., 2020). A more realistic model is that the combination of mechanical and frictional properties of sediments determines the modes of fault slip behavior to first order (e.g., Scholz, 1998) and different fault slip behavior can be viewed as manifestations of the heterogeneity of these properties (e.g., Collettini et al., 2011). The evolution of fault slip and the heterogeneity of fault patches are tightly interconnected (e.g., Fagereng et al., 2019). Our speculation needs to be verified by more detailed studies coupling pore pressure, frictional properties and their evolutions.

5.5 Conclusions

In this study, we conducted consolidation experiments on samples from IODP Site U1520 and estimated the pore pressure in the Northern Hikurangi subduction zone using consolidation data. Consolidation tests show that the sediment in trench-wedge facies is underconsolidated whereas that in pelagic and volcaniclastic facies is overconsolidated. Lithology, biostratigraphy and seismic reflection data (Saffer et al., 2019b; Barnes et al., 2019, 2020) suggest that the trench-wedge facies are stratigraphically equivalent to the horizon where the active Pāpaku splay fault occurs at IODP Site U1518. Based on a pore pressure prediction equation for Site U1518 derived from critical state soil mechanics, the pore pressure at the top of the Pāpaku fault constitutes 77% of lithostatic stress, whereas the pore pressure at the bottom increases to 93% of lithostatic stress. According to the RSF theory, SSEs at 2 kmbsf are simulated under above pore pressure conditions. The modeling results are comparable to the natural SSEs and indicate that high pore pressure decreases the recurrence interval of SSEs.

Supplementary Material

Table S5-1. Details of the whole round samples in this study.

Sample NO.	Site	Hole	Core	Type	Section	Depth (mbsf)	Unit
NO01	U1520	D	13	H	6	119	II
NO02	U1520	D	22	F	3	184	II
NO03	U1520	D	30	F	2	246	III
NO04	U1520	D	47	X	CC	477	III
NO05	U1520	C	4	R	4	666	IV
NO06	U1520	C	14	R	6	765	IV
NO07	U1520	C	18	R	3	799	IV
NO08	U1520	C	26	R	4	876	V
NO09	U1520	C	37	R	3	980	V

Table S5-2. Results of the consolidation experiments

Sample NO.	Depth	σ_v (Pa)	P_{hy} (Pa)	σ'_{hy} (Pa)	σ'_{pc_Casa} (Pa)	σ'_{pc_Becker} (Pa)	σ'_{pc_min} (Pa)	σ'_{pc_max} (Pa)
NO01	119	2120413	1194905	925507	604092	575547	486506	765862
NO02	184	3309290	1846251	1463038	586887	630298	541795	702725
NO03	246	4461269	2469872	1991396	1009219	1027449	702233	1728968
NO04	477	8771459	4789565	3981894	1125918	1471856	1128750	1452023
NO05	666	12282575	6688354	5594220	12058619	12504167	10074717	16456256
NO06	765	14344080	7684762	6659318	11590173	12392494	11558520	14215128
NO07	799	15066303	8028818	7037485	13246858	13462288	12251668	14688477
NO08	876	16560415	8798399	7762016	15487700	17276768	15263836	23232361
NO09	980	18677185	9846741	8830444	23293299	25806553	23586291	32912512

Chapter 6: Conclusions and Outlook

6.1 Conclusions

In this Ph.D. study, the pore pressure in the Nankai Trough, North Sumatra and Northern Hikurangi subduction zones is investigated through multi approaches including uniaxial consolidation experiments, porosity-based prediction equations and numerical fluid flow models. In order to improve the performance of the porosity-based pore pressure prediction approach for overconsolidated sediments, a new method which accounts for the consolidation state of sediments is proposed building on a recent critical state soil mechanics model, and is successfully applied to the Nankai Trough. The pore pressure estimates presented in this Ph.D. dissertation provide important insights for understanding the hydro-mechanical processes in the Nankai Trough, North Sumatra and Northern Hikurangi subduction zones, and are linked to the occurrence of tsunamigenic earthquakes and slow slip events. The main conclusions are as follows:

(1) In the Nankai Trough, excess pore pressure is revealed in both accreted and underthrust sediments at IODP Site C0023. The excess pore pressure increases continuously across the accretionary prism and underthrust section, with nearly constant ratios of pore pressure to lithostatic stress. This implies that accreted and underthrust sediments constitute one hydrogeological system and the plate interface (décollement) is not a fluid barrier as previously believed. Pore pressures 84%-93% of the lithostatic stress is inferred along the subduction thrust based on uniaxial consolidation data and seem attributable to the propagation of the frontal thrust which causes repeated lithostatic pore pressure transients migrated along faults in the last 3 kyrs. The resulting extremely low shear strength is similar to the estimated coseismic shear strength in the 2011 Tohoku earthquake. Seismic reflection data indicate that the high pore pressure may extend to a large area (Park et al., 2014). If the pore pressure is similarly high as revealed at Site C0023, seismic slip could be propagated to the trench and causes tsunami hazard offshore SW Japan when a large earthquake occurs.

(2) Based on the newly developed pore pressure prediction method which accounts for the consolidation state of sediments, the overconsolidated sediment in the Nankai Trough generates 40%~50% less excess pore pressure than the normally consolidated sediment, suggesting that overconsolidation inhibits the development of excess pore pressure. The lower excess pore pressure in overconsolidated sediments is attributed to the decrease of loading efficiency. For shallow sediments, overconsolidated sediments suppress the pore pressure build-up and reduce the likelihood of slope failure. In contrast, the inhibition of excess pore pressure in deeply seated sediments facilitates the instability of faults and thus the generation of earthquakes by driving the friction stability parameter ζ more negative. The pore pressure prediction in the Nankai accretionary prism off Muroto Peninsula revels a weak décollement with shear strength < 2.2 MPa. However, its corresponding shear stress is even lower (< 0.4 MPa), which implies that the accretionary prism is not at Coulomb failure.

(3) In the North Sumatra subduction zone, mainly hydrostatic to low excess pore pressure is reveled at IODP Sites U1480 and U1481, while a horizon which is considered as the potential candidate for the future décollement shows moderate excess pore pressure. According to a one-dimensional sedimentation-flow model which accounts for the sedimentation rate and silicate dehydration, present excess pore pressure of the proto-décollement horizon results from high sedimentation rate and silicate dehydration. As the sediment approaches the subduction zone, the excess pore pressure increases continuously and the dehydration of silicate makes an increasing contribution to the excess pore pressure. The pore pressure in the proto-décollement horizon reaches >90% of the lithostatic stress when plate subduction and thus high excess pore pressure is inferred along the décollement in the North Sumatra subduction zone. Together with the landward-directed lateral friction exerted by higher subduction velocity to the southeast (McNeill & Henstock, 2014), the high excess pore pressure might lead to the landward vergence of frontal thrusts. The high pore pressure and landward vergent frontal thrusts provide a plausible explanation for the occurrence of the Mw 9.2 2004 Sumatra-Andaman tsunamigenic earthquake.

(4) In the Northern Hikurangi subduction zone, consolidation experiments on samples from IODP Site U1520 show that the sediment in trench-wedge facies is underconsolidated whereas that in pelagic and volcaniclastic facies is overconsolidated. Lithology, biostratigraphy and seismic reflection data (Saffer et al., 2019b; Barnes et al., 2019, 2020) suggest that the trench-wedge facies are stratigraphically equivalent to the horizon where the active Pāpaku splay fault occurs at IODP Site U1518. Based on the consolidation data on trench-wedge facies, a pore pressure prediction equation for Site U1518 is derived using critical state soil mechanics. Pore pressure 77% of lithostatic stress is revealed at the top of the Pāpaku fault, whereas the pore pressure at the bottom increases to 93% of lithostatic stress. Previous studies have shown that SSEs in the North Hikurangi subduction zone may propagate to a depth of < 2 km below seafloor (Wallace et al., 2016). Therefore, SSEs at 2 km below seafloor are simulated under above pore pressure conditions according to the rate-and-state friction (RSF) theory. The modeling results are comparable to the natural SSEs and indicate that high pore pressure decreases the recurrence interval of SSEs.

6.2 Outlook

Pore pressure has been a subject of ongoing concern since 1950s due to the important role it plays in fluid circulation, structural development of sediments and rocks, and fault slip and earthquake nucleation (e.g., Saffer & Tobin, 2011). Therefore, predicting pore fluid pressure is crucial to improve our understanding on the hydro-mechanical processes in subduction zones. This Ph.D. study has generated new insights into the distribution of excess pore pressure and its implication for the slip behavior of the plate interface through pore pressure prediction in three typical subduction zones. Building on this Ph.D. study, following aspects should be improved or examined by future research:

(1) A focus in pore pressure prediction is to establish robust constitutive models for the sediment (e.g., Karig, 1986). Based on this idea and previous models (e.g., Flemings & Saffer, 2018), this Ph.D. dissertation proposes a new pore pressure prediction method for overconsolidated sediments in the accretionary prism and shows that the pore pressure of overconsolidated sediment can be well predicted from porosity. A key parameter in the proposed method is the ratio of horizontal to vertical effective stress in the accretionary prism, which can be acquired by assuming a state of Coulomb failure (e.g., Flemings & Saffer, 2018). For the sediments in a stable state, the stress ratio can be estimated using the dynamic Coulomb wedge theory (Wang & Hu, 2006). Therefore, a promising topic for further research is to provide a universal pore pressure prediction pathway for both sediments at Coulomb failure and steady state by combining critical state soil mechanics and the dynamic Coulomb wedge theory.

(2) It has been widely accepted that there is high pore pressure in underthrust sediments and megathrust faults (e.g., Skarbek & Saffer, 2009; Tobin & Saffer, 2009) and it has an important impact on the distribution of seismogenic zones (e.g., Moore & Saffer, 2001). Based on this Ph.D. study, high pore pressure not only exists in underthrust sediments and megathrust faults, but also is widely-distributed in the accretionary prism. Pore pressure is thought to govern the degree of interseismic locking and high pore pressure seems responsible for poor locking (Moreno et al., 2014). This makes large earthquakes unlikely to nucleate on the reverse faults of overpressured accretionary prism, which is in good agreement with the occurrence of very low frequency earthquakes in some overpressured accretionary prisms (e.g., Ito & Obara, 2006). But on the other hand, high pore pressure will decrease the shear strength of reverse faults within accretionary prism and thus facilitates the propagation of seismic slip through to the trench, when a large earthquake happens down-dip. Therefore, more attention should be paid to the pore pressure in accretionary prism in future studies, since it is critical for assessment of the geological hazard potential.

(3) Current pore pressure prediction research mainly focuses on characterization of static pore pressure. Another important direction for future research is to monitor the time-series pore pressure variations, because recent instrumentation such as the long-term borehole monitoring system (LTBMS) has enabled the continuous observation of in situ pore pressure, temperature, strain and pore water composition (e.g., Kopf et al., 2017). In fact, the LTBMS data is heavily underrated, and it has the potential to constrain the in situ permeability of faults (e.g., Kinoshita & Saffer, 2018) and to shed light on the permeability evolution with pore pressure variations. This provides a unique opportunity to better understand the role of faults in fluid-mediated processes and will advance our knowledge on the evolution of fault slip and earthquake cycles.

(4) Although high pore pressure has been widely invoked to explain the occurrence of tsunamigenic coseismic slip near the trench (e.g., Seno, 2002), the causal relationship between high pore pressure and tsunami generation remains incompletely understood. Faulkner et al. (2011) explained the shallow coseismic slip from the point of view of energy and proposed that the weak sediment is energetically favorable for the slip propagation and permits the coseismic slip near the

trench. However, this explanation does not answer how the coseismic slip propagates in velocity strengthening material, because according to the rate-and-state friction (RSF) law, velocity strengthening material is intrinsically stable (e.g., Gu et al., 1984; Ranjith & Rice, 1999). Based on this Ph.D. study, widely high pore pressure does exist in some shallow subduction zones where tsunami occurred, and the generation of tsunamis seems to be related to high pore pressure indeed. The propagation of coseismic slip might be related to the velocity of dynamic loading. When the velocity of dynamic loading is high enough, although the velocity strengthening material will prevent the velocity from being infinite, a certain velocity can be reached and thus coseismic slip can occur. This hypothesis can be examined by future numerical modeling, which will contribute to a more complete insight into the fault slip behavior in different materials.

Appendix

A.1 IODP-ICDP Kolloquium 2019 Abstract

Near lithostatic pore pressures prepare the Nankai décollement for the next megatsunami offshore SW Japan*

Junli Zhang, Andre Hüpers, Stefan Kreiter and Achim Kopf

MARUM–Center for Marine Environmental Sciences, University of Bremen, Leobener Straße 8, 28359 Bremen, Germany

*This abstract was published in IODP-ICDP Colloquium, Cologne, Germany, 18-20 March 2019. https://www.bgr.bund.de/DE/Themen/MarineRohstoffforschung/IODP/Downloads/kolloquiumsband-2019.pdf

ABSTRACT

Earthquakes along subduction zones cause devastating tsunamis when seismic slip reaches near the trench and displaces the seafloor by tens of meters, as seen in the 2011 Tohoku earthquake (Fujii et al., 2011). To explain tsunamigenic earthquake occurrence, high pore pressure in forearc sediments has been proposed as a mechanism (e.g., Seno, 2002), but direct pore pressure observations along subduction thrusts are still sparse.

Here we provide robust experimental estimates of pore pressure based on consolidation tests. Our samples derive from IODP Site C0023, where the whole accreted and subducted sediment succession was recovered at the seaward edge of the central Nankai Trough accretionary prism offshore Muroto peninsula. Our data indicate pore pressures in the accreted Upper Shikoku Basin facies to outer trench-wedge facies are nearly hydrostatic while samples in the underthrust sequence are overpressured, which is consistent with previous studies. More importantly, our data reveal high excess pore pressure at the top of the décollement. Further hydrogeological modelling based on Cl concentrations suggests that the high excess pore pressure is mainly attributed to pressure translation through recent fluid discharge along permeable faults and overpressured horizon is not confined to Site C0023 but to a considerable areal extent. The high excess pore pressure leads to much lower shear strength than previously thought. Lower shear strength means less energy dissipation and that might explain how a large rupture might not be arrested from propagating to the trench as in the Tohoku earthquake (Faulkner et al., 2011). Hence, the very weak décollement of Nankai Trough subduction zone makes a catastrophic tsunami offshore SW Japan very likely.

A.2 AGU Fall Meeting 2019 Abstract

The effect of consolidation state on pore pressure development in the Nankai accretionary prism off Muroto Peninsula, SW Japan*

Junli Zhang, Andre Hüpers, Stefan Kreiter, Walter Menapace and Achim Kopf

MARUM–Center for Marine Environmental Sciences, University of Bremen, Leobener Straße 8, 28359 Bremen, Germany

*This abstract was published in AGU Fall Meeting, San Francisco, USA, 9-13 December 2019. https://ui.adsabs.harvard.edu/abs/2019AGUFM.T51G0370Z/abstract

ABSTRACT

In subduction zones, pore pressure is intimately associated with fluid flow and structural development of sediments and rocks (Saffer and Tobin, 2011). Therefore, pore pressure is a key parameter to understand the hydro-mechanically coupled processes in subduction forearcs. However, direct pore pressure observations are rare. Flemings and Saffer (2018) recently proposed a porosity-based modeling approach to predict pore pressure based on critical state soil mechanics and Coulomb failure theory, which takes into account the stress path of sediments. This study advances upon their work by introducing the consolidation state of sediments into the model to explore the effect of overconsolidation on pore pressure development.

We select IODP Site C0023 as our case study site, which is located at the seaward edge of the central Nankai Trough accretionary prism offshore the Muroto peninsula, where numerous consolidation studies indicate overconsolidation of the incoming sediments. The modeled excess pore pressure of accreting sediments at Site C0023 ranges from 1 MPa to 3 MPa, which is overall consistent with values inferred from consolidation test results. Compared with pore pressure modeled for a normally consolidated sediment, the overconsolidated sediment generates 40% ~ 50% less excess pore pressure, implying that the overconsolidation inhibits the development of excess pore pressure. Our modeling results are consistent with the view of rapid loading by burial and horizontal compression causing elevated pore pressure in low permeable clay-rich subduction zone sediments, and we additionally show that the consolidation state plays a crucial role for the magnitude and spatial distribution of excess pore pressure in accretionary prisms.

Acknowledgements

This Ph.D. study was conducted at the MARUM – Center for Marine Environmental Sciences, University of Bremen, under the supervision of Prof. Dr. A. J. Kopf and Dr. A. Hüpers. I am grateful to my supervisor Prof. Dr. A. J. Kopf who gave me complete freedom to pursue the research topic that interests me, supported me to attend AGU Fall Meeting 2019, recommended me to participate in IODP Expedition 358 and Meteor cruise M167, and gave me great help in manuscript writing and revision. I also would like to thank my second supervisor Dr. A. Hüpers who patiently taught me to conduct experiments and process data step by step, offered me endless help in data interpretation, numerical modeling, and manuscript writing and revision, and encouraged me to participate conferences and research cruises.

I also acknowledge the financial supports from the China Scholarship Council (CSC), the Bremen Early Career Researcher Development (BYRD) center and Central Research Development Fund (CRDF) at university of Bremen, the German Research Foundation (DFG), the Federal Institute for Geosciences and Natural Resources (BGR) and the EU Marine Robots project. The CSC and BYRD funded my Ph.D. study at University of Bremen. The CRDF and my supervisor Prof. Dr. A. J. Kopf funded me to attend AGU Fall Meeting 2019. The DFG funded me to attend IODP/ICDP-Kolloqium 2019. The BGR funded me to participate in IODP Expedition 358 in the framework of the DFG - SPP 527 priority program. The EU Marine Robots project funded the Meteor cruise M167.

I would like to thank my colleagues M. Ikari, W. Menapace, S. Kreiter, P. Renken, T. Fleischmann, C. Zoellner, Y. Ruan, Q. Zhu, T. W. Wu, A. Rösner, K. Stanislowski, A. M. Eijsink, N. Behrendt, G. Wiemer, C. Witt and P. Haberkorn who gave me scientific, technical and administrative advice and support throughout my Ph.D. study. I also would like to thank all the people I sailed with, who gave me great help during the research cruise.

Last, I want to express my deepest gratitude to my parents, sister and girlfriend who always love, care, and trust me. Without their continuous support and understanding, I would not be where I am in life.

References

Adam, J., Klaeschen, D., Kukowski, N., & Flueh, E. (2004). Upward delamination of Cascadia Basin sediment infill with landward frontal accretion thrusting caused by rapid glacial age material flux. *Tectonics*, *23*, TC3009. https://doi.org/10.1029/2002TC001475

Ammon, C. J., Ji, C., Thio, H. K., Robinson, D., Ni, S., Hjorleifsdottir, V., et al. (2005). Rupture process of the 2004 Sumatra-Andaman earthquake. *Science*, *308*, 1133–1139. https://doi.org/10.1126/science.1112260

Ando, M. (1975). Source mechanisms and tectonic significance of historical earthquakes along the Nankai Trough, Japan. *Tectonophysics*, *27*, 119–140. https://doi.org/10.1016/0040-1951(75)90102-x

Arnulf, A. F., Biemiller, J., Lavier, L., Wallace, L. M., Bassett, D., Henrys, S., et al. (2021). Physical conditions and frictional properties in the source region of a slow-slip event. *Nature Geoscience*, *14*(5), 334–340. https://doi.org/10.1038/s41561-021-00741-0

ASTM International (2011). *Standard test methods for one-dimensional consolidation properties of soils using incremental loading, D2435/D2435M-11*. West Conshoshocken, PA: ASTM International.

Azizi, F. (2000). *Applied analyses in geotechnics*. London: E&FN Spon.

Bangs, N. L., Shipley, T. H., Gulick, S. P., Moore, G. F., Kuromoto, S., & Nakamura, Y. (2004). Evolution of the Nankai Trough décollement from the trench into the seismogenic zone: Inferences from three-dimensional seismic reflection imaging. *Geology*, *32*, 273–276. https://doi.org/10.1130/g20211.2

Barnes, P. M., Wallace, L. M., Saffer, D. M., Pecher, I. A., Petronotis, K. E., LeVay, L. J., et al. (2019). Site U1520. *In* Wallace, L. M., Saffer, D. M., Barnes, P. M., Pecher, I. A., Petronotis, K. E., LeVay, L. J., and the Expedition 372/375 Scientists, Hikurangi Subduction Margin Coring, Logging, and Observatories. *Proceedings of the International Ocean Discovery Program, 372B/375*: College Station, TX (International Ocean Discovery Program). https://doi.org/10.14379/iodp.proc.372B375.105.2019

Barnes, P. M., Wallace, L. M., Saffer, D. M., Bell, R. E., Underwood, M. B., Fagereng, A., et al. (2020). Slow slip source characterized by lithological and geometric heterogeneity. *Science Advances*, *6*, eaay3314. https://doi.org/10.1126/sciadv.aay3314

Becker, D. E., Crooks, J. H. A., Been, K., & Jefferies, M. G. (1987). Work as a criterion for determining in situ and yield stresses in clays. *Canadian Geotechnical Journal*, *24*, 549–564. https://doi.org/10.1139/t87-070

Becker, K., Fisher, A. T., & Davis, E. E. (1997). The CORK experiment in Hole 949C: Long-term observations of pressure and temperature in the Barbados accretionary prism. In T. H. Shipley, Y. Ogawa, P. Blum, & J. M. Bahr (Eds.), *Proceedings of the Ocean Drilling Program*, *Scientific Results*, *156*, 247–252. College Station, TX: Ocean Drilling Program.

Behrmann, J. H. (1991). Conditions for hydrofracture and the fluid permeability of accretionary wedges. *Earth and Planetary Science Letters*, *107*, 550–558. https://doi.org/10.1016/0012-821X(91)90100-V

Bekins, B. A., & Dreiss, S. (1992). A simplified analysis of parameters controlling dewatering in accretionary prisms. *Earth and Planetary Science Letters*, *109*(3–4), 275–287. https://doi.org/10.1016/0012-821x(92)90092-a

Bekins, B. A., McCaffrey, A., & Dreiss, S. J. (1995). Episodic and constant flow models for the origin of low-chloride waters in a modem accretionary complex. *Water Resources Research*, *31*, 3205–3215. https://doi.org/10.1029/95wr02569

Bekins, B. A., & Screaton, E. J. (2007). 6. Pore Pressure and Fluid Flow in the Northern Barbados Accretionary Complex. In T. H. Dixon, & J. C. Moore (Eds.), *The seismogenic zone of subduction thrust faults* (pp. 148–170). New York, NY: Columbia University Press.

Bellew, G. M. (2004). Consolidation properties, stress history, and modeling of pore pressures for deep sea sediments at the Nankai Trough, Master thesis. University of Missouri-Columbia.

Bjerrum, L. (1973). Problems of soil mechanics and construction on soft clays. State of the art report, Session 4. *Proceedings of the Eighth International Conference on Soil Mechanics and Foundation Engineering*, *3*, 109–159. Moscow.

Bletery, Q., Sladen, A., Jiang, J., & Simons, M. (2016). A Bayesian source model for the 2004 great Sumatra-Andaman earthquake. *Journal of Geophysical Research: Solid Earth*, *121*(7), 5116–5135. https://doi.org/10.1002/2016JB012911

Blewitt, G., Hammond, W. C., & Kreemer, C. (2018). Harnessing the GPS data explosion for interdisciplinary science. *Eos*, *99*. https://doi.org/10.1029/2018EO104623

Bolton, A. J., Maltman, A. J., & Clennell, M. B. (1998). The importance of overpressure timing and permeability evolution in fine-grained sediments undergoing shear. *Journal of Structural Geology*, *20*, 1013–1022. https://doi.org/10.1016/s0191-8141(98)00030-3

Boudreau, B. P. (1997). *Diagenetic Models and Their Implementation: Modelling Transport and Reactions in Aquatic Sediments*. Berlin: Springer.

Boulton, C., Niemeijer, A. R., Hollis, C. J., Townend, J., Raven, M. D., Kulhanek, D. K., & Shepherd, C. L. (2019). Temperature-dependent frictional properties of heterogeneous Hikurangi Subduction Zone input sediments, ODP Site 1124. *Tectonophysics*, *757*, 123–139. https://doi.org/10.1016/j.tecto.2019.02.006

Bray, C. J., & Karig, D. E. (1988). Dewatering and extensional deformation of the Shikoku Basin hemipelagic sediments in the Nankai Trough. *Pure and Applied Geophysics*, *128*, 724–739. https://doi.org/10.1007/bf00874554

Bredehoeft, J. (2009). Maintaining high fluid pressures in older sedimentary basins. *Geofluids*, *9*(3), 179–181. https://doi.org/10.1111/j.1468-8123.2009.00252.x

Brown, K. M., Bekins, B., Clennell, B., Dewhurst, D., & Westbrook, G. (1994). Heterogeneous hydrofracture development and accretionary fault dynamics. *Geology*, *22*(3), 259–262. https://doi.org/10.1130/0091-7613(1994)022<0259:hhdaaf>2.3.co;2

Brown, K. M., Kopf, A., Underwood, M. B., & Weinberger, J. L. (2003). Compositional and fluid pressure controls on the state of stress on the Nankai subduction thrust: A weak plate boundary. *Earth and Planetary Science Letters*, *214*, 589–603. https://doi.org/10.1016/S0012-821X(03)00388-1

Brown, K. M, Saffer, D. M., & Bekins, B. A. (2001). Smectite diagenesis, pore-water freshening, and fluid flow at the toe of the Nankai wedge. *Earth and Planetary Science Letters*, *194*, 97–109. https://doi.org/10.1016/s0012-821x(01)00546-5

Brumund, W. F., Jonas, E., & Ladd, C. C. (1976). Estimating in situ maximum past (preconsolidation) pressure of saturated clays from results of laboratory consolidometer tests. Transportation Research Board Special Report.163

Butterfield, R. (1979). A natural compression law for soils (an advance on e-log p'). *Geotechnique*, *29*, 469–480. https://doi.org/10.1680/geot.1979.29.4.469

Casagrande, A. (1936). The determination of pre-consolidation load and it's practical significance. *Proceedings of the International Conference on Soil mechanics and Foundation Engineering*, *3*, 60-64. Cambridge, MA: Harvard University.

Casey, B. (2014). The consolidation and strength behavior of mechanically compressed fine-grained sediments. PhD Thesis. Cambridge, MA: Department of Civil and Environmental Engineering. Massachusetts Institute of Technology.259

Casey, B., Germaine, J. T., Flemings, P. B., & Fahy, B. P. (2016). In situ stress state and strength in mudrocks. *Journal of Geophysical Research: Solid Earth*, *121*, 5611–5623. https://doi.org/10.1002/2016jb012855

Chlieh, M., Avouac, J. P., Sieh, K., Natawidjaja, D. H., & Galetzka, J. (2008). Heterogeneous coupling of the Sumatran megathrust constrained by geodetic and paleogeodetic measurements. *Journal of Geophysical Research*, *113*(B05305). https://doi.org/10.1029/2007JB004981

Clementino, R. V. (2005). Discussion of "An oedometer test study on the preconsolidation stress of glaciomarine clays". *Canadian Geotechnical Journal*, *42*(3), 972–974. https://doi.org/10.1139/t05-010

Collettini, C., Niemeijer, A., Viti, C., Smith, S. A., & Marone, C. (2011). Fault structure, frictional properties and mixed-mode fault slip behavior. *Earth and Planetary Science Letters*, *311*, 316–327. https://doi.org/10.1016/j.epsl.2011.09.020

Costa Pisani, P., Reshef, M., & Moore, G. (2005). Targeted 3-D prestack depth imaging at Legs 190-196 ODP drill sites (Nankai Trough, Japan). *Geophysical Research Letters*, *32*(L20309). https://doi.org/10.1029/2005GL024191

Couzens-Schultz, B. A., & Chan, A. W. (2010). Stress determination in active thrust belts: An alternative leak-off pressure interpretation. *Journal of Structural Geology*, *32*(8), 1061–1069. https://doi.org/10.1016/j.jsg.2010.06.013

Cubas, N., Souloumiac, P., & Singh, S. C. (2016). Relationship link between landward vergence in accretionary prisms and tsunami generation. *Geology*, *44*(10), 787–790. https://doi.org/10.1130/G38019.1

Dahlen, F. A. (1984). Noncohesive critical Coulomb wedges: An exact solution. *Journal of Geophysical Research: Solid Earth*, *89*(B12), 10125–10133. https://doi.org/10.1029/JB089iB12p10125

Dahlen, F. A. (1990). Critical taper model of fold-and-thrust belts and accretionary wedges. *Annual Review of Earth and Planetary Sciences*, *18*, 55–99. https://doi.org/10.1146/annurev.ea.18.050190.000415

Daigle, H., & Dugan, B. (2014). Data report: permeability, consolidation, stress state, and pore system characteristics of sediments from Sites C0011, C0012, and C0018 of the Nankai Trough. In P. Henry, T. Kanamatsu, & K. Moe (Eds.), *Proceedings of the Integrated Ocean Drilling Program, 333*. Tokyo: Integrated Ocean Drilling Program Management International, Inc. https://doi.org/10.2204/iodp.proc.333.201.2014

Darcy, H. (1856). *Les Fontaines Publiques de la Ville de Dijon* (pp. 304–311). Paris: Victor Dalmont.

Davis, D., Suppe, J., & Dahlen, F. A. (1983). Mechanics of fold-and- thrust belts and accretionary wedges. *Journal of Geophysical Research*, *88*(B2), 1153–1172. https://doi.org/10.1029/JB088iB02p01153

Davis, R. O., & Selvadurai, A. P. S. (1996). *Elasticity and geomechanics*. Cambridge: Cambridge University Press.

Dean, S. M., McNeill, L. C., Henstock, T. J., Bull, J. M., Gulick, S. P. S., Austin, J. A., et al. (2010). Contrasting décollement and prism properties over the Sumatra 2004–2005 earthquake rupture boundary. *Science*, *329*, 207–210. https://doi.org/10.5040/9780755621101.0007

Deming, D. (1994). Factors necessary to define a pressure seal. *AAPG Bulletin*, *78*, 1005–1009. https://doi.org/10.1306/A25FE40F-171B-11D7-8645000102C1865D

DeShon, H. R., Schwartz, S. Y., Bilek, S. L., Dorman, L. M., Gonzalez, V., Protti, J. M., Flueh, E. R., & Dixon, T. H. (2003). Seismogenic zone structure of the southern Middle America trench, Costa Rica. *Journal of Geophysical Research: Solid Earth*, *108*(B10). https://doi.org/10.1029/2002JB002294

Dieterich, J. H. (1979). Modeling of rock friction 1. Experimental results and constitutive equations. *Journal of Geophysical Research*, *84*, 2161–2168. https://doi.org/10.1029/JB084iB05p02161

Doser, D. I., & Webb, T. H. (2003). Source parameters of large historical (1917-1961) earthquakes, North Island, New Zealand. *Geophysical Journal International*, *152*, 795–832. https://doi.org/10.1046/j.1365-246X.2003.01895.x

Dugan, B., & Daigle, H. (2011). Data report: permeability, compressibility, stress state, and grain size of shallow sediments from Sites C0004, C0006, C0007, and C0008 of the Nankai accretionary complex. In M. Kinoshita, H. Tobin, J. Ashi, G. Kimura, S. Lallemant, E. J. Screaton, et al. (Eds.), *Proceedings of the Integrated Ocean Drilling Program, 314/315/316*. Washington, DC: Integrated Ocean Drilling Program Management International, Inc. https://doi.org/10.2204/iodp.proc.314315316.208.2011

Dugan, B., Flemings, P. B., Olgaard, D. L., & Gooch, M. J. (2003). Consolidation, effective stress, and fluid pressure of sediments from ODP Site 1073, US mid-Atlantic continental slope. *Earth and Planetary Science Letters*, *215*, 13–26. https://doi.org/10.1016/S0012-821X(03)00425-4

Dugan, B., & Germaine, J. T. (2008). Near-seafloor overpressure in the deepwater Mississippi Canyon, northern Gulf of Mexico. *Geophysical Research Letters*, *35*, L02304. https://doi.org/10.1029/2007gl032275

Eaton, B. A. (1972). The Effect of Overburden Stress on Geopressure Prediction from Well Logs. *Journal of Petroleum Technology*, *24*(8), 929–934. https://doi.org/10.2118/3719-pa

Erickson, N., & Jarrard, R. D. (1998). Velocity-porosity relationships for water-saturated sediments. *Journal of Geophysical Research*, *103*(B12), 30385–30406. https://doi.org/10.1029/98JB02128

Fagereng, A., & Ellis, S. (2009). On factors controlling the depth of interseismic coupling on the Hikurangi subduction interface, New Zealand. *Earth and Planetary Science Letters*, *278*, 120–130. https://doi.org/10.1016/j.epsl.2008.11.033

Fagereng, Å., Savage, H. M., Morgan, J. K., Wang, M., Meneghini, F., Barnes, P. M., et al. (2019). Mixed deformation styles observed on a shallow subduction thrust, Hikurangi margin, New Zealand. *Geology, 47*, 872–876, https://doi.org/10.1130/G46367.1

Faulkner, D. R., Mitchell, T. M., Behnsen, J., Hirose, T., & Shimamoto, T. (2011). Stuck in the mud? Earthquake nucleation and propagation through accretionary forearcs. *Geophysical Research Letters*, *38*, L18303. https://doi.org/10.1029/2011gl048552

Faulkner, D. R., & Rutter, E. H. (1998). The gas permeability of clay-bearing fault gouge at 20°C. In R. J. Knipe, G. Jones, & Q. Fischer (Eds.), *Faulting, fault sealing and fluid-flow in hydrocarbon reservoirs Vol. 147*, (pp. 147–156). Geologic Society, London, Special Publications. http://dx.doi.org/10.1144/GSL.SP.1998.147.01.10

Feeser, V., Moran, K., & Bruckmann, W. (1993). Stress-regime-controlled yield and strength behavior of sediment from the frontal part of the Nankai accretionary prism. In I. A. Hill, et al. (Eds.), *Proceedings of the Ocean Drilling Program*, *Scientific Results*, *131*, 261–273. College Station, TX: Ocean Drilling Program.

Fetter, C. W. (2013). *Applied Hydrogeology* (4th Edition). Essex: Pearson Education Limited.

Fisher, A. T., & Zwart, G. (1997). Packer experiments along the decollement of the Barbados accretionary complex: Measurements of in situ permeability. In T. H. Shipley, Y. Ogawa, P. Blum, & J. M. Bahr (Eds.), *Proceedings of the Ocean Drilling Program*, *Scientific Results*, *156*, 199–218. College Station, TX: Ocean Drilling Program.

Flemings, P., Long, H., Dugan, B., Germaine, J., John, C. M., Behrmann, J. H., Sawyer, D., & IODP Expedition 308 Scientists (2008). Pore pressure penetrometers document high overpressure near the seafloor where multiple submarine landslides have occurred on the continental slope, offshore Louisiana,

Gulf of Mexico. *Earth and Planetary Science Letters*, *269*, 309–325. https://doi.org/10.1016/j.epsl.2007.12.005

Flemings, P. B., & Saffer, D. M. (2018). Pressure and stress prediction in the Nankai accretionary prism: A critical state soil mechanics porosity-based approach. *Journal of Geophysical Research: Solid Earth*, *123*, 1089–1115. https://doi.org/10.1002/2017jb015025

Fujii, Y., Satake, K., Sakai, S. I., Shinohara, M., & Kanazawa, T. (2011). Tsunami source of the 2011 off the Pacific coast of Tohoku Earthquake. *Earth, Planets and Space*, *63*, 815–820. https://doi.org/10.5047/eps.2011.06.010

Fujiwara, T., Kodaira, S., No, T., Kaiho, Y., Takahashi, N., & Kaneda, Y. (2011). The 2011 Tohoku-Oki earthquake: Displacement reaching the trench axis. *Science*, *334*(6060), 1240. https://doi.org/10.1126/science.1211554

Fulton, P. M., Brodsky, E. E., Kano, Y., Mori, J. J., Chester, F. M., Ishikawa, T., et al., & the Expedition 343, 343T, and KR13-08 Scientists (2013). Low coseismic friction on the Tohoku-Oki fault determined from temperature measurements. *Science*, *342*, 1214–1217. https://doi.org/10.1126/science.1243641

Gamage, K., & Screaton, E. (2006). Characterization of excess pore pressures at the toe of the Nankai accretionary complex, Ocean Drilling Program sites 1173, 1174, and 808: Results of one-dimensional modeling. *Journal of Geophysical Research*, *111*, B04103. https://doi.org/10.1029/2004jb003572

Geersen, J., McNeill, L., Henstock, T. J., & Gaedicke, C. (2013). The 2004 Aceh-Andaman Earthquake: Early clay dehydration controls shallow seismic rupture. *Geochemistry, Geophysics, Geosystems*, *14*(9), 3315–3323. https://doi.org/10.1002/ggge.20193

Gordon, D. S., & Flemings, P. B. (1998). Generation of overpressure and compaction-driven fluid flow in a Plio-Pleistocene growth-faulted basin, Eugene Island 330, offshore Louisiana. *Basin Research*, *10*, 177–196. https://doi.org/10.1046/j.1365-2117.1998.00052.x

Graham, J., Crooks, J. H. A., & Bell, A. L. (1983). Time effects on the stress-strain behaviour of natural soft clays. *Geotechnique*, *33*(3), 327–340. https://doi.org/10.1680/geot.1983.33.3.327

Gratier, J. P., Favreau, P., & Renard, F. (2003). Modeling fluid transfer along California faults when integrating pressure solution crack sealing and compaction processes. *Journal of Geophysical Research*, *108*, 2104. https://doi.org/10.1029/2001jb000380

Grozic, J. L. H. (2005). Reply to the discussion by Clementino on "An oedometer test study on the preconsolidation stress of glaciomarine clays". *Canadian Geotechnical Journal*, *42*, 975–976. https://doi.org/10.1139/t05-011

Gu, J. C., Rice, J. R., Ruina, A. L., & Simon, T. T. (1984). Slip motion and stability of a single degree of freedom elastic system with rate and state dependent friction. *Journal of the Mechanics and Physics of Solids*, *32*(3), 167–196. https://doi.org/10.1016/0022-5096(84)90007-3

Gulick, S. P. S., Austin, J. A., McNeill, L. C., Bangs, N. L. B., Martin, K. M., Henstock, T. J., et al. (2011). Updip rupture of the 2004 Sumatra earthquake extended by thick indurated sediments. *Nature Geoscience*, *4*, 453–456. https://doi.org/10.1038/ngeo1176

Guo, J., Likos, W. J., Underwood, M. B., Skarbek, R. M., Adamson, N., & Saffer, D. M. (2011). Data report: consolidation characteristics of sediments from Sites C0002, C0006, and C0007, IODP Expeditions 315 and 316, NanTroSEIZE Stage 1. In M. Kinoshita, H. Tobin, J. Ashi, G. Kimura, S. Lallemant, E. J. Screaton, et al. (Eds.), *Proceedings of the Integrated Ocean Drilling Program, 314/315/316*. Washington, DC: Integrated Ocean Drilling Program Management International, Inc. https://doi.org/10.2204/iodp.proc.314315316.213.2011

Guo, J., & Underwood, M. B. (2014). Data report: Consolidation and permeability of sediments from Sites C0011, C0012, and C0018, IODP Expeditions 322 and 333, NanTroSEIZE Stage 2. In S. Saito, M. B. Underwood, Y. Kubo, & the Expedition 322 Scientists, (Eds.), *Proceedings of the Integrated Ocean Drilling Program*, *322*. Tokyo: Integrated Ocean Drilling Program Management International, Inc. https://doi.org/10.2204/iodp.proc.322.209.2014

Gutscher, M. A., Klaeschen, D., Flueh, E., & Malavieille, J. (2001). Non-Coulomb wedges, wrong-way thrusting, and natural hazards in Cascadia. *Geology*, *29*(5), 379–382. https://doi.org/10.1130/0091-7613(2001)029<0379:NCWWWT>2.0.CO;2

Hamilton, E. L. (1976). Variations of density and porosity with depth in deep-sea sediments. *Journal of Sedimentary Petrology*, *46*(2), 280–300. https://doi.org/10.1306/212f6f3c-2b24-11d7-8648000102c1865d

Henry, P. (2000). Fluid flow at the toe of the Barbados accretionary wedge constrained by thermal, chemical, and hydrogeologic observations and models. *Journal of Geophysical Research*, *105*(B11), 25855–25872. https://doi.org/10.1029/2000jb900215

Henry, P., Kanamatsu, T., Moe, K., & the Expedition 333 Scientists. (2012a). Site C0011. In P. Henry, T. Kanamatsu, K. Moe, & the Expedition 333 Scientists (Eds.), *Proceedings of the Integrated Ocean Drilling Program, 333*. Tokyo: Integrated Ocean Drilling Program Management International, Inc. https://doi.org/10.2204/iodp.proc.333.104.2012

Henry, P., Kanamatsu, T., Moe, K., & the Expedition 333 Scientists. (2012b). Site C0012. In P. Henry, T. Kanamatsu, K. Moe, & the Expedition 333 Scientists (Eds.), *Proceedings of the Integrated Ocean Drilling Program, 333*. Tokyo: Integrated Ocean Drilling Program Management International, Inc. https://doi.org/10.2204/iodp.proc.333.105.2012

Henstock, T. J., McNeill, L. C., & Tappin, D. R. (2006). Seafloor morphology of the Sumatran subduction zone: Surface rupture during megathrust earthquakes? *Geology*, *34*(6), 485–488. https://doi.org/10.1130/22426.1

Heuer, V. B., Inagaki, F., Morono, Y., Kubo, Y., Maeda, L., Bowden, S., et al. (2017). Site C0023. In V. B. Heuer, F. Inagaki, Y. Morono, Y. Kubo, L. Maeda, & The Expedition 370 Scientists (Eds.), *Proceedings of the International Ocean Discovery Program*, *370*. College Station, TX: International Ocean Discovery Program. https://doi.org/10.14379/iodp.proc.370.103.2017

Hiramatsu, Y., Honma, H., Saiga, A., Furumoto, M., & Ooida, T. (2005). Seismological evidence on characteristic time of crack healing in the shallow crust. *Geophysical Research Letters*, *32*, L09304. https://doi.org/10.1029/2005gl022657

Hirose, H., & Hirahara, K. (2002). A model for complex slip behavior on a large asperity at subduction zones. *Geophysical Research Letters*, *29*(22), 2068. https://doi.org/10.1029/2002GL015825

Hoffman, N. W., & Tobin, H. J. (2004). An empirical relationship between velocity and porosity for underthrust sediments of the Nankai Trough Accretionary Prism. In H. Mikada, G. F. Moore, A. Taira, K. Becker, J. C. Moore, & A. Klaus (Eds.), *Proceedings of the Ocean Drilling Program, Scientific Results, 190/196*. College Station, TX: Ocean Drilling Program. https://doi.org/10.2973/odp.proc.sr.190196.355.2004

Hornbach, M. J., Braudy, N., Briggs, R. W., Cormier, M. H., Davis, M. B., Diebold, J. B., et al. (2010). High tsunami frequency as a result of combined strike-slip faulting and coastal landslides. *Nature Geoscience*, *3*, 783–788. https://doi.org/10.1038/ngeo975

Howald, T., Person, M., Campbell, A., Lueth, V., Hofstra, A., Sweetkind, D., & Karlstrom, K. (2015). Evidence for long timescale (> 103 years) changes in hydrothermal activity induced by seismic events. *Geofluids*, *15*(1–2), 252–268. https://doi.org/10.1111/gfl.12113

Huffman, K. A., & Saffer, D. M. (2016). In situ stress magnitudes at the toe of the Nankai trough accretionary prism, offshore Shikoku Island, Japan. *Journal of Geophysical Research: Solid Earth*, *121*, 1202–1217. https://doi.org/10.1002/2015jb012415

Huyakorn, P. S., & Pinder, G. F. (1978). A pressure-enthalpy finite element model for simulating hydrothermal reservoirs. *Mathematics and Computers in Simulation*, *20*, 167–178. https://doi.org/10.1016/0378-4754(78)90066-6

Hüpers, A., Ikari, M. J., Dugan, B., Underwood, M. B., & Kopf, A. J. (2015). Origin of a zone of anomalously high porosity in the subduction inputs to Nankai Trough. *Marine Geology*, *361*, 147–162. https://doi.org/10.1016/j.margeo.2015.01.004

Hüpers, A., & Kopf, A. J. (2009). The thermal influence on the consolidation state of underthrust sediments from the Nankai margin and its implications for excess pore pressure. *Earth and Planetary Science Letters*, *286*, 324–332. https://doi.org/10.1016/j.epsl.2009.05.047

Hüpers, A., & Kopf, A. J., & The Expedition 322 Scientists (2012). Data report: Consolidation properties of silty claystones and sandstones sampled seaward of the Nankai Trough subduction zone, IODP Sites C0011 and C0012. In S. Saito, M. B. Underwood, & Y. Kubo (Eds.), *Proceedings of the Integrated Ocean Drilling Program*, *322*. Tokyo: Integrated Ocean Drilling Program Management International, Inc. https://doi.org/10.2204/iodp.proc.322.203.2012

Hüpers, A., Torres, M. E., Owari, S., McNeill, L. C., Dugan, B., Henstock, T. J., et al. (2017). Release of mineral-bound water prior to subduction tied to shallow seismogenic slip off Sumatra. *Science*, *356*, 841–844. https://doi.org/10.1126/science.aal3429

Hyndman, R. D., & Wang, K. (1995). The rupture zone of Cascadia great earthquakes from current deformation and the thermal regime. *Journal of Geophysical Research: Solid Earth*, *100*(B11), 22133–22154. https://doi.org/10.1029/95JB01970

Ienaga, M., McNeill, L. C., Mikada, H., Saito, S., Goldberg, D., & Moore, J. C. (2006). Borehole image analysis of the Nankai Accretionary Wedge, ODP Leg 196: Structural and stress studies. *Tectonophysics*, *426*, 207–220. https://doi.org/10.1016/j.tecto.2006.02.018

Ikari, M. J., & Hüpers, A. (2021). Velocity-weakening friction induced by laboratory-controlled lithification. *Earth and Planetary Science Letters*, *554*, 116682. https://doi.org/10.1016/j.epsl.2020.116682

Ikari, M. J., & Kopf, A. J. (2015). The role of cohesion and overconsolidation in submarine slope failure. *Marine Geology*, *369*, 153–161. https://doi.org/10.1016/j.margeo.2015.08.012

Ikari, M. J., & Kopf, A. J. (2017). Seismic potential of weak, near-surface faults revealed at plate tectonic slip rates. *Science Advances*, *3*, e1701269. https://doi.org/10.1126/sciadv.1701269

Ikari, M. J., Marone, C., Saffer, D. M., & Kopf, A. J. (2013). Slip weakening as a mechanism for slow earthquakes. *Nature Geoscience*, *6*(6), 468–472. https://doi.org/10.1038/ngeo1818

Ikari, M. J., & Saffer, D. M. (2012). Permeability contrasts between sheared and normally consolidated sediments in the Nankai accretionary prism. *Marine Geology*, *295*, 1–13. https://doi.org/10.1016/j.margeo.2011.11.006

Ikari, M. J., Saffer, D. M., & Marone, C. (2007). Effect of hydration state on the frictional properties of montmorillonite-based fault gouge. *Journal of Geophysical Research: Solid Earth*, *112*(B6), B06423. https://doi.org/10.1029/2006JB004748

Ikari, M. J., Wallace, L. M., Rabinowitz, H. S., Savage, H. M., Hamling, I. J., & Kopf, A. J. (2020). Observations of laboratory and natural slow slip events: Hikurangi subduction zone, New Zealand. *Geochemistry, Geophysics, Geosystems*, *21*, e2019GC008717. https://doi.org/10.1029/2019GC008717

Im, K., Elsworth, D., Marone, C., & Leeman, J. (2017). The impact of frictional healing on stick-slip recurrence interval and stress drop: Implications for earthquake scaling. *Journal of Geophysical Research: Solid Earth*, *122*, 10,102–10,117. https://doi.org/10.1002/2017JB014476

Im, K., Saffer, D., Marone, C., & Avouac, J. P. (2020). Slip-rate-dependent friction as a universal mechanism for slow slip events. *Nature Geoscience*, *13*(10), 705–710. https://doi.org/10.1038/s41561-020-0627-9

Ito, Y., & Obara, K. (2006). Dynamic deformation of the accretionary prism excites very low frequency earthquakes. *Geophysical Research Letters*, *33*, L02311. https://doi.org/10.1029/2005GL025270

Ito, Y., Tsuji, T., Osada, Y., Kido, M., Inazu, D., Hayashi, Y., Tsushima, H., Hino, R., & Fujimoto, H. (2011). Frontal wedge deformation near the source region of the 2011 Tohoku-Oki earthquake. *Geophysical Research Letters*, *38*, L00G05. https://doi.org/10.1029/2011GL048355

Jacobsen, H. M. (1992). Bestemmelse af forbelastningstryk i laboratoriet. Proceedings of nordiske geotechnikermonde NGM-92, Aalborg, Denmark 2, (pp. 455–460) Danish Geotechnical Society Bulletin No. 9 In Danish.

Kanamori, H. (1986). Rupture process of subduction-zone earthquakes. *Annual Review of Earth and Planetary Sciences*, *14*(1), 293–322. https://doi.org/10.1146/annurev.ea.14.050186.001453

Karig, D. E. (1986). Physical properties and mechanical state of accreted sediments in the Nankai Trough, Southwest Japan arc. *Geological Society of America Memoirs*, *166*, 117–134. https://doi.org/10.1130/MEM166-p117

Karig, D. E. (1990). Experimental and observational constraints on the mechanical behaviour in the toes of accretionary prisms. *Geological Society, London, Special Publications*, *54*, 383–398. https://doi.org/10.1144/GSL.SP.1990.054.01.35

Karig, D. E. (1993). Reconsolidation tests and sonic velocity measurements of clay-rich sediments from the Nankai Trough. In I. A. Hill, A. Taira, & J. V. Firth (Eds.), *Proceedings of the Ocean Drilling Program, Scientific Results, 131*, 247–260. College Station, TX: Ocean Drilling Program. https://doi.org/10.2973/odp.proc.sr.131.127.1993

Karig, D. E., & Ask, M. V. S. (2003). Geological perspectives on consolidation of clay-rich marine sediments. *Journal of Geophysical Research*, *108*(B4), 2197. https://doi.org/10.1029/2001jb000652

Kastner, M., Elderfield, H., & Martin, J. B. (1991). Fluids in convergent margins: What do we know about their composition, origin, role in diagenesis and importance for oceanic chemical fluxes?. *Philosophical Transactions of the Royal Society A: Mathematical, Physical and Engineering Sciences*, *335*, 243–259. https://doi.org/10.1098/rsta.1991.0045

Kinoshita, C., & Saffer, D. M. (2018). In situ permeability and scale dependence of an active accretionary prism determined from cross-borehole experiments. *Geophysical Research Letters*, *45*(14), 6935–6943. https://doi.org/10.1029/2018GL078304

Kitajima, H., Chester, F. M., & Biscontin, G. (2012). Mechanical and hydraulic properties of Nankai accretionary prism sediments: Effect of stress path. *Geochemistry, Geophysics, Geosystems*, *13*(1). https://doi.org/10.1029/2012GC004124

Kitajima, H., & Saffer, D. M. (2012). Elevated pore pressure and anomalously low stress in regions of low frequency earthquakes along the Nankai Trough subduction megathrust. *Geophysical Research Letters*, *39*, L23301. https://doi.org/10.1029/2012GL053793

Kitajima, H., & Saffer, D. M. (2014). Consolidation state of incoming sediments to the Nankai Trough subduction zone: Implications for sediment deformation and properties. *Geochemistry, Geophysics, Geosystems*, *15*, 2821–2839. https://doi.org/doi:10.1002/2014GC005360

Kitajima, H., Saffer, D., Sone, H., Tobin, H., & Hirose, T. (2017). In Situ Stress and Pore Pressure in the Deep Interior of the Nankai Accretionary Prism, Integrated Ocean Drilling Program Site C0002. *Geophysical Research Letters*, *44*, 9644–9652. https://doi.org/10.1002/2017GL075127

Knappett, J., & Craig, R. (2012). *Craig's soil mechanics* (8th edition). Abingdon: Spon Press.

Ko, S. C., Olgaard, D. L., & Wong, T. F. (1997). Generation and maintenance of pore pressure excess in a dehydrating system 1. Experimental and microstructural observations. *Journal of Geophysical Research: Solid Earth*, *102*(B1), 825–839. https://doi.org/10.1029/96JB02485

Kodaira, S., Iidaka, T., Kato, A., Park, J. O., Iwasaki, T., & Kaneda, Y. (2004). High pore fluid pressure may cause silent slip in the Nankai Trough. *Science*, *304*, 1295–1298. https://doi.org/10.1126/science.1096535

Kopf, A. J., & Brown, K. M. (2003). Friction experiments on saturated sediments and their implications for the stress state of the Nankai and Barbados subduction thrusts. *Marine Geology*, *202*, 193–210. https://doi.org/10.1016/S0025-3227(03)00286-X

Kopf, A., Araki, E., Toczko, S., & the Expedition 332 Scientists (2011). The SmartPlug and GeniusPlug: simple retrievable observatory systems for NanTroSEIZE borehole monitoring. In Kopf, A., Araki, E., Toczko, S., and the Expedition 332 Scientists (Eds.), *Proceedings of the Integrated Ocean Drilling Program*, *332*. Tokyo: Integrated Ocean Drilling Program Management International, Inc. https://doi.org/10.2204/iodp.proc.332.105.2011

Kopf, A., Saffer, D., Toczko, S., Araki, E., Carr, S., Kimura, T., et al. (2017). Expedition 365 summary. In Saffer, D., Kopf, A., Toczko, S., and the Expedition 365 Scientists (Eds.), NanTroSEIZE Stage 3: Shallow Megasplay Long-Term Borehole Monitoring System. *Proceedings of the International Ocean Discovery Program*, *365*. College Station, TX: International Ocean Discovery Program. https://doi.org/10.14379/iodp.proc.365.101.2017

Koulali, A., McClusky, S., Wallace, L., Allgeyer, S., Tregoning, P., D'Anastasio, E., & Benavente, R. (2017). Slow slip events and the 2016 TeAraroa *Mw* 7.1 earthquake interaction: Northern Hikurangi subduction, New Zealand. *Geophysical Research Letters*, *44*, 8336–8344. https://doi.org/10.1002/2017GL074776

Lauer, R. M., & Saffer, D. M. (2015). The impact of splay faults on fluid flow, solute transport, and pore pressure distribution in subduction zones: A case study offshore the Nicoya Peninsula, Costa Rica. *Geochemistry, Geophysics, Geosystems*, *16*(4), 1089–1104. https://doi.org/10.1002/2014GC005638

Lauer, R. M., Saffer, D. M., & Harris, R. N. (2017). Links between clay transformation and earthquakes along the Costa Rican subduction margin. *Geophysical Research Letters*, *44*(15), 7725–7732. https://doi.org/10.1002/2017GL073744

Lay, T., Bilek, S., Dixon, T. H., & Moore, J. C. (2007). Anomalous earthquake ruptures at shallow depths on subduction zone megathrusts. In T. H. Dixon, & J. C. Moore (Eds.), *The seismogenic zone of subduction thrust faults* (pp. 476–511). New York, NY: Columbia University Press.

Leonards, G. A., & Ramiah, B. K. (1960). Time Effects in the Consolidation of Clays. In *Papers on Soils 1959 Meetings* (pp. 116–130). West Conshohocken, PA: ASTM International. https://doi.org/10.1520/stp44309s

Lin, W., Byrne, T. B., Kinoshita, M., McNeill, L. C., Chang, C., Lewis, J. C., et al. (2016). Distribution of stress state in the Nankai subduction zone, southwest Japan and a comparison with Japan Trench. *Tectonophysics*, *692*, 120–130. https://doi.org/10.1016/j.tecto.2015.05.008

Liu, Y., & Rice, J. R. (2007). Spontaneous and triggered aseismic deformation transients in a subduction fault model. *Journal of Geophysical Research*, *112*, B09404. https://doi.org/10.1029/2007jb004930

Locat, J., & Lee, H. J. (2002). Submarine landslides: Advances and challenges. *Canadian Geotechnical Journal*, *39*, 193–212. https://doi.org/10.1139/t01-089

Locat, J., & Lefebvre, G. (1986). The origin of structuration of the Grande-Baleine marine sediments, Québec, Canada. *Quarterly Journal of Engineering Geology and Hydrogeology*, *19*(4), 365–374. https://doi.org/10.1144/gsl.qjeg.1986.19.04.0

Long, H., Flemings, P. B., Germaine, J. T., & Saffer, D. M. (2011). Consolidation and overpressure near the seafloor in the Ursa Basin, Deepwater Gulf of Mexico. *Earth and Planetary Science Letters*, *305*(1–2), 11–20. https://doi.org/10.1016/j.epsl.2011.02.007

Maltman, A. J., Byrne, T., Karig, D. E., & Lallemant, S. (1993). Deformation at the toe of an active accretionary prism: Synopsis of results from ODP Leg 131, Nankai, SW Japan. *Journal of Structural Geology*, *15*(8), 949–964. https://doi.org/10.1016/0191-8141(93)90169-b

McAdoo, B. G., Capone, M. K., & Minder, J. (2004). Seafloor geomorphology of convergent margins: Implications for Cascadia seismic hazard. *Tectonics*, *23*(TC6008). https://doi.org/10.1029/2003TC001570

McAdoo, B. G., Pratson, L. F., & Orange, D. L. (2000). Submarine landslide geomorphology, US continental slope. *Marine Geology*, *169*, 103–136. https://doi.org/10.1016/S0025-3227(00)00050-5

McNeill, L. C., Dugan, B., Petronotis, K. E., Backman, J., Bourlange, S., Chemale, F., et al. (2017a). Expedition 362 summary. In L.C. McNeill, B. Dugan, K. E. Petronotis, & the Expedition 362 Scientists (Eds.), *Proceedings of the International Ocean Discovery Program, 362*. College Station, TX: International Ocean Discovery Program. https://doi.org/10.14379/iodp.proc.362.101.2017

McNeill, L. C., Dugan, B., Petronotis, K. E., Backman, J., Bourlange, S., Chemale, F., et al. (2017b). Site U1480. In L.C. McNeill, B. Dugan, K. E. Petronotis, & the Expedition 362 Scientists (Eds.), *Proceedings of the International Ocean Discovery Program, 362*. College Station, TX: International Ocean Discovery Program. https://doi.org/10.14379/iodp.proc.362.103.2017

McNeill, L. C., & Henstock, T. J. (2014). Forearc structure and morphology along the Sumatra-Andaman subduction zone. *Tectonics*, *33*, 112–134. https://doi.org/10.1002/2012TC003264

McNulty, E. G., Gorman, C. T., & Hopkins, T. C. (1978). Analysis of time-dependent consolidation data. *Research Report 488 Department of Transportation, Commonwealth of Kentucky*.

Meltzner, A. J., Sieh, K., Chiang, H. W., Shen, C. C., Suwargadi, B. W., Natawidjaja, D. H., et al. (2012). Persistent termini of 2004- and 2005-like ruptures of the Sunda megathrust. *Journal of Geophysical Research*, *117*, B04405. https://doi.org/10.1029/2011JB008888

Meridth, L. N., Screaton, E. J., Jaeger, J. M., James, S. R., & Villaseñor, T. (2017). The impact of rapid sediment accumulation on pore pressure development and dehydration reactions during shallow subduction in the Gulf of Alaska. *Geochemistry, Geophysics, Geosystems*, *18*(1), 189–203. https://doi.org/10.1002/2016GC006693

Miyazaki, S. I., & Heki, K. (2001). Crustal velocity field of southwest Japan: Subduction and arc-arc collision. *Journal of Geophysical Research: Solid Earth*, *106*(B3), 4305–4326. https://doi.org/10.1029/2000JB900312

Moeremans, R., Singh, S. C., Mukti, M., McArdle, J., & Johansen, K. (2014). Seismic images of structural variations along the deformation front of the Andaman-Sumatra subduction zone: Implications for rupture propagation and tsunamigenesis. *Earth and Planetary Science Letters*, *386*, 75–85. https://doi.org/10.1016/j.epsl.2013.11.003

Moore, G. F., Taira, A., Klaus, A., et al. (2001). *Proceedings of the Ocean Drilling Program, Initial Reports, 190*. College Station, TX: Ocean Drilling Program. https://doi.org/10.2973/odp.proc.ir.190.2001

Moore, G. F., Taira, A., Klaus, A., Becker, L., Boeckel, B., Cragg, B. A., et al. (2001). New insights into deformation and fluid flow processes in the Nankai Trough accretionary prism: Results of Ocean Drilling

Program Leg 190. *Geochemistry, Geophysics, Geosystems*, *2*.GC000166. https://doi.org/10.1029/2001gc000166

Moore, J. C., Klaus, A., Bangs, N. L., Bekins, B., Brückmann, W., Bücker, C. J., et al. (1998). Site 1044. In J. Casey Moore & A. Klaus (Eds.), *Proceedings of the Ocean Drilling Program, Initial Reports, 171A*, 19–37. College Station, TX: Ocean Drilling Program.

Moore, J. C., Moore, G. F., Cochrane, G. R., & Tobin, H. J. (1995). Negative-polarity seismic reflections along faults of the Oregon accretionary prism: Indicators of overpressuring. *Journal of Geophysical Research*, *100*(B7), 12895–12906. https://doi.org/10.1029/94jb02049

Moore, J. C., Rowe, C., and Meneghini, F., (2007). How Accretionary Prisms Elucidate Seismogenesis in Subduction Zones. In T. H. Dixon, & J. C. Moore (Eds.), *The seismogenic zone of subduction thrust faults* (pp. 288–302). New York, NY: Columbia University Press.

Moore, J. C., & Saffer, D. M. (2001). Updip limit of the seismogenic zone beneath the accretionary prism of southwest Japan: An effect of diagenetic to low-grade metamorphic processes and increasing effective stress. *Geology*, *29*(2), 183–186. https://doi.org/10.1130/0091-7613(2001)029<0183:ulotsz>2.0.co;2

Moore, J. C., & Tobin, H. (1997). Estimated fluid pressures of the Barbados accretionary prism and adjacent sediments. In T. H. Shipley, Y. Ogawa, P. Blum, & J. M. Bahr (Eds.), *Proceedings of the Ocean Drilling Program*, *Scientific Results*, *156*, 229–238. College Station, TX: Ocean Drilling Program.

Moore, J. C., & Vrolijk, P. (1992). Fluids in accretionary prisms. *Reviews of Geophysics*, *30*(2), 113–135. https://doi.org/10.1029/92rg00201

Moran, K., Brückmann, W., Feeser, V., & Campanella, R. G. (1993). In situ stress conditions at Nankai Trough, Site 808. In I. A. Hill, et al. (Eds.), *Proceedings of the Ocean Drilling Program*, *Scientific Results*, *131*, 283–291. College Station, TX: Ocean Drilling Program.

Moreno, M., Haberland, C., Oncken, O., Rietbrock, A., Angiboust, S., & Heidbach, O. (2014). Locking of the Chile subduction zone controlled by fluid pressure before the 2010 earthquake. *Nature Geoscience*, *7*(4), 292–296. https://doi.org/10.1038/ngeo2102

Morgan, J. K., & Ask, M. V. S. (2004). Consolidation state and strength of underthrust sediments and evolution of the décollement at the Nankai accretionary margin: Results of uniaxial reconsolidation experiments. *Journal of Geophysical Research*, *109*, B03102. https://doi.org/10.1029/2002jb002335

Nobes, D. C., Mwenifumbo, C. J., Mienert, J., & Blangy, J. P. (1991). The problem of porosity rebound in deep-sea sediment cores: A comparison of laboratory and in situ physical-property measurements, Site 704, Meteor rise. In P. F. Ciesielski, Y. Kristoffersen, et al. (Eds.), *Proceedings of the Ocean Drilling Program*, *Scientific Results*, *114*, 711–716. College Station, TX: Ocean Drilling Program.

Oleskevich, D. A., Hyndman, R. D., & Wang, K. (1999). The updip and downdip limits to great subduction earthquakes: Thermal and structural models of Cascadia, south Alaska, SW Japan, and Chile. *Journal of Geophysical Research: Solid Earth*, *104*(B7), 14965–14991. https://doi.org/10.1029/1999JB900060

Olsen, H. W., Rice, T. L., Mayne, P. W., & Singh, R. D. (1986). Piston core properties and disturbance effects. *Journal of Geotechnical Engineering*, *112*, 608–625. https://doi.org/10.1061/(asce)0733-9410(1986)112:6(608)

Pacheco, J. F., & Sykes, L. R. (1992). Seismic moment catalog of large shallow earthquakes, 1900 to 1989. *Bulletin of the Seismological Society of America*, *82*(3), 1306–1349. https://doi.org/10.1785/BSSA0820031306

Pacheco Silva, F. (1970). A new graphical construction for determination of the pre-consolidation stress of a soil sample. *Proceedings of the 4th Brazilian Conference on Soil Mechanics and Foundation Engineering*, *2*(1), 225–232. Rio de Janeiro, Brazil.

Park, J. O., Naruse, H., & Bangs, N. L. (2014). Along-strike variations in the Nankai shallow décollement properties and their implications for tsunami earthquake generation. *Geophysical Research Letters*, *41*, 7057–7064. https://doi.org/10.1002/2014gl061096

Peltonen, C., Marcussen, Ø., Bjørlykke, K., & Jahren, J. (2009). Clay mineral diagenesis and quartz cementation in mudstones: The effects of smectite to illite reaction on rock properties. *Marine and Petroleum Geology*, *26*(6), 887–898. https://doi.org/10.1016/j.marpetgeo.2008.01.021

Perret, D., Locat, J., & Leroueil, S. (1995). Strength development with burial in fine-grained sediments from the Saguenay Fjord, Quebec. *Canadian Geotechnical Journal*, *32*(2), 247–262. https://doi.org/10.1139/t95-027

Persson, B.N. (2000). *Sliding Friction: Physical Principles and Applications*. Berlin: Springer Science & Business Media.

Qin, Y., & Singh, S. C. (2017). Detailed seismic velocity of the incoming subducting sediments in the 2004 great Sumatra earthquake rupture zone from full waveform inversion of long offset seismic data. *Geophysical Research Letters*, *44*, 3090–3099. https://doi.org/10.1002/2016GL072175

Rabinowitz, H. S., Savage, H. M., Polissar, P. J., Rowe, C. D., & Kirkpatrick, J. D. (2020). Earthquake slip surfaces identified by biomarker thermal maturity within the 2011 Tohoku-Oki earthquake fault zone. *Nature Communications*, *11*(1), 1–9. https://doi.org/10.1038/s41467-020-14447-1

Rabinowitz, H. S., Savage, H. M., Skarbek, R. M., Ikari, M. J., Carpenter, B. M., & Collettini, C. (2018). Frictional behavior of input sediments to the Hikurangi Trench, New Zealand. *Geochemistry, Geophysics, Geosystems*, 19, 2973–2990. https://doi.org/10.1029/2018GC007633

Ranjith, K., & Rice, J. R. (1999). Stability of quasi-static slip in a single degree of freedom elastic system with rate and state dependent friction. *Journal of the Mechanics and Physics of Solids*, *47*(6), 1207-1218. https://doi.org/10.1016/S0022-5096(98)00113-6

Raymer, L. L., Hunt, E. R., & Gardner, J. S. (1980). An improved sonic transit time-to-porosity transform. In *21st Annual Logging Symposium*. Lafayette, LA: Society of Professional Well Log Analysts.

Rea, B. R., & Gaillot, P. (2004). Data report: Correction of core physical properties and composite depths for sites 1215-1222 using core-log correlation-derived rebound coefficients. In P. A. Wilson, M. Lyle, T. R. Janecek, & J. v. Firth (Eds.), *Proceedings of the Ocean Drilling Program, Scientific Results, 199*. College Station, TX: Ocean Drilling Program. https://doi.org/10.2973/odp.proc.sr.199.208.2004

Rhie, J., Dreger, D., Bürgmann, R., & Romanowicz, B. (2007). Slip of the 2004 Sumatra-Andaman earthquake from joint inversion of long-period global seismic waveforms and GPS static offsets. *Bulletin of the Seismological Society of America*, *97*(1A), S115–S127. https://doi.org/10.1785/0120050620

Rice, J. R. & Ruina, A. L. (1983). Stability of steady frictional slipping. *Journal of Applied Mechanics*, *50*, 343–349. https://doi.org/10.1115/1.3167042

Roscoe, K. H., & Burland, J. B. (1968). On the generalized stress-strain behaviour of "wet" clay. In J. Heyman (Eds.), *Engineering plasticity* (pp. 535–609). Cambridge: Cambridge University Press.

Rubey, W. W., & Hubbert, M. K. (1959). Role of fluid pressure in mechanics of overthrust faulting: II. Overthrust belt in geosynclinal area of western Wyoming in light of fluid-pressure hypothesis. *Bulletin of the Geological Society of America*, *70*, 167–206. https://doi.org/10.1130/0016-7606(1959)70[167:ROFPIM]2.0.CO;2

Rubin, A. M. (2008). Episodic slow slip events and rate-and-state friction. *Journal of Geophysical Research*, *113*, B11414. https://doi.org/10.1029/2008JB005642

Ruff, L. J., & Tichelaar, B. W. (1996). What controls the seismogenic plate interface in subduction zones? In G. E. Bebout, et al. (Eds.), *Subduction: Top to bottom*, *Geophysical Monograph Series* (Vol. 96, pp. 105–111). Washington, DC: AGU. https://doi.org/10.1029/GM096p0105

Ruina, A. L. (1983). Slip instability and state variable friction laws. *Journal of Geophysical Research*, *88*, 10,359–10,370. https://doi.org/10.1029/JB088iB12p10359

Ryan, W. B. F., Carbotte, S. M., Coplan, J. O., O'Hara, S., Melkonian, A., Arko, R., et al. (2009). Global multi-resolution topography synthesis. *Geochemistry, Geophysics, Geosystems*, *10*(3). https://doi.org/10.1029/2008GC002332

Saffer, D. M. (2003). Pore pressure development and progressive dewatering in underthrust sediments at the Costa Rican subduction margin: Comparison with northern Barbados and Nankai. *Journal of Geophysical Research*, *108*(B5), 2261. https://doi.org/10.1029/2002jb001787

Saffer, D. M. (2007). Pore pressure within underthrust sediment in subduction zones. In T. H. Dixon, & J. C. Moore (Eds.), *The seismogenic zone of subduction thrust faults* (pp. 171–209). New York, NY: Columbia University Press.

Saffer, D. M. (2015). The permeability of active subduction plate boundary faults. *Geofluids*, *15*, 193–215. https://doi.org/10.1111/gfl.12103

Saffer, D. M. (2017). Mapping fluids to subduction megathrust locking and slip behavior. *Geophysical Research Letters*, *44*(18), 9337–9340. https://doi.org/10.1002/2017GL075381

Saffer, D. M., & Bekins, B. A. (1998). Episodic fluid flow in the Nankai accretionary complex: Timescale, geochemistry, flow rates, and fluid budget. *Journal of Geophysical Research*, *103*, 30351–30370. https://doi.org/10.1029/98jb01983

Saffer, D. M., & Bekins, B. A. (1999). Fluid budgets at convergent plate margins: Implications for the extent and duration of fault-zone dilation. *Geology*, *27*, 1095–1098. https://doi.org/10.1130/0091-7613(1999)027<1095:fbacpm>2.3.co;2

Saffer, D. M., Guo, J., Underwood, M. B., Likos, W., Skarbek, R. M., Song, I., & Gildow, M. (2011). Data report: consolidation, permeability, and fabric of sediments from the Nankai continental slope, IODP Sites C0001, C0008, and C0004. In M. Kinoshita, H. Tobin, J. Ashi, G. Kimura, S. Lallemant, E. J. Screaton, et al. (Eds.), *Proceedings of the Integrated Ocean Drilling Program, 314/315/316*. Washington, DC: Integrated Ocean Drilling Program Management International, Inc. https://doi.org/10.2204/iodp.proc.314315316.218.2011

Saffer, D. M., & Kopf, A. J. (2016). Boron desorption and fractionation in subduction zone fore arcs: Implications for the sources and transport of deep fluids. *Geochemistry, Geophysics, Geosystems*, *17*(12), 4992–5008. https://doi.org/10.1002/2016GC006635

Saffer, D. M., Lockner, D. A., & McKiernan, A. (2012). Effects of smectite to illite transformation on the frictional strength and sliding stability of intact marine mudstones. *Geophysical Research Letters*, *39*, L11304. https://doi.org/10.1029/2012GL051761

Saffer, D. M., & Marone, C. (2003). Comparison of smectite- and illite-rich gouge frictional properties: Application to the updip limit of the seismogenic zone along subduction megathrusts. *Earth and Planetary Science Letters*, *215*, 219–235. https://doi.org/10.1016/s0012-821x(03)00424-2

Saffer, D. M., & McKiernan, A. W. (2009). Evaluation of in situ smectite dehydration as a pore water freshening mechanism in the Nankai Trough, offshore southwest Japan. *Geochemistry, Geophysics, Geosystems*, *10*, Q02010. https://doi.org/10.1029/2008gc002226

Saffer, D. M., Silver, E. A., Fisher, A. T., Tobin, H., & Moran, K. (2000). Inferred pore pressures at the Costa Rica subduction zone: Implications for dewatering processes. *Earth and Planetary Science Letters*, *177*, 193–207. https://doi.org/10.1016/S0012-821X(00)00048-0

Saffer, D. M., & Tobin, H. J. (2011). Hydrogeology and mechanics of subduction zone forearcs: Fluid flow and pore pressure. *Annual Review of Earth and Planetary Sciences*, *39*, 157–186. https://doi.org/10.1146/annurev-earth-040610-133408

Saffer, D. M., & Wallace, L. M. (2015). The frictional, hydrologic, metamorphic and thermal habitat of shallow slow earthquakes. *Nature Geoscience*, *8*, 594–600. https://doi.org/10.1038/NGEO2490

Saffer, D. M., Wallace, L. M., Barnes, P. M., Pecher, I. A., Petronotis, K. E., LeVay, L. J., et al. (2019a). Expedition 372B/375 summary. In L. M., Wallace, D. M., Saffer, P. M., Barnes, I. A., Pecher, K. E., Petronotis, L. J., LeVay, & the Expedition 372/375 Scientists, Hikurangi Subduction Margin Coring, Logging, and Observatories. *Proceedings of the International Ocean Discovery Program*, 372B/375. College Station, TX: International Ocean Discovery Program. https://doi.org/10.14379/iodp.proc.372B375.101.2019

Saffer, D.M., Wallace, L.M., Barnes, P.M., et al. (2019b). Site U1518. In L. M., Wallace, D. M., Saffer, P. M., Barnes, I. A., Pecher, K. E., Petronotis, L. J., LeVay, & the Expedition 372/375 Scientists, Hikurangi Subduction Margin Coring, Logging, and Observatories. *Proceedings of the International Ocean Discovery Program, 372B/375*. College Station, TX: International Ocean Discovery Program. https://doi.org/10.14379/iodp.proc.372B375.103.2019

Saffer, D.M., Wallace, L.M., & Petronotis, K., 2017. *Expedition 375 Scientific Prospectus: Hikurangi Subduction Margin Coring and Observatories.* International Ocean Discovery Program. http://dx.doi.org/10.14379/iodp.sp.375.2017

Saito, T., Ujiie, K., Tsutsumi, A., Kameda, J., & Shibazaki, B. (2013). Geological and frictional aspects of very-low-frequency earthquakes in an accretionary prism. *Geophysical research letters*, *40*(4), 703–708. https://doi.org/10.1002/grl.50175

Saito, S., Underwood, M. B., Kubo, Y., & the Expedition 322 Scientists. (2010a). Site C0011. In S. Saito, M. B. Underwood, Y. Kubo, & the Expedition 322 Scientists (Eds.), *Proceedings of the Integrated Ocean Drilling Program, 322*. Tokyo: Integrated Ocean Drilling Program Management International, Inc. https://doi.org/10.2204/iodp.proc.322.103.2010

Saito, S., Underwood, M. B., Kubo, Y., & the Expedition 322 Scientists. (2010b). Site C0012. In S. Saito, M. B. Underwood, Y. Kubo, & the Expedition 322 Scientists (Eds.), *Proceedings of the Integrated Ocean Drilling Program, 322*. Tokyo: Integrated Ocean Drilling Program Management International, Inc. https://doi.org/10.2204/iodp.proc.322.104.2010

Sample, J. C., Torres, M. E., Fisher, A., Hong, W. L., Destrigneville, C., Defliese, W. F., & Tripati, A. E. (2017). Geochemical constraints on the temperature and timing of carbonate formation and lithification in the Nankai Trough, NanTroSEIZE transect. *Geochimica et Cosmochimica Acta*, *198*, 92–114. https://doi.org/10.1016/j.gca.2016.10.013

Santagata, M. C., & Germaine, J. T. (2002). Sampling disturbance effects in normally consolidated clays. *Journal of Geotechnical and Geoenvironmental Engineering*, *128*, 997–1006. https://doi.org/10.1061/(asce)1090-0241(2002)128:12(997)

Sawyer, A. H., Flemings, P. B., Elsworth, D., & Kinoshita, M. (2008). Response of submarine hydrologic monitoring instruments to formation pressure changes: Theory and application to Nankai advanced CORKs. *Journal of Geophysical Research*, *113*, B01102. https://doi.org/10.1029/2007jb005132

Scholz, C. H. (1998). Earthquakes and friction laws. *Nature*, *391*, 37–42. https://doi.org/10.1038/34097

Scholz, C. H. (2019). *The mechanics of earthquakes and faulting*. Cambridge University Press.

Schwartz, S. Y., & Rokosky, J. M. (2007). Slow slip events and seismic tremor at circum-Pacific subduction zones. *Reviews of Geophysics*, *45*, RG3004. https://doi.org/10.1029/2006RG000208

Screaton, E., Saffer, D., Henry, P., Hunze, S., & Leg 190 Shipboard Scientific Party (2002). Porosity loss within the underthrust sediments of the Nankai accretionary complex: Implications for overpressures. *Geology*, *30*(1), 19–22. https://doi.org/10.1130/0091-7613(2002)030<0019:plwtus>2.0.co;2

Screaton, E. J., Wuthrich, D. R., & Dreiss, S. J. (1990). Permeabilities, fluid pressures, and flow rates in the Barbados Ridge Complex. *Journal of Geophysical Research*, *95*(B6), 8997–9007. https://doi.org/10.1029/jb095ib06p08997

Seely, D. R. (1977). The Significance of Landward Vergence and Oblique Structural Trends on Trench Inner Slopes. In M. Talwani & W. C. Pitman III (Eds.), *Island Arcs, Deep Sea Trenches and Back-Arc Basins* (pp. 187–198). Washington, D.C.: American Geophysical Union. https://doi.org/10.1029/ME001p0187

Seno, T., Stein, S., & Gripp, A. E. (1993). A model for the motion of the Philippine Sea Plate consistent with NUVEL-1 and geological data. *Journal of Geophysical Research*, *98*(B10), 17941–17948. https://doi.org/10.1029/93jb00782

Seno, Tetsuzo. (2002). Tsunami earthquakes as transient phenomena. *Geophysical Research Letters*, *29*(10), 1419. https://doi.org/10.1029/2002gl014868

Shi, W., Wang, J., Guo, L., Hu, X., Fu, H., Jin, J., & Jin, F. (2018). Undrained cyclic behavior of overconsolidated marine soft clay under a traffic-load-induced stress path. *Marine Georesources and Geotechnology*, *36*(1), 163–172. https://doi.org/10.1080/1064119X.2017.1355343

Shibazaki, B., & Iio, Y. (2003). On the physical mechanism of silent slip events along the deeper part of the seismogenic zone. *Geophysical Research Letters*, *30*(9), 1489. https://doi.org/10.1029/2003GL017047

Sibson, R. H. (1990). Conditions for fault-valve behaviour. In R. J. Knipe, & E. H. Rutter (Eds.), Deformation mechanisms, rheology and tectonics. *Geological Society*, *London*, *Special Publications*, *54*, 15–28. https://doi.org/10.1144/GSL.SP.1990.054.01.02

Sibson, R. H., Robert, F., & Poulsen, K. H. (1988). High-angle reverse faults, fluid-pressure cycling, and mesothermal gold-quartz deposits. *Geology*, *16*(6), 551–555. https://doi.org/10.1130/0091-7613(1988)016<0551:harffp>2.3.co;2

Skarbek, R. M., & Saffer, D. M. (2009). Pore pressure development beneath the décollement at the Nankai subduction zone: Implications for plate boundary fault strength and sediment dewatering. *Journal of Geophysical Research*, *114*, B07401. https://doi.org/10.1029/2008jb006205

Skempton, A. W. (1954). The pore-pressure coefficients A and B. *Geotechnique*, *4*, 143–147. https://doi.org/10.1680/geot.1954.4.4.143

Song, T.-R. A., Helmberger, D. v, Brudzinski, M. R., Clayton, R. W., Davis, P., Pérez-campos, X., & Singh, S. K. (2009). Subducting slab ultra-slow velocity layer coincident with silent earthquakes in southern Mexico. *Science*, *324*, 502–507. https://doi.org/10.1126/science.1167595

Stern, R. J. (2002). Subduction zones. *Reviews of Geophysics*. *40*(4), 1012. https://doi.org/10.1029/2001RG000108

Steurer, J. F., & Underwood, M. B. (2003). Clay mineralogy of mudstones from the Nankai Trough reference Sites 1173 and 1177 and frontal accretionary prism Site 1174. In H. Mikada, G. F. Moore, A. Taira, K. Becker, J. C. Moore, & A. Klaus (Eds.), *Proceedings of the Ocean Drilling Program, Scientific Results*, *190/196*. College Station, TX: Ocean Drilling Program.

Stigall, J., & Dugan, B. (2010). Overpressure and earthquake initiated slope failure in the Ursa region, northern Gulf of Mexico. *Journal of Geophysical Research*, *115*(B04101). https://doi.org/10.1029/2009jb006848

Strozyk, F., Strasser, M., Frster, A., Kopf, A., & Huhn, K. (2010). Slope failure repetition in active margin environments: Constraints from submarine landslides in the Hellenic fore arc, eastern Mediterranean. *Journal of Geophysical Research*, *115*(B08103). https://doi.org/10.1029/2009JB006841

Swarbrick, R. E. (2001). Challenges of porosity based pore pressure prediction. In *63rd EAGE Conference & Exhibition*. Amsterdam: European Association of Geoscientists & Engineers. https://doi.org/10.3997/2214-4609-pdb.15.O-25

Taira, A., Hill, I., Firth, J. V., & et al. (1991). *Proceedings of the Ocean Drilling Program, Initial Reports, 131*. College Station, TX: Ocean Drilling Program. https://doi.org/10.2973/odp.proc.ir.131.1991

Taylor, D. W. (1948). *Fundamentals of soil mechanics*. New York: Wiley.

Terzaghi, K. (1943). *Theoretical soil mechanics*. New York: John Wiley and Sons.

Thyberg, B., & Jahren, J. (2011). Quartz cementation in mudstones: Sheet-like quartz cement from clay mineral reactions during burial. *Petroleum Geoscience*, *17*(1), 53–63. https://doi.org/10.1144/1354-079310-028

Tobin, H., Hirose, T., Ikari, M., Kanagawa, K., Kimura, G., Kinoshita, M., et al., & the Expedition 358 Scientists (2020). Expedition 358 summary. In Tobin, H., Hirose, T., Ikari, M., Kanagawa, K., Kimura, G., Kinoshita, M., et al., & the Expedition 358 Scientists (Eds.), *Proceedings of the International Ocean Discovery Program, 358*. College Station, TX: International Ocean Discovery Program. https://doi.org/10.14379/iodp.proc.358.101.2020

Tobin, H. J., Moore, J. C., & Moore, G. F. (1994). Fluid pressure in the frontal thrust of the Oregon accretionary prism: Experimental constraints. *Geology*, *22*(11), 979–982. https://doi.org/10.1130/0091-7613(1994)022<0979:fpitft>2.3.co;2

Tobin, H. J., & Saffer, D. M. (2009). Elevated fluid pressure and extreme mechanical weakness of a plate boundary thrust, Nankai Trough subduction zone. *Geology*, *37*(8), 679–682. https://doi.org/10.1130/g25752a.1

Tobin, H. J., Vannucchi, P., & Meschede, M. (2001). Structure, inferred mechanical properties, and implications for fluid transport in the décollement zone, Costa Rica convergent margin. *Geology*, *29*, 907–910. https://doi.org/10.1130/0091-7613(2001)029<0907:simpai>2.0.co;2

Torres M., Milliken K., Hüpers A., Kim J., Lee S., and Zhang J., Authigenic clay versus carbonate as products of marine silicate weathering (MSiW) in the input sequence to the Sumatra subduction zone. GSA 2020 Connects Online, 26-30 October 2020. https://doi.org/10.1130/abs/2020AM-349206

Townend, J., & Zoback, M. D. (2001). Implications of earthquake focal mechanisms for the frictional strength of the San Andreas fault system. *Geological Society, London, Special Publications*, *186*(1), 13–21. https://doi.org/10.1144/GSL.SP.2001.186.01.02

Trütner, S., Hüpers, A., Ikari, M. J., Yamaguchi, A., & Kopf, A. J. (2015). Lithification facilitates frictional instability in argillaceous subduction zone sediments. *Tectonophysics*, *665*, 177–185. https://doi.org/10.1016/j.tecto.2015.10.004

Tsuji, T., Kamei, R., & Pratt, R. G. (2014). Pore pressure distribution of a mega-splay fault system in the Nankai Trough subduction zone: Insight into up-dip extent of the seismogenic zone. *Earth and Planetary Science Letters*, *396*, 165–178. https://doi.org/10.1016/j.epsl.2014.04.011

Tsuji, T., Tokuyama, H., Costa Pisani, P., & Moore, G. (2008). Effective stress and pore pressure in the Nankai accretionary prism off the Muroto Peninsula, southwestern Japan. *Journal of Geophysical Research*, *113*, B11401. https://doi.org/10.1029/2007jb005002

Ujiie, K., Tanaka, H., Saito, T., Tsutsumi, A., Mori, J. J., Kameda, J., et al. (2013). & the Expedition 343 and 343T Scientists low coseismic shear stress on the Tohoku-Oki megathrust determined from laboratory experiments. *Science*, *342*, 1211–1214. https://doi.org/10.1126/science.1243485

Von Huene, R., & Scholl, D. W. (1991). Observations at convergent margins concerning sediment subduction, subduction erosion, and the growth of continental crust. *Reviews of Geophysics*, *29*(3), 279–316. https://doi.org/10.1029/91RG00969

Walker, K. T., Ishii, M., & Shearer, P. M. (2005). Rupture details of the 28 March 2005 Sumatra Mw 8.6 earthquake imaged with teleseismic P waves. *Geophysical Research Letters*, *32*, L24303. https://doi.org/10.1029/2005GL024395

Wallace, L. M. (2020). Slow slip events in New Zealand. *Annual Review of Earth and Planetary Sciences*, *48*, 175–203. https://doi.org/10.1146/annurev-earth-071719-055104

Wallace, L. M., & Beavan, J. (2010). Diverse slow slip behavior at the Hikurangi subduction margin, New Zealand. *Journal of Geophysical Research*, *115*, B12402. https://doi.org/10.1029/2010JB007717

Wallace, L. M., Beavan, J., McCaffrey, R., & Darby, D. (2004). Subduction zone coupling and tectonic block rotations in the North Island, New Zealand. *Journal of Geophysical Research*, *109*, B12406. https://doi.org/10.1029/2004JB003241

Wallace, L. M., Hreinsdóttir, S., Ellis, S., Hamling, I., D'Anastasio, E., & Denys, P. (2018). Triggered slow slip and afterslip on the southern Hikurangi subduction zone following the Kaikoura earthquake. *Geophysical Research Letters*, *45*, 4710–4718. https://doi.org/10.1002/2018GL077385

Wallace, L. M., Kaneko, Y., Hreinsdóttir, S., Hamling, I., Peng, Z., Bartlow, N., et al. (2017). Large-scale dynamic triggering of shallow slow slip enhanced by overlying sedimentary wedge. *Nature Geoscience*, *10*, 765–770. https://doi.org/10.1038/NGEO3021

Wallace, L. M., Webb, S. C., Ito, Y., Mochizuki, K., Hino, R., Henrys, S., et al. (2016). Slow slip near the trench at the Hikurangi subduction zone, New Zealand. *Science*, *352*, 701–704. https://doi.org/10.1126/science.aaf2349

Wang, K., & He, J. (2008). Effects of frictional behavior and geometry of subduction fault on coseismic seafloor deformation. *Bulletin of the Seismological Society of America*, *98*, 571–579. https://doi.org/10.1785/0120070097

Wang, K., & Hu, Y. (2006). Accretionary prisms in subduction earthquake cycles: The theory of dynamic Coulomb wedge. *Journal of Geophysical Research*, *111*, B06410. https://doi.org/10.1029/2005jb004094

Wood, D. M. (1990). *Soil behaviour and critical state soil mechanics*. Cambridge: Cambridge University Press.

Wyllie, M. R. J., Gregory, A. R., & Gardner, L. W. (1956). Elastic wave velocities in heterogeneous and porous media. *Geophysics*, *21*(1), 41–70. https://doi.org/10.1190/1.1438217

Yamamoto, Y., Lin, W., Oda, H., Byrne, T., & Yamamoto, Y. (2013). Stress states at the subduction input site, Nankai Subduction Zone, using anelastic strain recovery (ASR) data in the basement basalt and overlying sediments. *Tectonophysics*, *600*, 91–98. https://doi.org/10.1016/j.tecto.2013.01.028

You, C. F., Spivack, A. J., Gieskes, J. M., Martin, J. B., & Davisson, M. L. (1996). Boron contents and isotopic compositions in pore waters: a new approach to determine temperature induced artifacts—geochemical implications. *Marine Geology*, *129*(3-4), 351-361. https://doi.org/10.1016/0025-3227(96)83353-6

Zhang, J. (2020). *Moisture, density, and consolidation properties of IODP site C0023 from the shallow Nankai Trough subduction zone*, SW Japan: PANGAEA https://doi.pangaea.de/10.1594/PANGAEA.918818

Zhang, J., He, S., Wang, Y., Wang, Y., Hao, X., Luo, S., et al. (2019). Main Mechanism for Generating Overpressure in the Paleogene Source Rock Series of the Chezhen Depression, Bohai Bay Basin, China. *Journal of Earth Science*, *30*(4), 775–787. https://doi.org/10.1007/s12583-017-0959-6

Zhang, J., Hüpers, A., Kreiter, S., & Kopf, A. J. (2021). Pore Pressure Regime and Fluid Flow Processes in the Shallow Nankai Trough Subduction Zone Based on Experimental and Modeling Results from IODP Site C0023. *Journal of Geophysical Research: Solid Earth*, *126*, e2020JB020248. https://doi.org/10.1029/2020jb020248

Zhou, J., Zhang, B., & Xu, Q. (2016). Effects of lateral friction on the structural evolution of fold-and thrust belts: Insights from sandbox experiments with implications for the origin of landward-vergent thrust wedges in Cascadia. *Geological Society of America Bulletin*, *128*(3–4), 669–683. https://doi.org/10.1130/B31320.1